INVESTIGATION OF RANGE MIGRATION COMPENSATION IN RADAR DETECTION

A THESIS SUBMITTED TO
THE GRADUATE SCHOOL OF NATURAL AND APPLIED SCIENCES
OF
MIDDLE EAST TECHNICAL UNIVERSITY

BY

ONUR ÇULHA

IN PARTIAL FULFILLMENT OF THE REQUIREMENTS
FOR
THE DEGREE OF DOCTOR OF PHILOSOPHY
IN
ELECTRICAL AND ELECTRONIC ENGINEERING

SEPTEMBER 2022

Approval of the thesis:

INVESTIGATION OF RANGE MIGRATION COMPENSATION IN RADAR DETECTION

submitted by **ONUR ÇULHA** in partial fulfillment of the requirements for the degree of **Doctor of Philosophy** i**n Electrical and Electronic Engineering, Middle East Technical University** by,

Prof. Dr. Halil Kalıpçılar
Dean, Graduate School of **Natural and Applied Sciences** _____

Prof. Dr. İlkay Ulusoy
Head of the Department, **Electrical and Electronic Engineering, Middle East Technical University** _____

Prof. Dr. Yalçın Tanık
Supervisor, **Electrical and Electronic Engineering, METU**

Examining Committee Members:

Prof. Dr. Orhan Arıkan
Electrical and Electronic Engineering, Bilkent University _____

Prof. Dr. Yalçın Tanık
Electrical and Electronic Engineering, METU _____

Prof. Dr. Çağatay Candan
Electrical and Electronic Engineering, METU _____

Prof. Dr. Cenk Toker
Electrical and Electronic Engineering, Hacettepe University _____

Assist. Prof. Dr. Gökhan M. Güvensen
Electrical and Electronic Engineering, METU _____

Date: 01.09.2022

I hereby declare that all information in this document has been obtained and presented in accordance with academic rules and ethical conduct. I also declare that, as required by these rules and conduct, I have fully cited and referenced all material and results that are not original to this work.

Name Last name : Onur Çulha

Signature :

ABSTRACT

INVESTIGATION OF RANGE MIGRATION COMPENSATION IN RADAR DETECTION

Çulha, Onur
Doctor of Philosophy, Electrical and Electronic Engineering
Supervisor : Prof. Dr. Yalçın Tanık

September 2022, 155 pages

In this study, range migration compensation methods in radar detection are examined from two different aspects: proposing novel methods to compromise between computational complexity and detection performance, and investigating range migration compensation under clutter and target fluctuation. We proposed a low complexity implementation of repetitive chirp-z transform (CZT) in order to be employed in Keystone transform and Radon Fourier transform with no loss in performance. Another efficient method has been proposed to compensate range migration without repeating CZT. The computer simulations show that the proposed method can achieve almost the same detection performance with significantly lower computational complexity compared to the classical ones. In addition, we investigate performance of range migration compensation methods under clutter and target fluctuation, and propose new methods to compensate range migration in these environments.

Keywords: Radar Detection, Range Migration, Clutter, Target Fluctuation

ÖZ

RADAR TESPİTİNDE MENZİL KAYMASI TELAFİSİNİN İNCELENMESİ

Çulha, Onur
Doktora, Elektrik ve Elektronik Mühendisliği
Tez Yöneticisi: Prof. Dr. Yalçın Tanık

Eylül 2022, 155 sayfa

Bu çalışmada, radar tespitinde menzil kayması telafi yöntemleri iki farklı açıdan incelenmiştir: hesaplama karmaşıklığı ve tespit performansı arasında denge sağlamak için yeni yöntemler önermek ve kargaşa ve hedef dalgalanması altında menzil kayması telafisini araştırmak. Keystone dönüşümünde ve Radon Fourier dönüşümünde performans kaybı olmadan kullanılmak üzere tekrarlayan chirp-z dönüşümünün (CZT) düşük karmaşıklıkta bir uygulamasını öngördük. Ayrıca, CZT'yi tekrarlamadan menzil kaymasını telafi etmek için bir başka verimli yöntem önerilmiştir. Yaptığımız bilgisayar benzetimleri, önerilen yöntemin klasik yöntemlere kıyasla önemli ölçüde daha düşük hesaplama karmaşıklığı ile hemen hemen aynı tespit performansını elde edebileceğini göstermektedir. Son olarak, kargaşa ve hedef dalgalanması altında menzil kayması telafi yöntemlerinin performansı araştırılmış ve bu ortamlarda menzil kaymasını telafi etmek için yeni yöntemler önerilmiştir.

Anahtar Kelimeler: Radar Tespiti, Menzil Kayması, Kargaşa, Hedef Dalgalanması

To my lovely wife and my dear daughter,

ACKNOWLEDGMENTS

I wish to express my deepest gratitude to my supervisor Prof. Dr. Yalçın Tanık for his guidance, advice, criticism, encouragements and insight throughout the research.

I would like to thank my thesis monitoring and examining committee members, Prof. Dr. Orhan Arıkan and Prof. Dr. Çağatay Candan for their suggestions, support, and encouragement.

I would like to forward my appreciation to my friends and colleagues especially, Hüseyin Caner Becer, Ahmet Çakır, and Ali Can Arık who contributed to my thesis with their continuous encouragement.

Special thanks to my dear wife Fulden, who always supported me, never lost her trust in me and always motivated and supported me. In addition, I am very grateful to my sweet daughter Fulya who joined our family and grew up throughout my thesis work. She has always made me happy, energized me and made me even stronger.

TABLE OF CONTENTS

LIST OF TABLES

TABLES

LIST OF FIGURES

FIGURES

LIST OF ABBREVIATIONS

ABBREVIATIONS

CA : Clutter attenutaion

CPI : Coherent processing interval

CTFT : Continuous time Fourier transform

CZT : Chirp z transform

DAST : Doppler ambiguity shift transform

DFT : Discrete Fourier transform

DTFT : Discrete time Fourier transform

FDF : Fractional frequency delay

FFT : Fast Fourier transform

FT : Fourier transform

HT : Hough transform

IDFT : Inverse discrete Fourier transform

IF : Improvement factor

IFFT : Inverse fast Fourier transform

IFT : Inverse Fourier transform

KT : Keystone transform

LFM : Linear frequency modulation

MDD : Minimum detectable Doppler

MDV : Minimum detectable velocity

MF : Matched filter

MTI : Moving target indicator

PD : Pulse Doppler

PRF : Pulse repetition frequency

PRI : Pulse repetition interval

RCS : Radar cross section

RFT : Radon Fourier transform

RMC : Range migration compensation

RT : Radon transform

SCR : Signal to clutter ratio

SIRP : Spherically invariant random process

SNR : Signal to noise ratio

CHAPTER 1

INTRODUCTION

Since its beginning a century ago, the ranging, imaging and positioning of radar targets has been extensively studied, for which numerous applications and variations exist. Although modern radar techniques have undergone rapid development in many fields, there are some serious challenges for effective radar detection. Among them, low SNR high speed targets should be detected effectively with high resolution. Regarding this, it is proposed to increase antenna aperture and transmission power in conventional approach. Nonetheless, this approach may bring about some electronic warfare and radar survivability issues such as cost, vulnerability and probability of intercept. To enhance detection performance while keeping physical radar parameters unchanged is a challenging problem.

Theoretically, it is known that detection performance can be increased via long integration time [1] [2]. However, increasing integration time brings benefit by the price of another limitation: target echoes are required to be confined in a single range resolution cell. Many detection algorithms have been developed in the last decades in order to remove the range walk, which can be divided into two categories: coherent and non-coherent integration. Radon Transform [3] [4] [5], Hough Transform [6] [7] [8] and the track-before-detect technique [9] [10] are classical non-coherent integration techniques. Since the non-coherent integration methods do not consider the phase variation between the pulses, their performance under low signal-to-noise ratio (SNR) environment is insufficient. Regarding the coherent integration techniques, there are mainly two types of methods: parametric and non-parametric search. Sequence reverse transform (SRT) [11], adjacent cross correlation function

(ACCF) [12] and scaled inverse Fourier transform (SCIFT) [13] are typical non-parametric search methods. These non-parametric search methods are computationally more efficient than the parametric search methods; however, they require high SNR input. With regards to the parametric search methods utilizing coherent integration, Keystone Transform (KT) [14] [15] [16] [17] [18] and Radon Fourier Transform (RFT) [19] [20] [21] are well-known algorithms. Although KT can remove range walk by rescaling the slow time axis for each range frequency, it requires interpolation operations and an extensive computational load to search for the Doppler ambiguity factor. A computationally efficient implementation of KT [22] has been proposed by using Chirp-Z transform (CZT). However, this method is still not very efficient because it has to repeat CZT operation for each Doppler ambiguity factor. RFT can compensate range migration by searching through the range and the velocity axes together, but it is computationally expensive because of the 2-dimensional search. Yu et al. [21] proposed to implement RFT by employing CZT to reduce computational load. Even though computational complexity can be lowered by using CZT in KT and RFT, they still need to be improved for real-time operations. Analysis and implementation aspects of KT and RFT are discussed in more detail in Chapter 2.

Most of the studies proposing range migration compensation (RMC) methods in the literature do not take into account the two main issues in real radar detection problem: clutter and target fluctuation. First, unwanted echoes, known as clutter, reflected from land, sea and rain can cause critical performance problems in radar detection. In addition, there may be some cases where both the target and clutter echoes are range migrating. Then, special efforts should be made to mitigate the range migration problem. Secondly, the amplitude of the echo signal from a moving target tends to have some fluctuations, which reduces the probability of detection.

1.1 Objectives

The main objectives pursued in this thesis are related to possible improvements on RMC methods and investigations on application of RMC methods in realistic conditions such as clutter and target fluctuation. The objectives can be detailed as:

- Analyze well-known RMC methods and their implementation aspects
- Propose two new methods: (i) to reduce computational load of existing KT and RFT algorithms without sacrificing the detection performance, and (ii) to achieve almost same detection performance as the RFT with lower computational complexity
- Evaluate the coherent integration performance when KT is applied to detect targets in sea clutter background
- Examine the effect of swapping the orders of clutter suppression and KT in detection of moving targets in rain clutter
- Propose an efficient method to detect targets when both rain clutter and target are range-migrating
- Investigate performance of the KT method for fluctuating targets
- Propose hybrid integration scheme for moderately fluctuating targets in case of range migration

1.2 Outline

We present the problem definition, review well-known RMC methods such as KT and RFT and analyze their implementation aspects in Chapter 2.

In Chapter 3, the KT is evaluated in realistic radar environment such as target fluctuation and clutter. We first introduce target fluctuation and clutter models. Consequently, hybrid integration technique has been analyzed to detect moderately fluctuating targets. Next, we examined the range migration compensation under sea and rain clutter. Finally, we propose a method to remove range migration jointly for both range migrating clutter and target.

Two novel methods are proposed to reduce computational complexity of existing RMC methods in Chapter 4. The first method proposes an efficient implementation of KT and RFT repeating execution of CZT for each Doppler ambiguity factor. The second one is an efficient method to search for the Doppler ambiguity number and residual velocity based on a new technique called Doppler ambiguity shift transform (DAST) developed in this thesis study.

In Chapter 5, this thesis work is summarized and conclusions are drawn.

CHAPTER 2

REVIEW OF COMMON RANGE MIGRATION COMPENSATION METHODS

In this chapter, we will define the range migration problem in radar, review some well-known range compensation methods, and analyze their implementation aspects.

2.1 Problem definition

Pulse integration is an effective way of improving target detection performance in a Pulsed Doppler (PD) radar under a noisy environment. Coherent integration allows obtaining a higher detection signal-to-noise ratio (SNR) than non-coherent integration, thanks to the compensation of phase variations between transmitted pulses.

Besides the improved detection performance, it is possible to obtain lower Doppler frequency and range resolution when transmitting wide-band pulse train in the PD radar. Nevertheless, the combination of the factors such as wide-band pulse, the high target velocity with respect to radar, the long coherent processing interval (CPI) results in considerable range migration. If the target has a high velocity, range between radar and target changes significantly during the long CPI. Wide bandwidth means low range resolution cell. Hence, the high speed target may move more than many range cells for wideband signal and an effective integration among multiple pulses cannot be realized due to the range migration effect. Therefore, how to compensate the envelope migration is the key problem which needs to be solved.

Consider a radar emitting N pulses during the CPI,

$$s_{Tx}(t,n) = p(t - nT_r)exp(j2\pi f_c t) \quad (2.1)$$

where t is time, n is pulse number, T_r is pulse repetition interval (PRI), f_c is the carrier frequency and, *p(t)* is an arbitrary envelope signal. We define

$$Q(f) = P(f)P^*(f) \quad (2.2)$$

where *P(f)* is the FT of *p(t)*, $(.)^*$ denotes complex conjugate, and $q(t)$ and $Q(f)$ are FT pairs:

$$q(t) = p(t) * p^*(-t) \quad (2.3)$$

We assume the pulses are scattered back from a point scatterer and the radial distance between the radar and the target is *R(n)* for the n^{th} pulse. We store the received signals in a 2-dimensional matrix $s_{Rx}(\tilde{t}, n)$ where $\tilde{t} = t - nTr$, is known as the "fast time" and *n* is the pulse count (slow-time index) from 0 to *N*-1. The received signal at the n^{th} pulse after downconversion can be expressed as

$$s_{Rx}(\tilde{t},n) \cong p[\tilde{t} - \tau(n)]exp[-j2\pi f_c \tau(n)] + w(\tilde{t}) \quad (2.4)$$

where $\tau(n)$ is the round time delay between the moving target and the radar at time *nT*, defined as

$$\tau(n) = \tau_0 + 2vnT_r/c = 2(R_0 + vnT_r)/c \quad (2.5)$$

in which c denotes the velocity of light, v is the radial velocity between the target and the radar, R_o is the target range at the transmission time of the 1st pulse, i.e. n = 0.

Equation (2.4) is an approximation, because $\tau(n)$ is assumed to be constant during pulse repetition interval T_r. This approximation is acceptable, unless T_r is very long. *w(t)* represents bandpass complex white Gaussian noise with zero mean and variance σ^2. The input SNR is then defined as $1/\sigma^2$. In addition, we ignore the variation of scatterer range during the pulse interval T_o.

The Fourier transform (FT) of (2.4) over $\tilde{t}$ is

$$S(f,n) = P(f) \cdot exp[-j2\pi(f + f_c)\tau(n)] + W(f) \quad (2.6)$$

where $W(f)$ is the FT of $w(\tilde{t})$.

Multiplying $S(f,n)$ by FT of the matched filter (MF) impulse response gives

$$O(f,n) = Q(f)exp[-j2\pi(f + f_c)\tau(n)] + P^*(f)W(f) \quad (2.7)$$

where the matched filter impulse response is $h(t) = p^*(-t)$, and $P(f)$ is the FT of $p(t)$, $(.)^*$ denotes complex conjugate. Substituting $\tau(n)$, we have the following statement

$$O(f,n) = Q(f)exp[-j2\pi(f+f_c)\tau_0]exp\left[-j2\pi(f+f_c)\frac{2vnT_r}{c}\right] + P^*(f)W(f) \quad (2.8)$$

where $n = 0,1,\dots,N-1$.

There is obviously a coupling between the fast time frequency *f* and slow time *n* in the exponential term $exp\left[-j2\pi f\frac{2vnT_r}{c}\right]$ in (2.8), which means that there is range migration.

We can illustrate the range migration problem in fast time – slow time domain as a sketch plot shown in Figure 2.1, where amplitude of each pulse is shown in a row only for illustration purpose, and x-axis shows the range bins corresponding to fast time. It is obvious that arrival times of pulses are not confined in the same range bin. This is why simple addition of pulses without any correction leads to reduction in the amplitude of the output. Figure 2.2 depicts the case when the arrival times of the pulses are aligned. Note that the amplitudes of all pulses peak in the same range bin, so the pulses can be simply summed up and the effect of the range migration problem is mitigated.

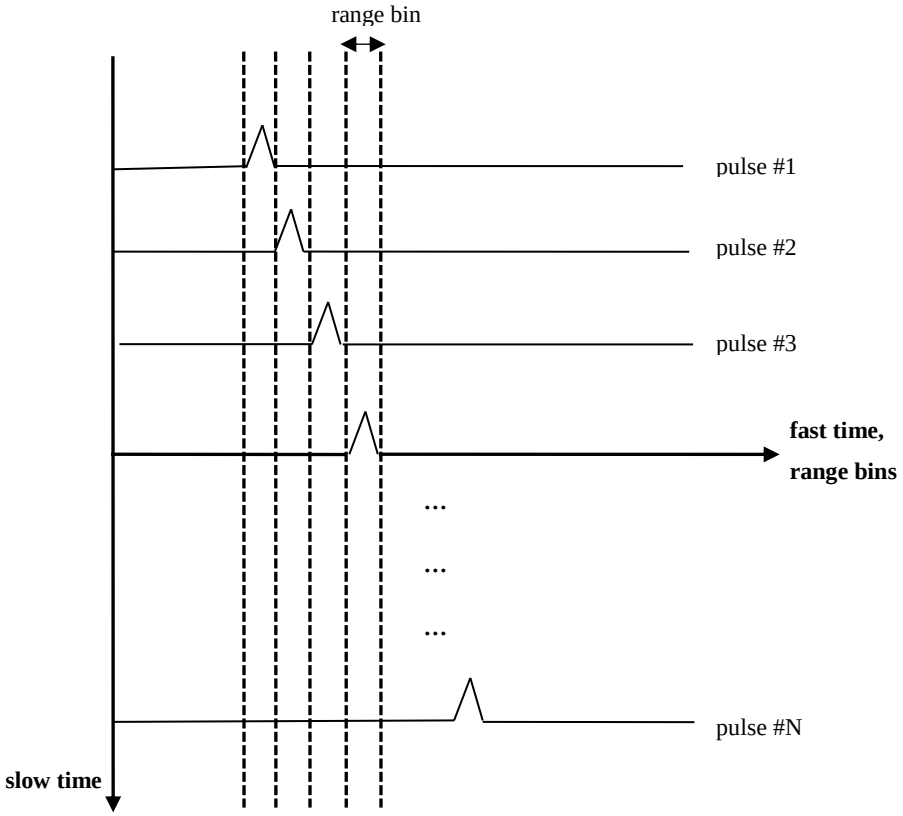

Figure 2.1 Illustration of range migration in fast time – slow time domain

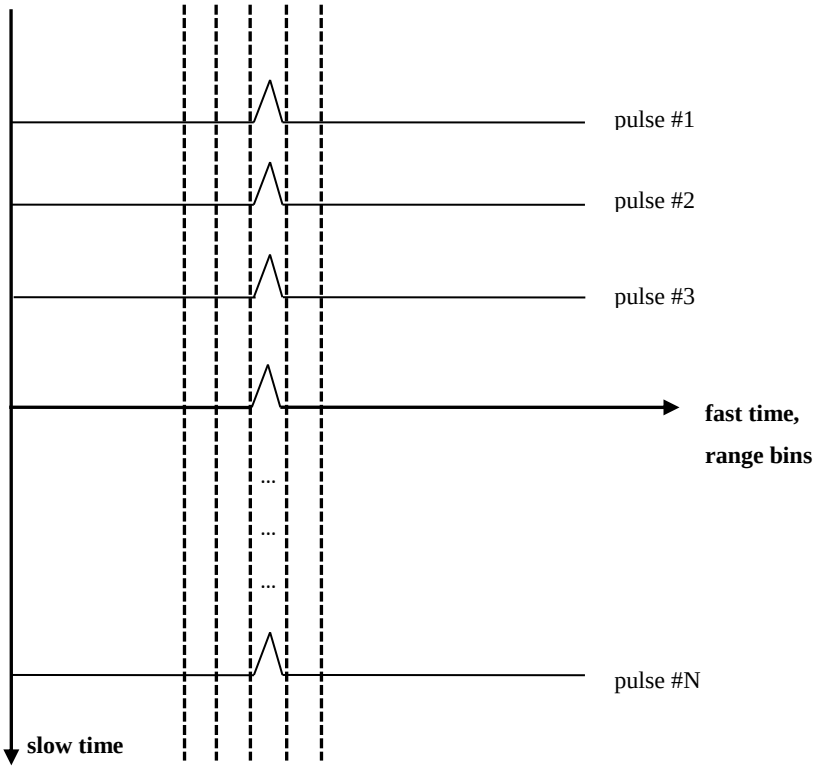

Figure 2.2 Illustration of pulses after range alignment

2.2 ANALYSIS AND IMPLEMENTATION ASPECTS OF KT

In this section we examine the KT algorithm, one of the well-known RMC algorithms, from analysis and implementation aspects.

2.2.1 RMC AND DOPPLER AMBIGUITY RESOLUTION VIA KT

The term $exp\left[-j\frac{4\pi}{c}fvnT_r\right]$ in (2.8) generates the range migration because *f* and *n* couple with each other. KT is employed to get rid of this coupling. Define the transform as

$$n = mf_c/(f_c + f) \tag{2.9}$$

This can be interpreted as the rescaling of axis *n* for each frequency *f*. Figure 2.3 shows the remapping process. The process is called "Keystone Transform" due to its Keystone shape [14].

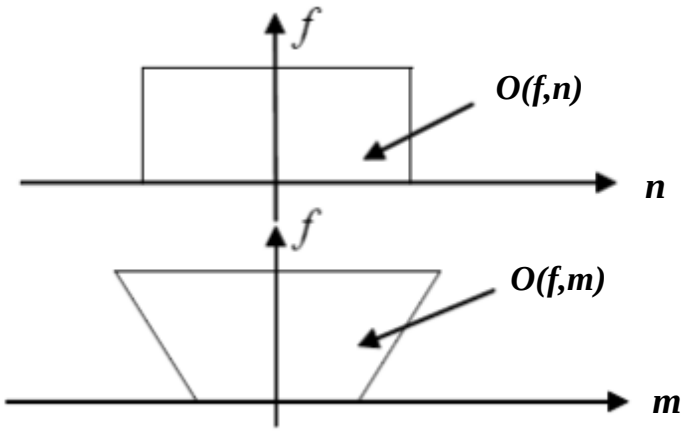

Figure 2.3. Transform of two dimensional data: the Keystone transformation.

Substituting (2.9) into (1.6), the rescaling operation is done and there is no more coupling between *f* and *m* axes:

$$\begin{aligned} O_{KT}(f,m) &= O\left(f,\frac{mf_c}{f_c+f}\right) \\ &= Q(f)exp[-j2\pi(f+f_c)\tau_0]exp\left[-j\frac{4\pi}{c}mf_cvT_r\right] + P^*(f)W(f) \end{aligned} \tag{2.10}$$

where $m = [0,1,\dots,N-1]\left(\frac{f_c+f}{f_c}\right)$.

Notice that the fast-time frequency f and the rescaled slow-time m are no more coupled. Hence, we eliminated the range migration by performing the KT.

In (2.10), $O_{KT}(f,m)$ is defined for non-integer values of m. We need to recover $O_{KT}(f,m')$ for integer values of $m' = 0,1,\dots,N-1$ by sinc interpolation based on truncating the Shannon interpolation formula as proposed in [16] and [17] ;

$$\begin{aligned} O_{KT}(f,m') &= \sum_{m=0}^{(N-1)\alpha} O_{KT}(f,m)sinc[m-m'] \\ &= \sum_{m=0}^{(N-1)\alpha} O(f,m/\alpha)sinc[m-m'] \end{aligned} \tag{2.11}$$

where $\alpha = \frac{f_c+f}{f_c}$.

Substituting $m = n\alpha$

$$O_{KT}(f,m') = \sum_{n=0}^{N-1} O(f,n)sinc[n\alpha - m'] \tag{2.12}$$

Effect of Doppler Ambiguity

High speed targets causes to significant Doppler ambiguity depending on the length of PRI. This would influence the compensation accuracy and hence integration effectivity. Hence, the KT requires a particular adaptation.

Let us inspect only the slow-time phase term $\frac{4\pi}{c} m f_c v T_r$ in $O_{KT}(f,m)$ of equation (2.10). Supposing the velocity *v* is low such that there is no Doppler ambiguity, we can rewrite the slow-time phase term, $exp\left[-j\frac{4\pi}{c} m f_c v T_r\right] = exp[-j2\pi m f_d T_r]$ where $f_d = \frac{2vf_c}{c}$ is the Doppler shift at frequency f_c. We now assume the target velocity is high enough to have Doppler ambiguity and folded over *F* times.

The slow-time phase term in $O_{KT}(f,m)$ becomes $exp\left[-j2\pi m(f_d - \frac{F}{T_r})T_r\right] = exp[-j2\pi m f_d T_r]$ again; there is no change in the desired result.

Let us examine the impact of Doppler ambiguity on the exponential coupling term of the matched filter output in equation (2.10)

$$exp\left[-j\frac{4\pi}{c}(f+f_c)vnT_r\right] = exp\left[-j2\pi\left[\frac{2v}{c}(f+f_c)-\frac{F}{T_r}\right]nT_r\right]$$
$$= exp\left[-j\frac{4\pi}{c}(f+f_c)vnT_r\right]exp[j2\pi Fn] \quad (2.13)$$

Although $exp[j2\pi Fn]$ equals to unity due to integer values of *F*, we have included this term to show the effect of rescaling the slow-time coefficient. After rescaling $n \rightarrow m$ to obtain $O_{KT}(f,m)$, the first slow-time phase term will be corrected to match the ideal result, however there will be an extra term because of the Doppler ambiguity:

$$exp\left[-j\frac{4\pi}{c}(f+f_c)vnT_r\right]exp[j2\pi Fn] \quad (2.14)$$
$$= exp\left[-j\frac{4\pi}{c}mf_cvT_r\right]exp\left[j2\pi F\frac{f_c}{(f_c+f)}m\right]$$

This equation shows that the corrected term must be considered in the case of ambiguity factor *F*, which is defined as

$$C(F) = \exp\left[-j2\pi F\frac{mf_c}{(f_c+f)}\right] \quad (2.15)$$

Then the KT algorithm in (2.12) is compensated by the multiplication by *C(F)* as

$$O_{KT-amb}(f,m) = C(F)O_{KT}(f,m) \quad (2.16)$$

After taking the inverse Fourier transform (IFT) in *f* domain, the range is compressed and the profiles are realigned as

$$o_{KT}(\tilde{t},m) = \text{IFT}\,[O_{KT-amb}(f,m)] \quad (2.17)$$

In the case of unknown Doppler ambiguity factor, the ambiguity compensation in (2.16) can be executed after coherent integration using all possible values of ambiguity factor *F*. In the end, we select the one giving the maximum amplitude peaks. As a remark, Doppler ambiguity can be searched for and found during detection phase. Namely, Doppler ambiguity factor is already known in the tracking mode of the radar, which allows us to significantly reduce the computational complexity of the KT algorithm during tracking.

Coherent Integration after Keystone Transform

Coherent integration can be carried out by taking discrete FT (DFT) of $o_{KT}(\tilde{t}, n)$ in (2.17) with respect to slow time *n*, as follows:

$$o_{KT}(\tilde{t}, k) = \sum_{n=0}^{N-1} o_{KT}(\tilde{t}, n) exp\left(-\frac{j2\pi nk}{N}\right) \tag{2.18}$$

where *k* is Doppler frequency index.

2.2.2 SPECIAL CASE: LFM SIGNAL

In this section we analyze the KT when the transmitted baseband signal is LFM, which will be the case in the simulations performed in this work.

The received signal at the nth pulse after downconversion, can be written as

$$s(\tilde{t}, n) = p[\tilde{t} - \tau(n)] exp[-j2\pi f_c \tau(n)] exp(-j2\pi f_d \tilde{t}) + w(\tilde{t}) \tag{2.19}$$

Suppose that the transmitting baseband signal of PD radar is LFM signal (chirp pulse) that is given as

$$p(t) = rect(t/T_0) exp(j\pi\mu t^2) \tag{2.20}$$

where T_0 is the pulsewidth, $\mu = \frac{B}{T_0}$ is the modulation rate, and *rect(t/ T_0)* is the rectangular function with duration T_0.

The Fourier transform (FT) of (2.19) over $\tilde{t}$ is

$$S(f,n) = P(f+f_d)\cdot exp[-j2\pi(f+f_c+f_d)\tau(n)] + W(f) \tag{2.21}$$

$$S(f,n) = P(f+f_d)\cdot exp\left[-j\frac{4\pi}{c}(f+f_c+f_d)(R_0+vnT_r)\right] + W(f) \tag{2.22}$$

The matched filter output can be represented as follows

$$O(f,n) = S(f,n)P^*(f) \tag{2.23}$$

FT of the chirp signal can be found applying stationary phase principle [23] as follows:

$$P(f) \cong rect\left(\frac{f}{B}\right)\exp(-\frac{j\pi f^2}{k}) \tag{2.24}$$

This approximation improves as the time-bandwidth product BT_0 increases. If $P(f)$ is substituted in (2.23)

$$O(f,n) = \frac{1}{\sqrt{k}} rect\left(\frac{f+\frac{f_d}{2}}{B-f_d}\right) exp\left(-j\frac{\pi}{k}{f_d}^2\right) exp\left\{-j2\pi f\left[\tau(n)+\frac{f_d}{k}\right]\right\} \times exp\{-j2\pi(f_d+f_c)\tau(n)\} + P^*(f)W(f) \tag{2.25}$$

Substituting (2.9) into (2.25), the rescaling operation is done and there is no more coupling between *f* and *m* axes

$$O_{KT}(f,m) = O(f,\frac{mf_c}{f_c+f})$$

$$= \frac{1}{\sqrt{k}} rect\left(\frac{f + \frac{f_d}{2}}{B - f_d}\right) exp\left(-j\frac{\pi}{k}{f_d}^2\right) exp\left\{-j2\pi f\left[\tau_0 + \frac{f_d}{k}\right]\right\}$$
$$\times exp(-j2\pi f_d m T_r)\, exp\{-j2\pi(f_d + f_c)\tau_0\} + P^*(f)W(f) \qquad (2.26)$$

After taking the IFT in *f* domain, range compression and realignment of profiles are completed as

$$o_{KT}(\tilde{t}, m) = \frac{(B - f_d)}{\sqrt{k}} sinc\left\{(B - f_d)\left(\tilde{t} - \tau_0 - \frac{f_d}{k}\right)\right\}$$
$$\times exp(-j\pi f_d \tilde{t})\ exp[-j\pi f_d \tau_0]$$
$$\times exp(-j2\pi f_c \tau_0)\, exp(-j2\pi f_d m T_r) + w'(\tilde{t}) \qquad (2.27)$$

Range Displacement due to Doppler Shift:

After eliminating the range migration, the maximum amplitude of the pulses in CPI are aligned to be in the same range bin at $\tilde{t} = \tau_0 + \frac{f_d}{k}$. This range bin corresponds to the range for the pulse $n = m = 0$. Substituting *k=B/ T0* and taking *B=1/dt*, peaks are found at

$$\tilde{t} = \tau_0 + \frac{f_d}{k} = \tau_0 + \frac{f_d T_0}{B} = \tau_0 + f_d \cdot T_0 \cdot dt \qquad (2.28)$$

where *dt* is the sampling period. Hence, there will be discretization loss, if $f_d \cdot T_0$ is not an integer.

In addition, the peak does not appear at $\tilde{t} = \tau_0$ as we desire. Rather, there will be a shift in fast time which is is proportional to the Doppler shift. The range measurement will include an error since the range is found depending on this peak time. The error in the range measurement can be written as

$$R_A = \frac{c\, f_d T_0}{2B} \tag{2.29}$$

Figure 2.4 shows that range displacement is proportional to Doppler shift. Range is measured as R_A instead of initial range R_0 between target and radar.

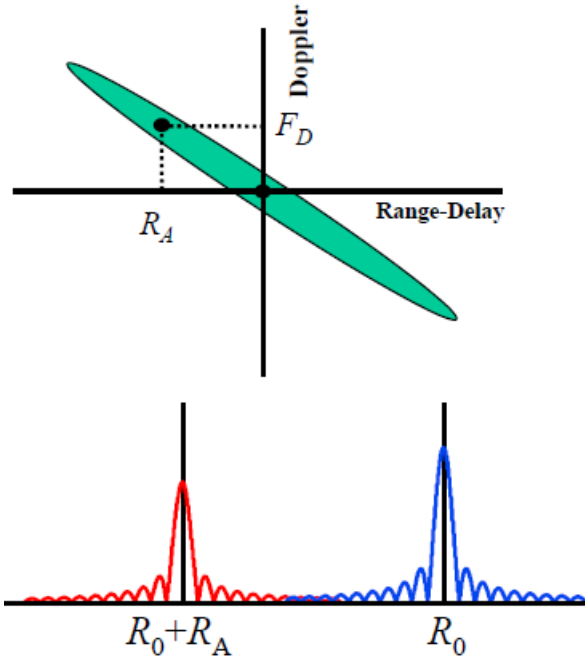

Figure 2.4. Illustration of the effect of range-Doppler coupling

Illustration of Rescaling in KT:

We provide an illustration of the rescaling operation in KT to make it hopefully clearer to readers.

The received signal at the n^{th} pulse after down conversion, can be rewritten as

$$s(\tilde{t}, n) = p[\tilde{t} - \tau(n)]e^{-j2\pi f_c \tau_0} exp[-j2\pi f_c n\Delta\tau] \tag{2.30}$$

The round-trip delay can be expressed as follows

$\tau(n) = 2\frac{R_0 + vnT_r}{c} = \tau_0 + n\Delta\tau$ and $\Delta\tau = \frac{2vT_r}{c}$

where v>0 implies a receding target.

The Fourier transform of $s(\tilde{t}, n)$ over $\tilde{t}$ is

$$S(f, n) = P(f)e^{-j2\pi(f+f_c)\tau_0} \cdot \exp[-j2\pi(f + f_c)n\Delta\tau] \tag{2.31}$$

where $P(f) = IFT\{p(t)\}$.

The matched filter output in fast time frequency domain can be expressed as

$$O(f, n) = P^*(f)S(f, n) \tag{2.32}$$

$$O(f, n) = Q(f)e^{-j2\pi(f+f_c)\tau_0} \cdot exp[-j2\pi(f + f_c)n\Delta\tau] \tag{2.33}$$

$$o(\tilde{t}, n) = q[\tilde{t} - \tau(n)]e^{-j2\pi f_c\tau_0}exp[-j2\pi f_c n\Delta\tau] \tag{2.34}$$

where $q(t)$, $Q(f)$ are defined in (2.2) and (2.3).

We recall that Keystone transform is defined as rescaling slow time index using $n = mf_c/(f_c + f)$. Namely, we obtain non-integers $m = 0, \frac{f_c+f}{f_c}, \frac{2(f_c+f)}{f_c} \dots, \frac{(N-1)(f_c+f)}{f_c}$ from integers $= 0,1, \dots, N-1$. After substituting $n = mf_c/(f_c + f)$ into $O(f, n)$ in (2.33), the rescaling operation is done and there is no more coupling between *f* and *m* axes

$$O_{KT}(f, m) = O(f, \frac{mf_c}{f_c + f})$$
$$O_{KT}(f, m) = Q(f)e^{-j2\pi(f+f_c)\tau_0} \cdot \exp[-j2\pi f_c m\Delta\tau] \tag{2.35}$$

The first exponential in this expression is a constant phase shift corresponding to round-trip time delay of the first pulse. The second exponential term $\exp[-j2\pi f_c m\Delta\tau] = \exp\left[-j4\pi f_c \frac{mvT_r}{c}\right]$ corresponds to the Doppler shift where mT_r represents slow time and v is the Doppler velocity. We do not have the exponential term $exp[-j2\pi fn\Delta\tau]$ representing coupling between f and n anymore.

Since m values are not integer, we find $O_{KT}(f,m)$ samples by interpolating $O(f,n)$ for each value of as shown in Figure 2.5. In this figure, black full-dots show $O(f,n)$ samples in range-frequency f and slow time index n domain, whereas red circles show $O_{KT}(f,m)$ samples in range-frequency f and slow time index m axes.

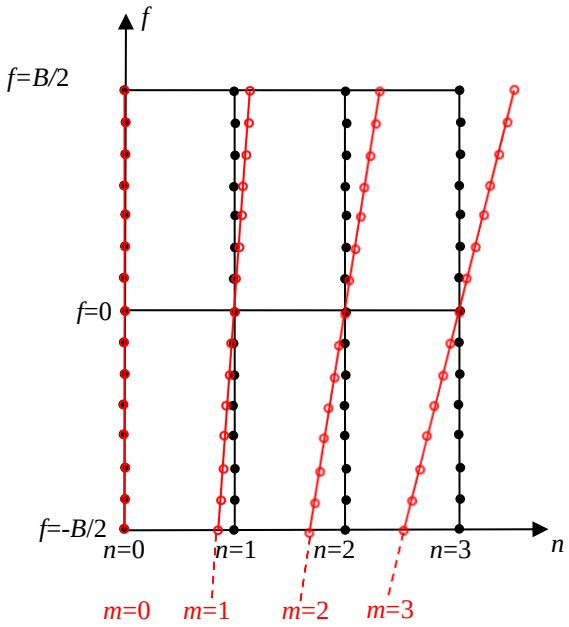

Figure 2.5 Illustration of KT in slow time - range frequency domain

We have shown in (2.26) that rescaling $O(f,n)$ eliminates the range migration. In order to find $O_{KT}(f,m)$ for integer values of m, we recover $O(f,n)$ for non-integer

values of *n*. We can recover by sinc interpolation based on truncating the Shannon interpolation formula as proposed in [16] and [17].

$$O_{KT}(f,m) = \sum_{n=0}^{N-1} O(f,n) sinc[n\alpha - m] \tag{2.36}$$

where $\alpha = \frac{f_c+f}{f_c}$.

In summary, $O(f,n)$ is given for $n \in \{0,1,\dots,N-1\}$, and we want to recover values for $n \in \{0,1/\alpha,\dots,(N-1)/\alpha\}$.

Ideally, desired interpolated signal will be as follows

$$O_{KT}(f,m) = O(f,\frac{m}{\alpha}) \tag{2.37}$$

for $m = 0,1,\dots,N-1$.

Figure 2.6 illustrates the interpolation operation in KT. Known samples of *O(f,n)* at $n = 0,1,2,\dots,N-1$ are shown by black full-circles, and, samples to be recovered at $n = 0,1/\alpha,\dots,(N-1)/\alpha$ are shown by red circles.

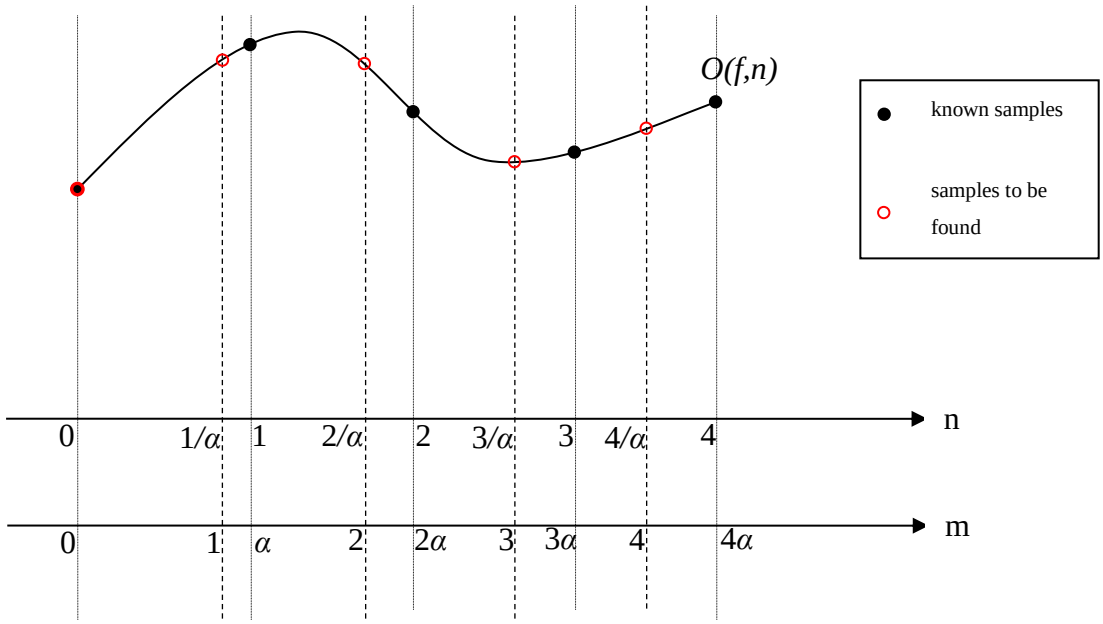

Figure 2.6. Illustration of interpolation in Keystone Transform

2.2.3 DISCRETE TIME ANALYSIS OF KT

We consider discrete time sampling of relevant signals in this section. Assume we have sampling period T_s and pulse repetition interval T_r is composed of L samples.

$$T_r = LT_s \tag{2.38}$$

Fast time sampling indices $l = 0,1,\dots,L-1$ can be represented as $\tilde{t} = lT_s$. The slow time index is $n = 0,1,\dots,N-1$. We can express received and down-converted signal $s(\tilde{t},n)$ in discrete-fast time as given

$$s_d[l,n] = s(lT_s,n) \tag{2.39}$$

where

$$s(\tilde{t}, n) = p(\tilde{t} - \tau(n)) e^{-j2\pi f_c(\tau_0 + n\Delta\tau)} \quad (2.40)$$

We can obtain 1-dimensional discrete signal in fast time domain by sampling $p(\tilde{t})$ with period T_s

$$p_{1d}[l] = p(lT_s) \quad (2.41)$$

Using Shannon interpolation formula [24], we can write

$$p(\tilde{t}) = \sum_k p_{1d}[k] sinc\left(\frac{\tilde{t} - kT_s}{T_s}\right) \quad (2.42)$$

Substituting $\tilde{t} - \tau(n)$ in place of $\tilde{t}$ in (2.42),

$$p(\tilde{t} - \tau(n)) = \sum_k p_{1d}[k] sinc\left(\frac{\tilde{t} - \tau(n) - kT_s}{T_s}\right) \quad (2.43)$$

We can define 2-dimensional continuous fast-time, discrete slow-time signal $p_c(\tilde{t}, n) = p(\tilde{t} - \tau(n))$. Then, we have following expression

$$p_c(\tilde{t}, n) = \sum_k p_{1d}[k] sinc\left(\frac{\tilde{t} - \tau(n) - kT_s}{T_s}\right) \quad (2.44)$$

We can obtain 2-dimensional discrete signal $p_{2d}[l, n]$ by sampling $p_c(\tilde{t}, n)$ with sampling period T_s.

$$p_{2d}[l, n] = p_c(lT_s, n) = p(lT_s - \tau(n)) \quad (2.45)$$

Then, we obtain following expression after substituting (2.44) in (2.45)

$$p_{2d}[l,n] = \sum_{k} p_{1d}[k] sinc\left(\frac{lT_s - \tau\,(n) - kT_s}{T_s}\right)$$

$$p_{2d}[l,n] = p_{1d}[l] * h_d[l,n] \tag{2.46}$$

where $h_d[l,n] = sinc\left(l - \frac{\tau\,(n)}{T_s}\right)$,

By employing (2.40), (2.45) and using the definition in (2.39), we can express $s_d[l,n]$ in the following form:

$$s_d[l,n] = p_{2d}[l,n] e^{-j2\pi f_c(\tau_0 + n\Delta\tau)} \tag{2.47}$$

Taking DFT along *l*,

$$S_d[k,n] = {}^{DFT}_{l}(s_d[l,n]) = \sum_{l=0}^{L-1} s_d[l,n] e^{-j2\pi kl/L} \tag{2.48}$$

where $k = 0,1, \ldots K-1$.

After substituting $s_d[l,n]$,

$$S_d[k,n] = e^{-j2\pi f_c(\tau_0 + n\Delta\tau)} \sum_{l=0}^{L-1} p_{2d}[l,n] e^{-\frac{j2\pi kl}{L}} \tag{2.49}$$

Since $p_{2d}[l,n]$ can be expressed as output of ideal fractional delay filter (FDF) as given in (2.46), we obtain the following expression by employing the ideal frequency response of FDF [25]

$$\sum_{l=0}^{L-1} p_{2d}[l,n]e^{-\frac{j2\pi kl}{L}} = DFT\{p_{2d}[l,n]\}$$
$$= P_{1d}[k]exp\left[-j2\pi\frac{k}{L}\frac{\tau(n)}{T_s}\right] \quad (2.50)$$

where $P_{1d}[k]$ is DFT of $p_{1d}[l]$ along l. Then,

$$S_d[k,n] = P_{1d}[k]exp\left[-j2\pi\frac{k}{L}\frac{\tau(n)}{T_s}\right]e^{-j2\pi f_c(\tau_0+n\Delta\tau)}. \quad (2.51)$$

DFT of the discrete-time matched filter output along discrete fast-time is

$$O_d[k,n] = P_{1d}{}^*[k]S_d[k,n], \quad (2.52)$$

$$O_d[k,n] = P_{1d}{}^*[k]P_{1d}[k]e^{-j2\pi\left(f_c+\frac{k}{LT_s}\right)\tau_0}e^{-j2\pi\left(f_c+\frac{k}{LT_s}\right)n\Delta\tau} \quad (2.53)$$

where $Q_d[k] = P_{1d}{}^*[k]P_{1d}[k] = |..|^2$ is the DFT of $q_d[k] = p_{1d}[l] * p_{1d}{}^*[-l]$. It is obvious that there is a coupling between the range frequency index *k* and the slow time index *n* in the exponential term $e^{-j2\pi\left(f_c+\frac{k}{LT_s}\right)n\Delta\tau}$ in (2.53), which causes the range migration.

We can define a new frequency $f_k = \frac{k}{LT_s}$ and substitute in $O_d[k,n]$

$$O_d[k,n] = Q_d[k]e^{-j2\pi(f_c+f_k)\tau_0}e^{-j2\pi(f_c+f_k)n\Delta\tau} \quad (2.54)$$

Now perform KT by $n = mf_c/(f_c + f_k)$

$$O_{d-KT}[k,m] = Q_d[k]e^{-j2\pi(f_c+f_k)\tau_0}e^{-j2\pi f_c m\Delta\tau} \quad (2.55)$$

where $m = 0,1,...,N-1$.

Note that there is no coupling between the range frequency index *k* and the slow time index *n*. Hence, the range migration has been removed and the derivation is valid for discrete time.

Sampling Theorem Perspective on KT:

The analytical derivation of KT is composed of two steps in the literature: (i) rescaling slow-time $= mf_c/(f_c + f)$, and (ii) compensating for the unwanted effect of rescaling in the case of the Doppler ambiguity. We find it helpful to show that the derivation can be done by using the sampling theorem, as it has not been found explicitly in the literature.

We rewrite the matched filter output in range frequency – continuous slow time domain referring to (2.8),

$$O(f, t_s) = Q(f)exp[-j2\pi(f + f_c)\tau_0]exp\left[-j2\pi(f + f_c)\frac{2vt_s}{c}\right] \qquad (2.56)$$

where t_s denotes slow-time. We define $x_c(t_s) = O(f, t_s)$ as 1-dimensional continuous slow-time signal for particular value of range frequency f.

To simplify the analysis, we assume that $x_c(t_s)$ is composed of only the coupling term as follows:

$$x_c(t_s) = exp\{j2\pi f_0 t_s\} \qquad (2.57)$$

where $f_0 = \left[\frac{2v}{c}(f + f_c) + \frac{F}{T_r}\right]$. We can include the Doppler ambiguity factor *F* in the expression in order to consider the effect of ambiguous Doppler referring to (2.13).

Actually, we have the MF output signal in discrete slow-time sampled by pulse repetition frequency (PRF) $f_{s1} = 1/T_r$. Sampling the signal $x_c(t_s)$ with a sampling frequency $f_{s1} = 1/T_r$, we obtain

$$\begin{aligned} x_{1d}[n] &= exp\{j2\pi f_0 T_r n\} \\ &= exp\left\{j2\pi\left[\frac{2v}{c}(f + f_c) + \frac{F}{T_r}\right]T_r n\right\} \end{aligned} \tag{2.58}$$

The expression $x_{1d}[n]$ shows the MF output signal in discrete slow-time. Since we want to get rid of the coupling between f and n in (2.58), the desired output is $exp\left\{j2\pi\left[\frac{2v}{c}f_c\right]T_r n\right\}$. The desired output can be obtained by sampling the continuous time $x_c(t_s)$ with another sampling frequency.

Thus, we sample continuous time $x_c(t_s)$ with sampling frequency $f_{s2} = \frac{f+f_c}{f_c T_r}$ to obtain

$$x_{2d}[n] = exp\{j2\pi f_1 T_r n\} \tag{2.59}$$

where $f_1 = f_c \frac{2v}{c}$.

In summary, we have samples of $x_{1d}[n]$ for n=0,1,...,N-1 and we want to reconstruct $x_{2d}[n]$.

After sampling $x_c(t_s)$ with a sampling frequency $f_{s1} = 1/T_r$,

$$x_1(t_s) = x_c(t_s)\sum_n \delta(t_s - nT_r) = \sum_n x_c(nT_r)\delta(t_s - nT_r) \tag{2.60}$$

$$x_{1d}[n] = x_c(nT_r) \tag{2.61}$$

where $\delta(\,)$ is the unit impulse function, or Dirac delta function. We refer to a system that implements the operation of (2.61) as an ideal continuous-to-discrete-time converter, and we show it in block diagram form as indicated in

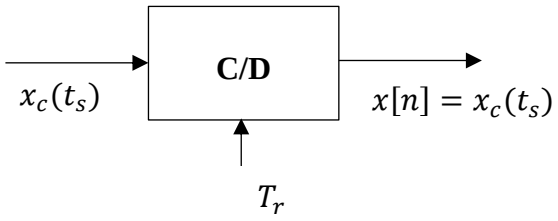

Figure 2.7 Block diagram representation of an ideal continuous-to-discrete-time (C/D) converter.

Continuous time FT (CTFT) of $x_c(t_s)$ and $x_1(t_s)$ can be written as

$$CTFT\{x_c(t_s)\} = X_c(f_s) = \delta(f_s - f_0) \tag{2.62}$$

where f_s denotes the frequency corresponding to slow-time.

CTFT of $x_1(t_s)$ can be found by employing $X_1(f_s) = \frac{1}{T_r}\sum_k X_c(f_s + kf_{s1})$ [26]

$$CTFT\{x_1(t_s)\} = X_1(f_s) = \frac{1}{T_r}\sum_k \delta(f_s - f_0 + kf_{s1}) \tag{2.63}$$

CTFT of $x_c(t_s)$ and $x_1(t_s)$ are given in Figure 2.8 and Figure 2.9.

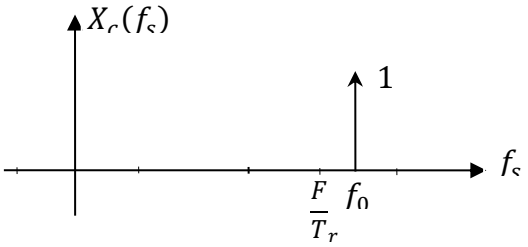

Figure 2.8. CTFT of $x_c(t_s)$

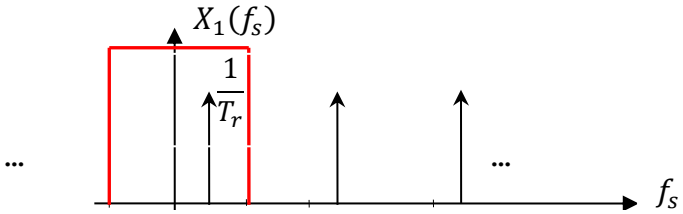

Figure 2.9. CTFT of $x_1(t_s)$

We can infer from Figure 2.8 and Figure 2.9 that $X_c(f_s)$ can be obtained by performing two operations on $X_1(f_s)$

(i) filtering $X_1(f_s)$ with a rectangular filter of width $1/T_r$ and multiplying by T_r,

(ii) shifting the output of (i) by $\frac{F}{T_r}$ in frequency domain

We can express these operations as follows:

$$X_c(f_s) = X_1\left(f_s - \frac{F}{T_r}\right) T_r rect\left((f_s - \frac{F}{T_r})T_r\right) \tag{2.64}$$

After taking IFT of (2.64) , we have

$$x_c(t_s) = exp\left(-j\frac{2\pi}{T_r}Ft_s\right)\left(x_1(t_s) * sinc\left(\frac{t_s}{T_r}\right)\right) \tag{2.65}$$

Substituting (2.60) in (2.65) ,

$$x_c(t_s) = exp\left(-j\frac{2\pi}{T_r}Ft_s\right)\left(\left(\sum_m x_c(t_s)\delta(t_s - mT_r)\right) * sinc\left(\frac{t_s}{T_r}\right)\right) \tag{2.66}$$

$$x_c(t_s) = exp\left(-j\frac{2\pi}{T_r}Ft_s\right)\sum_m x_c(mT_r)sinc\left(\frac{t_s - mT_r}{T_r}\right) \tag{2.67}$$

Substituting (2.61) into (2.67),

$$x_c(t_s) = exp\left(-j\frac{2\pi}{T_r}Ft_s\right)\sum_m x_{1d}[m]sinc\left(\frac{t_s - mT_r}{T_r}\right) \tag{2.68}$$

Hence, we can reconstruct $x_c(t_s)$ from $x_{1d}[n]$.

We finally obtain $x_{2d}[n]$ by sampling continuous time $x_c(t_s)$ with a sampling frequency $f_{s2} = \frac{f+f_c}{f_c T_r}$. Substituting $t_s = n\frac{f_c T_r}{f+f_c}$

$$x_{2d}[n] = \underbrace{exp\left(-j2\pi F\frac{f_c}{f+f_c}n\right)}\sum_m x_{1d}[m]sinc\left(n\frac{f_c}{f+f_c} - m\right) \tag{2.69}$$

Doppler ambiguity correction

Note that, the expression (2.69) includes the same operations given in (2.12), (2.15) and (2.16). Thus, we have shown the derivation of KT using the sampling theorem and we obtain the same result.

2.2.4 FAST IMPLEMENTATION WITH CZT

The application of KT to chirp signal using *sinc* interpolation kernel was presented in [16] and [17]. It is noted that when the accumulation time is long, the pulse number N will be very large. In that case, the algorithm is computationally burdensome. In [27] Chirp-Z interpolation algorithm was proposed and investigated in detail. In [22] a modified algorithm based on the fast implementation of KT using CZT algorithm is proposed. A fast KT using CZT is employed, whose main idea is to implement FFT over the slow time variable instead of interpolation and sequentially decreases the algorithm's complexity. In this section, we introduce CZT and provide a summary of the fast KT implementation method using CZT.

Review of CZT [28]

CZT employs the idea of expressing z-transform on a spiral contour as a discrete convolution and thus FFT operations can be used to compute the z-transform efficiently. CZT is the *K*-element z-transform of sequence *x(n)*, where *W* and *A* are scalars which specify the contour in the z-plane on which the z-transform is computed. *A* is the complex starting point, *W* is a complex scalar describing the complex ratio between points on the contour (point spacing). *A* and *W* are complex numbers are of the form $A = A_0 e^{j2\pi\theta_0}$, $W = W_0 e^{j2\pi\phi_0}$

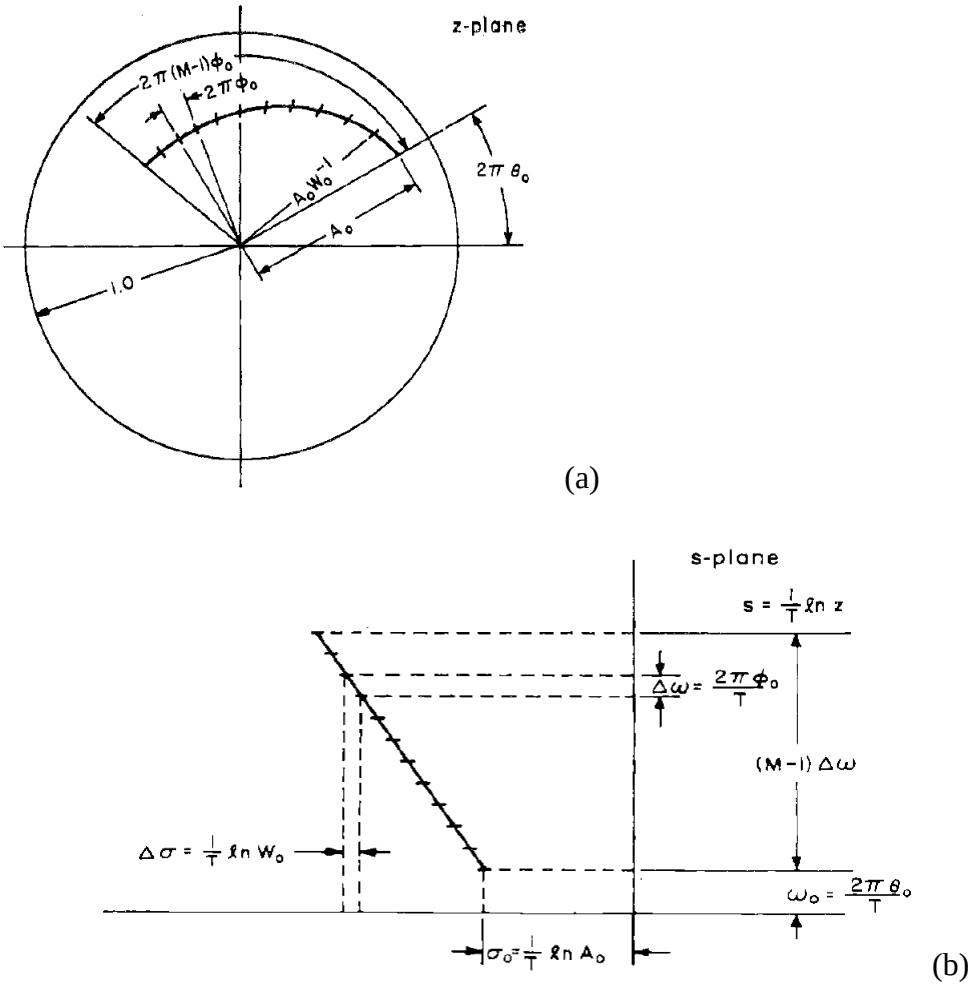

Figure 2.10. An illustration of independent parameters of the CZT: the correspondence of (a) a z-plane contour to (b) an s-plane contour through the relation $z = e^{sT}$.

Figure 2.10 illustrates the correspondence of (a) a z-plane contour to (b) an s-plane contour through the relation $z = e^{sT}$. The contour in the z-plane (a spiral or "chirp" contour) is described by

$$z_k = AW^{-k}, \qquad k = 1,2,\dots,K \tag{2.70}$$

K-point CZT of the *N* points input signal *x(n)* becomes

$$X[k] = \sum_n x(n)(AW^{-k})^{-n}$$
$$X[k] = \sum_n x(n)A^{-n}W^{nk} \tag{2.71}$$

Let us substitute $nk = \frac{n^2+k^2-(k-n)^2}{2}$ into (2.71)

$$X[k] = \sum_n x_n A^{-n} W^{(n^2/2)} W^{(k^2/2)} W^{-(k-n)^2/2} \tag{2.72}$$

In fact, (2.72) can be thought as a three-step process

1) Form a new sequence $y_n = x_n A^{-n} W^{(n^2/2)}$

2) Convolve y_n with the sequence defined as $v_n = W^{-n^2/2}$ to give a sequence

$g_k = \sum_n y_n v_{k-n}$

3) Multiply g_k with $W^{k^2/2}$ to give $X[k]$: $X[k] = g_k W^{k^2/2}$

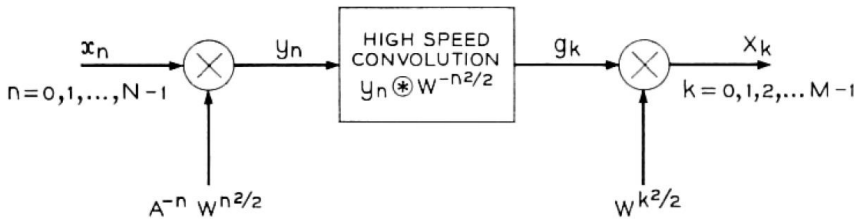

Figure 2.11. Implementation of the CZT as a circular convolution

The implementation of the CZT as a circular convolution is demonstrated in Figure 2.11.

Implementation of the CZT can be done by a circular convolution operation or equivalently as two FFT, one IFFT and four complex multiplication operations (see Figure 2.12). Since we will have constant values for W, we will need to take FFT of

$W^{-n^2/2}$ at only first time step. Hence, 1 FFT, 1 IFFT and 4 complex multiplications will be sufficient for CZT operation.

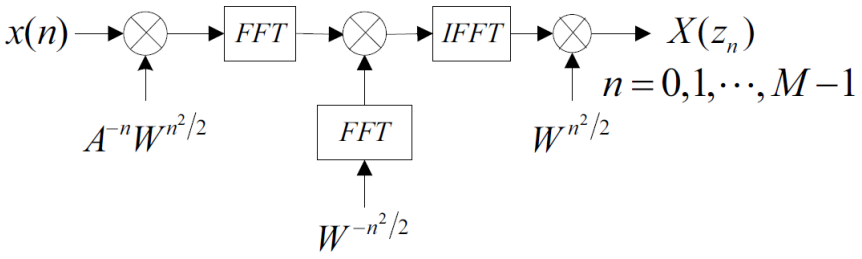

Figure 2.12. Implementation of the CZT using FFT's

KT Implementation using CZT

In KT implementation, the CZT parameters A and W are set as

$$A = 1 \qquad W = e^{\left(-j\frac{2\pi(f+f_c)}{N\ f_c}\right)} \tag{2.73}$$

Since we take $A = 1$, the contour in the z-plane is not a spiral any more. We take z-transform on the unit circle as in Discrete Fourier Transform (DFT), the difference with respect to DFT is the spacing between points on the contour. Figure 2.13 shows the contour in the z-plane where the phase distance between points is $\frac{2\pi}{N}\frac{(f+f_c)}{f_c}$.

We note that when the radar is in tracking mode it is not necessary to search the entire velocity range as the velocity is already found during detection and we assume that the velocity does not change significantly from detection to tracking mode.

Consequently, the contour becomes only an arc on the unit circle instead of a full circle. Therefore, it brings less computational complexity in tracking mode.

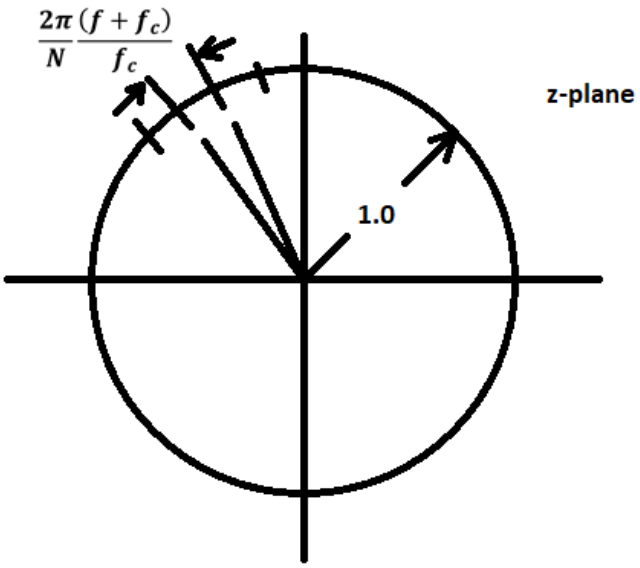

Figure 2.13 Illustration of the CZT parameters to be set for KT in z-plane

In the standard KT implementation, the compensation of the Doppler ambiguity is usually performed after KT, as shown (2.16). However, Doppler ambiguity compensation is done prior to CZT in the KT implementation via CZT [22].

$$O_{amb}(f,n) = C(F)O(f,n) \tag{2.74}$$

where $C(F)$ and $O(f,n)$ are given in (2.15) and (2.8), respectively.

CZT of $O_{amb}(f,n)$ is taken along slow-time n,

$$O_{czt}(f,k) = CZT_n\{O_{amb}(f,n)\} \tag{2.75}$$

where k is the Doppler frequency index.

Then, we can obtain coherent integration output in fast-time, Doppler frequency domain by taking IFT of $O_{czt}(f,k)$ in range frequency f,

$$y_{coh-czt}(\tilde{t},k) = IFT_f\{O_{czt}(f,k)\} \tag{2.76}$$

Unlike KT via sinc interpolation, we do not need to take FFT over slow-time for coherent integration when we apply KT using CZT. Figure 2.14 shows block diagrams of KT algorithm utilizing sinc and CZT interpolation algorithms.

The CZT eliminates the need for interpolation, while providing the desired point spacing. The FT over slow time with different granularity can be performed by the CZT algorithm using FFT. The KT algorithm utilizing CZT achieves high speed in real-time processing due to fast FFT operations.

According to [22], the interpolation algorithm given in [16] demands the following number of complex multiplications: $MN^2 + (MN/2)\log_2(N)$,whereas the KT using CZT requires the following number of complex multiplications: $M \times (L + 2N + (3/2)L\log_2 L + (3/2)N\log_2(N))$, where L should satisfy the equation $L = 2^m$, and $L \geq 2N - 1$.

In summary, it has been shown that fast KT based on CZT has less computational complexity.

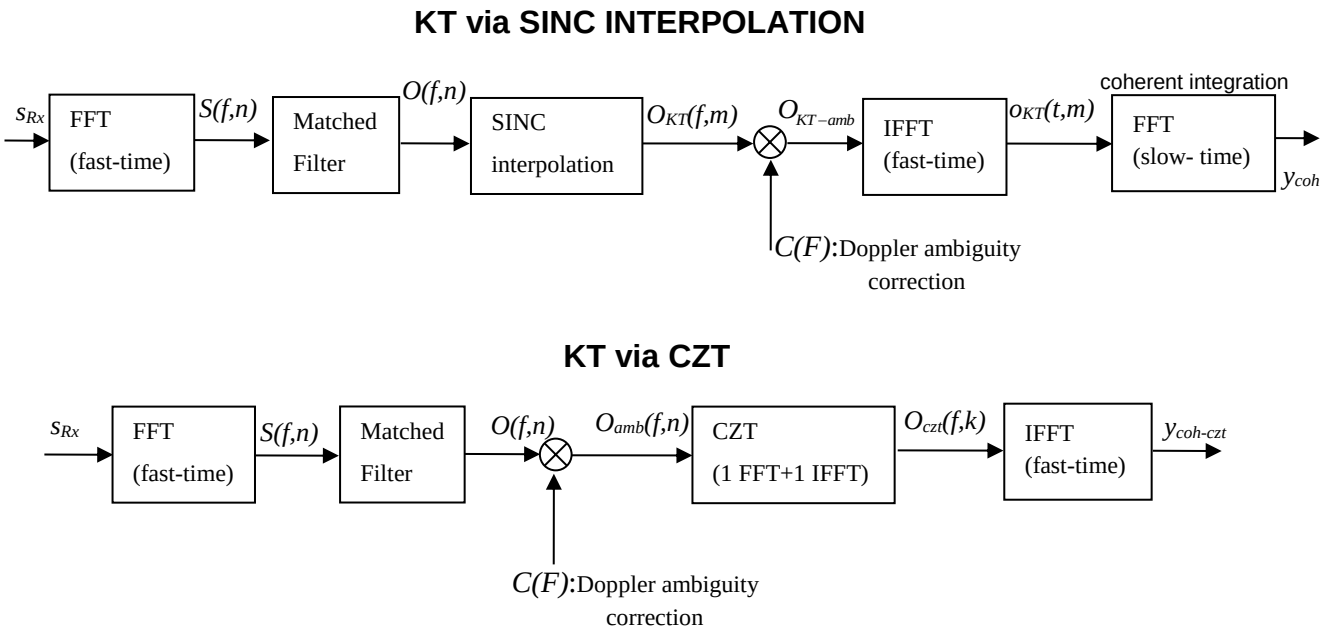

Figure 2.14 Comparison of implementations of KT via sinc interpolation and CZT

2.3 ANALYSIS AND IMPLEMENTATION ASPECTS OF RFT

In this section, we examine the RFT algorithm, one of the well-known coherent integration methods for the moving targets with range migration, from analysis and implementation aspects. Before analyzing the RFT in detail, it is helpful to review briefly the inspirational method Radon transform (RT) and a method very similar to RT, the Hough transform.

2.3.1 Radon Transform [29]

The Radon transform (RT) takes his name from J. Radon who presented the description of a function in terms of its (integral) projections [30]. The most famous RT application is in medical imaging, providing the theoretical principles for

computerized tomography devices. Nevertheless, there are also other RT applications in numerous fields such as radar signal processing [31] [32] [3]. Carretero-Moya [3] proposed to employ RT to detect small-targets in sea clutter.

A typical coordinate system for setting up the Radon transform is the following. Figure 2.15 shows a line L_ρ in R^2 with distances from the origin O = (0,0) in x,y-plane is further characterized by an angle θ where $B = (\rho\cos\theta, \rho\sin\theta)$ is a fixed point on L.

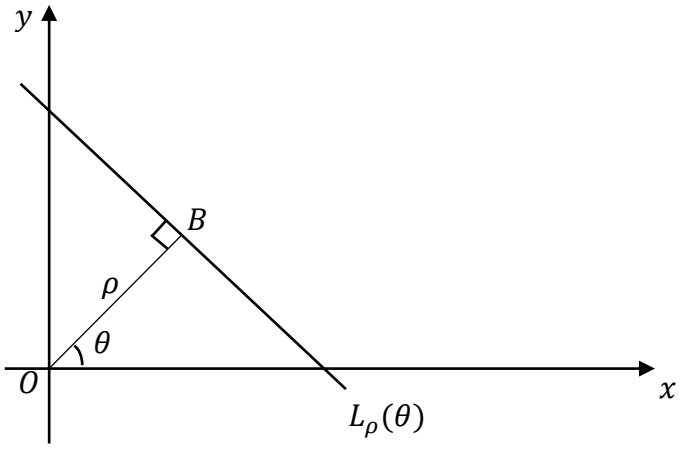

Figure 2.15. Typical coordinate system for the RT

So each line has two parameters , θ . Let $A = (x, y)$ denote a variable point on $L_\rho(\theta)$. Then, if the distance from *A* to *B* equals *t*, we have

$$\begin{aligned} x &= \rho\cos\theta - t\sin\theta \\ y &= \rho\sin\theta + t\cos\theta \end{aligned} \tag{2.77}$$

To define the Radon transform we assume that $f: \mathbb{R}_2 \to \mathbb{R}$ is continuous and integrable, and we write

$$Rf(\rho,\theta) = \int_{-\infty}^{\infty} f(x,y)dt, \quad (x,y) \in L_\rho(\theta) \tag{2.78}$$

In general, the RT $Rf(\rho,\theta)$ of a two-dimensional function $f(x,y)$ is calculated by integrating along slanted lines:

$$Rf(\rho,\theta) = \iint_{-\infty}^{\infty} f(x,y)\,\delta(\rho - x\cos\theta - y\sin\theta)dxdy \tag{2.79}$$

where δ is the Dirac delta function.

The line-like features on the input image appears as single points in $\rho - \theta$ space after taking Radon transform. Indeed, the RT is a well-known feature detector especially for finding lines in a noisy background.

2.3.2 Hough Transform [33]

Paul Hough proposed the Hough transform (HT) [34] to detect complex patterns in binary image processing. There are also some applications of the HT in radar signal processing. Carlson [6] [7] [8] introduced the HT based methods for noncoherent integration of range migrating targets.

The HT implementation utilizes the parametric representation of lines passing through a point in the image plane indexed by x-y coordinates. Figure 2.16 shows an illustration of HT of a straight line. A point *P(x,y)* in the image plane is defined by a set of intersecting lines at *P(x,y)*. Each line passing through can be represented by its parametric representation using

$$\rho = xcos\theta + ysin\theta \tag{2.80}$$

where (x,y) is the pixel coordinate in the image plane, ρ is the length of the perpendicular from the origin to the line, and θ is the angle made by the perpendicular with the x-axis. Every line that passes through *P(x,y)* is represented by a unique $\rho - \theta$ combination. These $\rho - \theta$ values are used to create a two

dimensional parametric space called Hough space where a point in image space is represented by a sinusoidal curve.

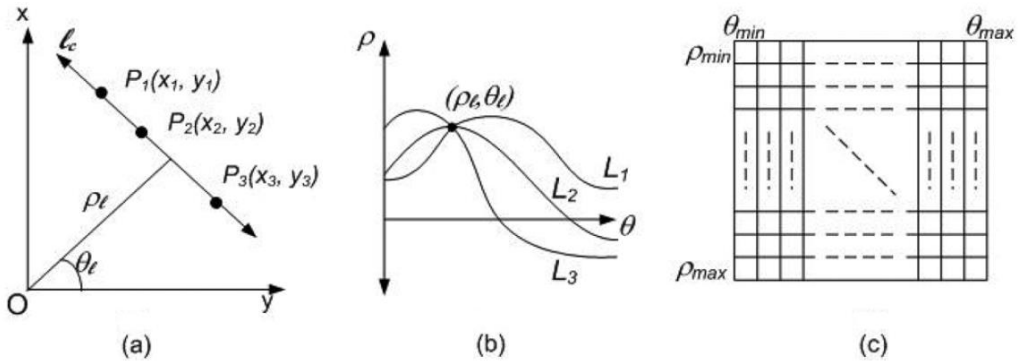

Figure 2.16. Straight line Hough transform. (a) Collinear points in image plane. (b) Intersecting sinusoids in Hough space. (c) Implementation as a two-dimensional array of accumulators.

The Hough transform can be used to detect collinear points by studying the Hough space as shown in Figure 2.16 (b). Points $P_1(x,y)$, $P_2(x,y)$, and $P_3(x,y)$, lying on the same line, share the same $\rho - \theta$ combination, $\rho_l - \theta_l$, which implies that the sinusoidal curves of the collinear points intersect in the Hough space.

The Hough transform is generally applied on an edge map to detect straight lines. It is implemented using a two-dimensional $\rho - \theta$ accumulator array as shown in Figure 2.16 (c). For every edge pixel coordinate, the ρ values are computed for angles from θ_{min} to θ_{max} , and the bins corresponding to these $\rho - \theta$ combinations are incremented. After processing the entire edge map, the array is scanned for accumulators that give high values or peaks. A peak in the array represents intersection in the parametric space and hence a straight line in the edge map.

2.3.3 The Relation between RT and HT

The Radon and Hough transforms are very closely related. According to van Ginkel [35], both RT and HT are mappings but in two different paradigms: reading and writing. In RT, we consider how a data point in the destination space is obtained from the data in the source space: *the reading paradigm*. In HT, we consider how a data point in the source space maps onto data points in the destination space*: the writing paradigm*. Another difference is that the HT is a discretization of the (continuous) RT. Usually, the RT is considered in the context of computed tomography, and the HT is considered in that of shape detection.

2.3.4 Radon Fourier Transform [19]

The integration loss of the Hough transform (HT) and Radon transform (RT)-based methods can be large compared to a coherent integration method because the phase fluctuation is not compensated for [36] [33] [6] [7] [8]. Therefore, it cannot be used when the SNR is extremely low. RFT [19] [20] [21] has been proposed to perform long-time coherent integration while there is linear range migration. RFT-based method is an optimal detector under the white Gaussian noise background [21]. However high peak blind speed side lobes (BSSL) can exist in the RFT-output [20].

Target's energy is concentrated to a focused peak in 2-dimensional space by jointly searching along velocity and range of the moving target.

We assume that a radar transmits LFM signal and signal model is as given in (2.4) and (2.20). The range between the radar and the target can be expressed as given:

$$R(t_s) = R_0 + vt_s \tag{2.81}$$

where v denotes the radial velocity between the target and the radar, t_s is the slow-time, and R_o is the range location of the target when the first pulse was emitted, i.e., at time $t_s = 0$.

After substituting (2.20) and (2.81) in (2.4), two-dimensional echoes of received signal is as follows:

$$s(\tilde{t}, t_s) = A_r rect\left(\frac{\tilde{t} - \frac{2R(t_s)}{c}}{T_0}\right) exp\left(j\pi k\left(\tilde{t} - \frac{2R(t_s)}{c}\right)^2\right) exp\left(-\frac{j4\pi f_c R(t_s)}{c}\right) \quad (2.82)$$

where A_r is the complex amplitude of the echo.

The matched filter impulse response is $h(t) = p^*(-t)$ where $p(t)$ is given as in (2.20). After the pulse compression, the target's 2-dimensional echoes:

$$s(\tilde{t}, t_s) = A_{rm} sinc\left(\pi B\left(\tilde{t} - \frac{2R(t_s)}{c}\right)\right) \exp\left(-\frac{j4\pi f_c R(t_s)}{c}\right) \quad (2.83)$$

where $A_{rm} = BT_0A_r$. Substituting $r = c\tilde{t}/2$

$$s(r, n) = A_{rm} sinc\left(\frac{2\pi B\left(r - R(t_s)\right)}{c}\right) \exp\left(-\frac{j4\pi f_c R(t_s)}{c}\right) \quad (2.84)$$

We define relative ranges with respect to a pre-set range center R_c:

$$R(t_s) = (R_0 - R_c) + R_c + vt_s = R_{sT} + R_c + vt_s \quad (2.85)$$

where the initial relative range $R_{sT} = R_0 - R_c$. Define $r_s = r - R_c$ and substitute (2.85) into (2.84), we have

$$s(r_s, t_s) = A_T sinc\left(\frac{\pi\left(r_s - R_s(t_s)\right)}{\rho_r}\right) \exp(-2\pi f_d t_s) \tag{2.86}$$

where $R_s(t_s) = R_{sT} + vt_s$, $\rho_r = \frac{c}{2B}$ is the range resolution, A_T is a complex backscattering coefficient.

From (2.86), it is seen that $s(r_s, t_s)$ has peak amplitude values when $r_s = R_s(t_s) = R_{sT} + vt_s$ holds. The equation $r_s = R_{sT} + vt_s$ corresponds to a straight line with a slope v in the $t_s - r_s$ plane. In other words, the range-compressed echoes of the moving target are approximately distributed along a straight line in the $t_s - r_s$ plane. From Figure 2.17, the target's range migration line in the $t_s - r_s$ plane may also be found by other two parameters (ρ, θ), where polar angle θ is defined as the anticlockwise angle from the range walk line to nT_r-axis as $\theta = cot^{-1}(-v)$. Also, polar distance ρ is defined as the minimum distance between the range walk and the $t_s - r_s$ plane origin as $\rho = R_{sT} \sin\theta$.

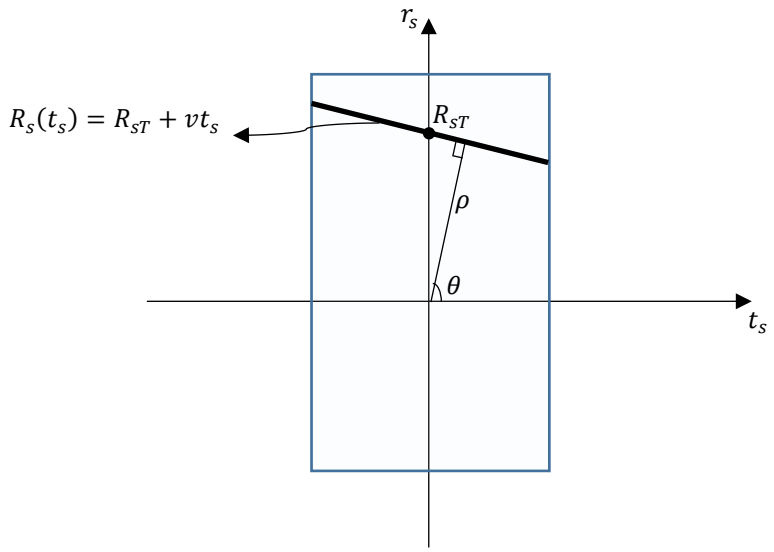

Figure 2.17. Representation of the moving target's range-compressed echoes, which are approximately distributed along a straight line in the $t_s - r_s$ plane.

We define Doppler filter function

$$H_{\theta_T}(t_s) = \exp\left(j\frac{4\pi f_c \cot(\theta)\, t_s}{c}\right) \tag{2.87}$$

Reminding that $v = -\cot(\theta)$, this filter can be used to compensate phase differences due to Doppler changes along slow time. Then, we introduce a kind of special integration on $s(r_s, t_s)$ as

$$G_{\rho\theta}(\rho, \theta) = \iint s(r_s, t_s)\, \delta(\rho - t_s \cos\theta - r_s \sin\theta) H_{\theta_T}(t_s) dt_s dr_s \tag{2.88}$$

Coherent integration of the pulses during integration interval is done via (2.88). RT of $s(r_s, t_s)$ is given for comparison as

$$R_{\rho\theta}(\rho, \theta) = \iint s(r_s, t_s)\, \delta(\rho - t_s \cos\theta - r_s \sin\theta) dt_s dr_s \tag{2.89}$$

Obviously, we have $\left|G_{\rho\theta}(\rho,\theta)\right| \geq \left|R_{\rho\theta}(\rho,\theta)\right|$ because the phase differences between pulses are not compensated for (2.89).

2.3.5 LOW COMPLEXITY RFT DETECTOR USING CZT [21]

In this section, an efficient RFT implementation proposed by Yu et. al [21] is reviewed. The standard RFT implementation may require considerably high computational load for high number of pulses during CPI. CZT has been employed for parameter searching to reduce complexity of the RFT detector.

Suppose s_{mn} is transmitted signal with slow-time index m and fast-time index n ($m = 1, \dots, M;\ n = 1, \dots, N$). Then these received echo samples can be represented as a binary decision problem as given

H_0: $x_{mn} = w_{mn}$

H_1: $x_{mn} = s_{mn} + w_{mn}$

where x_{mn} are received echoes, w_{mn} is white Gaussian noise, H_0 and H_1 are the hypotheses for target and no target, respectively.

A low complexity detector can be implemented in four steps as described below:

Step 1:

An FFT operation is performed along the fast time axis.

$$X_{m\hat{n}} = FFT_n\{x_{mn}\} \tag{2.90}$$

where $\hat{n}$ is the range frequency index.

Step 2:

Matched filtering is accomplished in the discrete-frequency-domain as

$$Y_{m\hat{n}} = H_{\hat{n}} X_{m\hat{n}} \tag{2.91}$$

where $H_{\hat{n}} = FFT_n\{p^*(-nT_s)\}$ is the frequency response of the matched filter, T_s is the sampling period, and $p(t)$ is the transmitted baseband signal. Then we have the matched filter output $Y_{m\hat{n}}$ obtained in frequency domain.

Step 3:

We can compensate the phase differences between the received pulses (due to the motion of the target) and integrate for each range frequency index.

$$Z_{k\hat{n}} = \sum_m C_{\hat{n}}^{km} Y_{m\hat{n}} \tag{2.92}$$

where $C_{\hat{n}} = exp\left(j4\pi\Delta v \frac{f_c + f_{\hat{n}}}{c} T_r\right)$, $k = -\frac{N_v}{2} + 1, \dots, \frac{N_v}{2}$ is velocity search index, Δv is the velocity search resolution, $f_{\hat{n}}$ is the range frequency, N_v is the number of searched velocities. We remind that frequency response of matched filter output includes the exponential term $exp\left(-j2\pi vn \frac{f_c + f_{\hat{n}}}{c} T_r\right)$ as given in (2.8). Consequently, $C_{\hat{n}}$ is employed for compensation of this term.

Thus, we apply a Doppler filter to compensate phase differences for each possible velocity cell as we show for standard RFT in (2.87).

Note that (2.92) is CZT of $Y_{m\hat{n}}$ as given in definition of CZT (2.71). Thus, RFT employs CZT for searching velocity by setting CZT parameters as $A = 1$ and $W = exp\left(j4\pi\Delta v \frac{f_c + f_{\hat{n}}}{c} T_r\right)$.

$$\begin{aligned} Z_{k\hat{n}} &= \sum_m C_{\hat{n}}^{(\frac{1}{2})(m^2 + k^2 - (m-k)^2)} Y_{m\hat{n}} \\ &= C_{\hat{n}}^{(\frac{1}{2})k^2} \sum_m C_{\hat{n}}^{-(\frac{1}{2})(m-k)^2} \left(C_{\hat{n}}^{(\frac{1}{2})m^2} Y_{m\hat{n}} \right) \\ &= C_{\hat{n}}^{(\frac{1}{2})k^2} \left(C_{\hat{n}}^{-(\frac{1}{2})m^2} * \left(C_{\hat{n}}^{(\frac{1}{2})m^2} Y_{m\hat{n}} \right) \right) \end{aligned} \tag{2.93}$$

Since (2.93) is a convolution operation, we can rearrange using FFT and IFFT operations.

$$Z_{k\hat{n}} = C_{\hat{n}}^{k^2/2} IFFT_m \left\{ FFT_m \left\{ C_{\hat{n}}^{-m^2/2} \right\} \cdot FFT_m \left\{ C_{\hat{n}}^{m^2/2} Y_{m\hat{n}} \right\} \right\} \tag{2.94}$$

which equals to $Z_{k\hat{n}} = CZT\{Y_{m\hat{n}}\}$. $Z_{k\hat{n}}$ yields maximum coherent integration magnitude when the searching velocity index k corresponds to the true velocity.

Step 4:

Coherent integration output in range-Doppler frequency domain can be obtained by taking IFFT of CZT output along range frequency. We have test statistic

$$T_{kn} = |IFFT_{\hat{n}}\{Z_{k\hat{n}}\}| \tag{2.95}$$

Binary decision can be done by comparing the test statistic with a certain threshold.

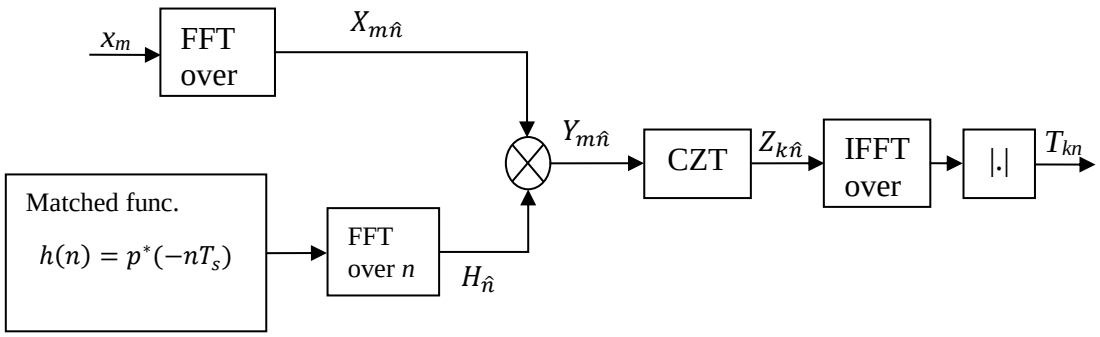

Figure 2.18. Low complexity RFT detector

Figure 2.18 shows implementation steps of the fast RFT detector in a block diagram.

For comparison, the computational complexity of the standard RFT is $O(N_v MN)$ and that of the RFT employing CZT is $NJ\log J$ where $J = M + N_v$, N is the number of range bins in PRI, M is the number of pulses to be integrated, N_v is the number of searched velocities. Accordingly, RFT can be implemented efficiently by using CZT for searching for parameters.

CHAPTER 3

EVALUATION OF KT IN REALISTIC ENVIRONMENT (TARGET FLUCTUATION AND CLUTTER)

We examine the performance of the KT in realistic environments such as clutter and target fluctuation in this chapter. Firstly, we introduce sea and rain clutter models, and clutter suppression methods. Secondly, we provide background information about target fluctuation models. Then, we investigate the detection of fluctuating targets in case of range migration. Next, we examine the range migration problem in sea and rain clutter. Finally, we look over the detection of range migrating targets in range migrating clutter, and propose an efficient method to remove jointly the target's and clutter's range migration.

3.1 Clutter Modeling and Suppression

In this section, we present background information about rain and sea clutter models, and explain methods and metrics for radar clutter suppression.

3.1.1 Sea Clutter Model [37]

It is unavoidable for radars working in sea to come across returned signals from the sea surface, generally called sea clutter. Sea clutter is undesired for many applications due to interference with the desired backscattering from the target. It is essential for the radar system designer to comprehend the characteristics of sea clutter in order to acquire appropriate signal processing approaches and to estimate performance in various cases. In order to fulfil this aim, it is an important task to develop statistical clutter models. These models have to be capable of combining the

spatial and temporal properties of the return for broad range of environmental conditions and various radar properties.

The clutter backscatters can be characterized by using many features including

- the area reflectivity, σ^0
- the amplitude distribution of the clutter amplitudes or power
- the Doppler spectrum of the clutter returns
- the spatial variation of the clutter return

3.1.1.1 Sea Clutter Reflectivity

The area reflectivity σ^0 is described by mean value of radar cross-section (RCS) of the backscatters divided by unit area. The clutter RCS can be found by $\sigma^0 A$ if the illuminated surface area is A. Due to continuously varying and composite structure of the sea surface, there is a large fluctuation around the average RCS σ^0.

3.1.1.2 Amplitude Statistics of Sea Clutter

The average clutter power is represented by the area reflectivity σ^0. The instantaneous power received from a particular resolution cell changes around the average value. Two components mainly cause the reflectivity to fluctuate:

1. The change in local surface shape, grazing angle, ripple density, and other factors associated with the passage of long waves and swell, cause the return from local tiny surfaces to change around the average reflectivity.

2. There are returns from lots of tiny structures in a single resolution cell, and there is a relative motion with respect to each other. Hence, this causes the returns to interfere. (usually called speckle).

Speckle is usually defined as a uniform field of numerous random scatterers that shows Gaussian scattering statistics.

We usually model the clutter as speckle when the sea swell wavelength is much less than the resolution cell and grazing angle is less than ten degrees. The amplitude distribution is Rayleigh in this case. The clutter‘s temporal decorrelation time is reasonably short, about between five and ten msec. Also, the clutter decorrelates reasonably well between pulses for frequency agile radars.

When the grazing angle decreases, and the radar resolution gets larger, the amplitude distribution of the clutter starts to have a longer ‘tail’. In such a case, the clutter backscatters are generally called to become spiky and the clutter pdf is characterized by K-distribution.

Not only does the clutter of high resolution radar resemble no longer like a Rayleigh distribution, but the correlation characteristics in time and space also becomes dissimilar to the correlation characteristics of speckles. Especially, the decorrelation of clutter with frequency agility does not exist anymore. The longest correlation times are observed in seconds instead of milliseconds.

The compound K-distribution [37] model represents the clutter with two components: (i) a relatively slowly changing underlying intensity *z* which is gamma distributed (ii) a more rapidly changing multiplicative noise component which modulates the underlying mean level. This component *x* has a Rayleigh distributed probability density function.

3.1.1.3 Spatial Correlation in Sea Clutter

There is a close relationship between the correlation of the clutter in space and the sea swell or sea wave patterns.

The correlation length of the sea surface in the range direction is denoted by ρ, and considered as a length characteristic of wind waves. It is found that [38]:

$$\rho = \frac{\pi}{2}\frac{W^2}{g}(3cos^2\theta + 1)^{1/2} \tag{3.1}$$

where θ is the angle between the line of sight and the wind direction, W is wind velocity W, and g is the gravitational acceleration.

Mostly, the effect of the correlation of the slowly varying gamma component on the radar performance is more important [39]. Due to this reason, it is more important to pay attention while generating gamma distributed random processes with determined correlation statistics.

3.1.1.4 Temporal Correlation in Sea Clutter

The form of the correlation between pulses is described by the use of the composite model: over a short period the reflected signals from any clutter resolution cell are always Rayleigh-distributed, indicating a return from multiple scatterers, and this speckle component has a Chi-distributed underlying average value, which describes, e.g. , the average value variation of clutter spikes or the periodic amplitude change while looking up or down the sea swell. The speckle component from any single resolution cell has a short temporal decorrelation period (1-10 msec) and is fully decorrelated from pulse to pulse over frequency agility. In contrast, temporal decorrelation period of the average value is long and does not change with frequency agility. Consequently, the temporal autocorrelation function of the sea clutter has a fast drop-off, which is followed by a slower periodic decay.

If the observation and processing intervals of sea clutter signals reflected from the individual resolution cell are much shorter than the average decorrelation time of the modulating process (usually the case for numerous operational radar systems), then according to the composite scattering model the return strength of these signals is proportional to the sea clutter radar cross-section per unit area, but is essentially constant during the time a single resolution cell is illuminated. Thus, the modulating

process exhibits negligible temporal fluctuations within the radar coherent processing interval or dwell. In this case, the overall correlation properties of the returned signals are dictated by those of the rapidly varying component of the sea clutter.

3.1.2 Rain Clutter Model

We introduce rain clutter model before analyzing the effects of rain clutter on the performance of KT in the following sections. Except for weather radars, the backscatter from precipitation is not desired and interferes with the radar's operation. It is necessary to develop statistical rain clutter models depending on radar and scenario parameters before developing suppression strategies. We need to characterize amplitude and spectral characteristics of rain clutter returns. Furthermore, the attenuation of the radar signal can be considerable for frequencies significantly above 9 GHz [40].

Rain Clutter Attenuation

Rain clutter attenuation [40] depends on altitude, radar frequency and humidity. Two-way rain clutter attenuation can be approximated as

$$\alpha = 3.7 \times 10^{-4} f^{1.85} \quad \text{(dB/km)/(mm/h)} \tag{3.2}$$

where f is carrier frequency in GHz.

Amplitude Characteristics of Rain Clutter [41]

Backscattering from precipitation particles results from many small rain drops, no one of which is dominant. The amplitude is Rayleigh distributed.

The mean volume reflectivity of rain can be expressed as

$$\eta = \frac{\pi^5 |K|^2 Z}{\lambda^4} \text{ m}^{-1} \tag{3.3}$$

where λ is the carrier wavelength, K is fairly constant 0.9 for rain. The term Z - called the volume reflectivitiy - includes the wavelength dependency and is expressed in mm^6/m^3. It is shown in the form

$$Z = ar^b \tag{3.4}$$

where r is rainfall rate in mm/h. The most commonly accepted relationship is $Z = 200r^{1.6}$. Table 3.1, derived from both theoretical and experimental data, gives relation of reflectivity with frequency and precipitation type [41].

Table 3.1 Rain clutter reflectivity

		η, dB m^{-1} Transmit frequency, GHz						
Z, dBz	Radar band: Type	S 3.0	C 5.6	X 9.3	K_u 15.0	K_a 35	W 95	mm 140
−12	Heavy stratus clouds				−100	−85	−69	−62
14	Drizzle, 0.25 mm/h	−102	−91	−81	−71	−58	−45*	−50*
23	Light rain, 1 mm/h	−92	−81.5	−72	−62	−49	−43*	−39*
32	Moderate rain, 4 mm/h	−83	−72	−62	−53	−41	−38*	−38*
41	Heavy rain, 16 mm/h	−73	−62	−53	−45	−33	−35*	−37*

* Approximate

Signal to clutter ratio (SCR) of rain clutter is given as [42]

$$SCR = \frac{\sigma}{R^2 \eta \Delta R \theta \varphi} \tag{3.5}$$

where σ is target RCS, R is the radial range between radar and scatterer, ΔR is range resolution, θ is half power antenna azimuth beamwidth in radians, φ is half power antenna elevation beamwidth in radians.

Spectral Characteristics of Rain Clutter

The returns from rain clutter is often considered to have a Gaussian power spectral density. It can be characterized by standard deviation σ_v and mean velocity v_0 in m/s. Nathanson and Reilly [41] have shown that Doppler spectra of rain clutter is determined by four mechanisms:

• Wind shear: change in wind velocity in various altitudes.

$$\sigma_{shear} = 0.42kR\varphi \tag{3.6}$$

where k is the velocity gradient in the vertical direction of the beam in m/s/km, R is the slant range to clutter in km and φ is the two-way half power antenna elevation beamwidth in radians. For pencil beam radars, $k = 4$ m/s/km is suggested for an arbitrary radar azimuth.

• Turbulences: unpredictable sudden change in wind.

It is not dependent on height and up to 1.5 km altitude, σ_{turb} is approximately equal to 1 m/s as found in many experiments.

• Fall velocity distribution

$\sigma_{fall} = 1.0 \sin\psi$ where ψ is the elevation angle.

• Beam broadening

$\sigma_{beam} = 0.42 v_0 \theta \sin\beta$ where v_0 is the wind speed in the beam center in m/s, θ is the half power antenna azimuth beam width in radians and β is the azimuth angle relative to the wind direction at beam center in radians.

If we assume these mechanisms are independent, the variance of Doppler velocity spectrum as sum of variances comes from each mechanism.

$$\sigma_v{}^2 = \sigma_{shear}{}^2 + \sigma_{beam}{}^2 + \sigma_{turb}{}^2 + \sigma_{fall}{}^2 \tag{3.7}$$

The mean velocity of the rain clutter can be represented as follows [1]:

$$v_0 = v_p \cos(A_p - A_b) - v_w \cos(A_w - A_b) + v_z \sin\psi \tag{3.8}$$

where A_p is the azimuth and v_p is the magnitude of the radar platform velocity, A_w is the azimuth and v_w is the magnitude of the wind velocity, A_b is the azimuth of the beam axis, v_z is the rain fall velocity.

3.1.2.1 Rain Clutter Simulation

We can generate rain clutter samples assuming amplitude of the rain clutter is Rayleigh distributed and has a Gaussian-shaped Doppler spectra. SIRP [43] is a well known approach for modeling non-Gaussian random variables. In order to generate correlated Rayleigh distributed random vector **y** with a desired covariance matrix **C**,

i. We first generate uncorrelated zero-mean unity variance Gaussian random vectors $\mathbf{x_1}$ and $\mathbf{x_2}$.

ii. Then we obtain desired real and complex components of random vector **y** using linear transformation as follows

$$\mathrm{Re}\{\mathbf{y}\} = \mathbf{G}\mathbf{x_1},\ \mathrm{Im}\{\mathbf{y}\} = \mathbf{G}\mathbf{x_2} \tag{3.9}$$

where $\mathbf{G} = \mathbf{E}\boldsymbol{D}^{\mathbf{1/2}}$.

E is the matrix of normalized eigenvectors of the covariance matrix **C**, and **D** is the diagonal matrix of eigenvalues of **C**.

A Gaussian-shaped clutter spectrum with unity power can be represented as given

$$S(f) = \frac{1}{\sqrt{2\pi}\sigma_f} e^{-\frac{f^2}{2\sigma_f{}^2}} \tag{3.10}$$

The velocity standard deviation has been converted to standard deviation of clutter power spectrum in Hz using the Doppler relation:

$$\sigma_f = \frac{2\sigma_v}{\lambda} \tag{3.11}$$

The corresponding auto-correlation function is

$$R(\tau) = e^{-4\pi\sigma_f^2\tau^2} \tag{3.12}$$

Hence the covariance matrix can be represented as

$$\boldsymbol{C} = \begin{bmatrix} 1 & R(T_r) & . & \ldots & R((N-1)T_r) \\ R(T_r) & 1 & . & \ldots & R((N-2)T_r) \\ . & . & . & \ldots & . \\ . & . & . & \ldots & . \\ R((N-1)T_r) & R((N-2)T_r) & . & \ldots & 1 \end{bmatrix} \tag{3.13}$$

where T_r is the pulse repetition interval.

3.1.3 Clutter Suppression

We review clutter suppression methods such as optimal MTI filters and PD processing, clutter suppression performance metrics, and provide simulation results of some examples.

3.1.3.1 Optimum MTI Filter [42]

Consider a complex signal column vector $\mathbf{y}_m = \left[y[m]\ y[m-1] \ldots y[m-N+1]\right]^T$ and a filter weight vector $\mathbf{h} = [h[0] \ldots h[N-1]]^T$, where $[\cdot]^T$ denotes matrix transpose. For simplicity $\mathbf{y}_m$ will be written as simply $\mathbf{y}$. A single output sample z

of the filter is represented by $z = \mathbf{h}^T\mathbf{y}$. The target signal vector is shown by **t** and the interference vector by **w**, so that $\mathbf{y} = \mathbf{t} + \mathbf{w}$**.** Denote the expected value of $\mathbf{w}^*\boldsymbol{w}^{\boldsymbol{T}}$ as the interference covariance matrix $\mathbf{S_I}$**.**

When the covariance matrix of the interference $\mathbf{S_I}$ is known, coefficients of the optimum clutter suppression filter are given by the equation

$$\mathbf{h} = \begin{bmatrix} h[0] \\ \vdots \\ h[N-1] \end{bmatrix} = \mathbf{S_I}^{-1}\mathbf{t}^* \tag{3.14}$$

Target signal can be represented as follows if the target moves with a constant radial velocity

$$\mathbf{t} = \left[1\ e^{-j2\pi f_D T} \dots e^{-j2\pi f_D (N-1)T}\right]^{\boldsymbol{T}} \tag{3.15}$$

where f_D is Doppler frequency.

The filtered data can be shown as

$$z = \mathbf{h}^T\mathbf{y} = \mathbf{t}^H(\mathbf{S_I}^{-1})^*\mathbf{y} \tag{3.16}$$

where $[\cdot]^H$ denotes Hermitian transpose.

Thus, the fast time/slow time data sequence is high-pass filtered in the slow-time, producing another fast time/slow time data matrix where the clutter components are attenuated.

3.1.3.2 Pulse Doppler (PD) Processing

PD processing differs from optimum MTI filtering in that high-pass filtering in the slow-time domain is replaced by explicit spectral analysis of slow-time data for each range bin. Thus, the result is a data matrix whose dimensions are fast time and Doppler frequency.

The aim is to pass the data through a bank of filters, each of them tuned to a different Doppler frequency. The filtered data can be presented to optimum MTI filter as follows

$$z = \mathbf{t}^H (\mathbf{S_I}^{-1})^* \mathbf{y} = \mathbf{t}^H \mathbf{y}_w \tag{3.17}$$

where $\mathbf{y}_w = (\mathbf{S_I}^{-1})^* \mathbf{y} = \left[y_w[0] \ \ldots y_w[N-1] \right]^{\boldsymbol{T}}$ shows whitened data.

$$z = \sum_{k=0}^{N-1} y_w[k] e^{j2\pi k f_D T} \tag{3.18}$$

We can perform the same operation using *N*-point DFT assuming $f_D = -\frac{n}{NT}$:

$$z[n] = \sum_{k=0}^{N-1} y_w[k] e^{-j2\pi kn/N} \tag{3.19}$$

$$\mathbf{z} = DFT(\mathbf{y}_w) = \left[z[0] \ \ldots z[N-1] \right]^{\boldsymbol{T}} \tag{3.20}$$

$$\mathbf{z} = DFT\left((\mathbf{S_I}^{-1})^* \mathbf{y} \right) \tag{3.21}$$

Thus, the n^{th} DFT sample corresponds to a Doppler filter bank output assuming Doppler frequency $f_D = -\frac{n}{NT}$, i.e. the Doppler frequency coincides exactly with one of the DFT sample frequencies. Because the *N*-point DFT calculates *N* different outputs from each input vector, actually it applies a bank of *N* matched filters simultaneously, each of them tuned to a different Doppler frequency. The peak value of the DFT amplitude is highest when Doppler frequency is exactly $f_D = -\frac{n}{NT}$, and decreases when target Doppler frequency is between DFT sample frequencies. This amplitude decrease is defined as Doppler straddle loss.

Doppler spectrum of a moving target has side-lobes in addition to the main-lobe which is centered at f_D. In order to reduce amplitude of these side-lobes, windowing can be applied before taking DFT [42]. Then (3.19) becomes as follows

$$z[n] = \sum_{k=0}^{N-1} w[k] y_w[k] e^{-j2\pi kn/N} \tag{3.22}$$

where $w[k]$ represents coefficients of selected windowing filter.

3.1.3.3 Clutter Suppression Performance Analysis

Some useful figure of merits necessary to analyze clutter suppression performance are defined in [42]. The first criterion is *clutter attenuation* (CA). It is simply as follows

$$CA = \frac{clutter\ power\ at\ the\ filter\ input}{clutter\ power\ at\ the\ filter\ output} = \frac{P_{C_{in}}}{P_{C_{out}}} \tag{3.23}$$

Clutter power at the filter output can be calculated analytically

$$P_{C_{out}} = h^H S_I^{-1} h \tag{3.24}$$

where *h* is the vector of coefficients of the MTI filter.

Another measure of the MTI filter performance is the *improvement factor* (IF), which can be defined as ratio of (signal to clutter ratio) SCR at the filter output to the SCR at the filter input.

$$IF = \frac{SCR_{out}}{SCR_{in}} = \frac{P_{S_{out}}}{P_{S_{in}}} \frac{P_{C_{in}}}{P_{C_{out}}} = G \cdot CA \tag{3.25}$$

where $G = \frac{P_{S_{out}}}{P_{S_{in}}}$ is power gain of the filter. The numerator of *G* (the signal power at the filter output) can be expressed as

$$P_{S_{out}} = h^H \mathbf{t}^* \mathbf{t} h \tag{3.26}$$

where **t** is the desired target signal vector.

Minimum detectable Doppler (MDD) or *minimum detectable velocity* (MDV) is another metric. Let's define *SCR loss* as reduction in SCR relative to no clutter case - the maximum SCR possible, and "acceptable" value of SCR loss L_0 (typical value -3dB). MDD and usable Doppler space fraction (UDSF) are illustrated in Figure 3.1. MDD is the Doppler shift above which the SCR loss is greater than L_0 [44].

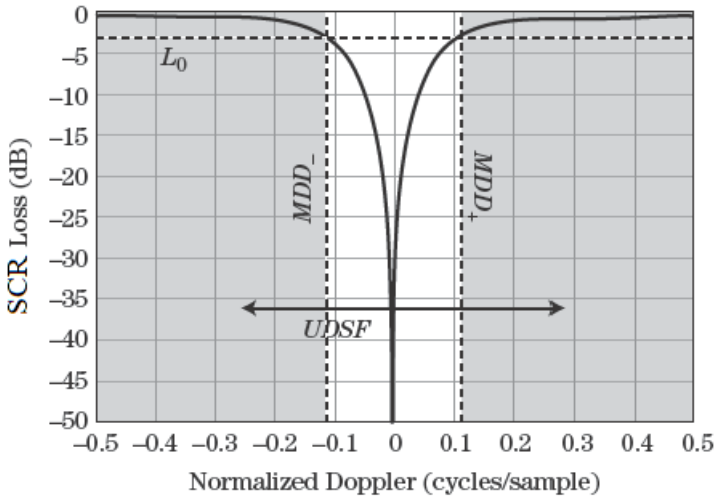

Figure 3.1. Illustration of minimum detectable Doppler

3.1.3.4 Simulation Results

Numerical simulations have been performed to show examples for rain clutter modeling and clutter suppression. We compared IF for optimum MTI and PD processing methods at various scenarios. Radar simulation parameters are listed in Table 3.2 and the rain clutter simulation parameters referring to section 3.1.2 are listed in Table 3.3.

Table 3.2 Radar simulation parameters

Target fluctuation	Swerling-0
Pulse width	30μs
Bandwidth	20MHz
Number of pulses, *N*	64
PRI	75μs
Carrier frequency	9GHz

Table 3.3 Rain clutter simulation parameters

Parameter	**Value**	**Explanation**
R	15000	the slant range to clutter in m
ΔR	7.5	Range resolution, m
η	-62dB	Volume reflectivity of rain for 9.3GHz, m^{-1}
φ_2	2.8	the two-way half power antenna elevation beamwidth in degree
k	4	the velocity gradient in the vertical direction of the beam in m/s/km
V_0	10	the wind speed in the beam center in m/s
θ_2	2.8	the two-way half power antenna azimuth beam width in degree
β	45	the azimuth angle relative to the wind direction at beam center in degree
ψ	10	the elevation angle in degree
σ_{turb}	1	m/s
σ_{shear}	0.82	m/s
σ_{beam}	0.16	m/s
σ_{fall}	0.17	m/s

σ_v	1.31	Standard deviation of Doppler velocity spectrum m/s
σ_f	78.6	Standard deviation of Doppler frequency spectrum Hz
V	3.3e4	Volume resolution cell
SCR	-1.92dB	Signal to clutter ratio (before considering attenuation)
v_z	5	Rain fall velocity, m/s
v_w	8 : upper limit Beaufort-4	Wind speed, m/s
v_p	0	Radar platform velocity, m/s
$A_w - A_b$	45	Azimuth angle between beam axis and wind, degrees
v_0	6.5	Mean clutter velocity, m/s

Figure 3.2 shows improvement factor obtained analytically and by simulations for optimum MTI and PD processing clutter suppression methods when mean clutter velocity is V_0=6.5 m/s and standard deviation of Doppler velocity spectrum is σ_v=1.31 m/s.

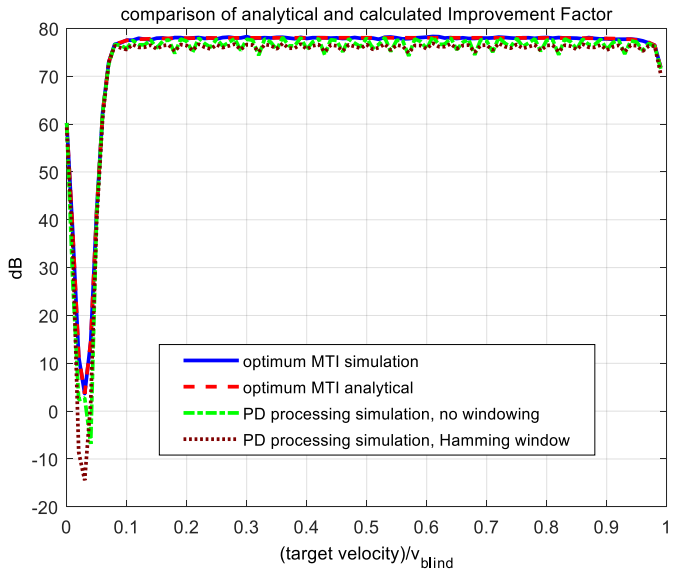

Figure 3.2. Improvement factor comparison for V_0=6.5 m/s and σ_v=1.31 m/s

In Figure 3.2, it is observed that IF obtained by analytical calculation and simulation results coincide after suppressing the clutter using an optimum MTI filter. Optimum MTI filter results in slightly higher IF compared to PD processing.

Figure 3.3 and Figure 3.4 shows improvement factor for various standard deviation of Doppler velocity σ_v=3.93 m/s and σ_v=0.1 m/s, respectively. Comparing Figure 3.2, Figure 3.3 and Figure 3.4, one can conclude that lower MDV can be obtained for lower values of σ_v. On the other hand, maximum IF does not change significantly depending on σ_v.

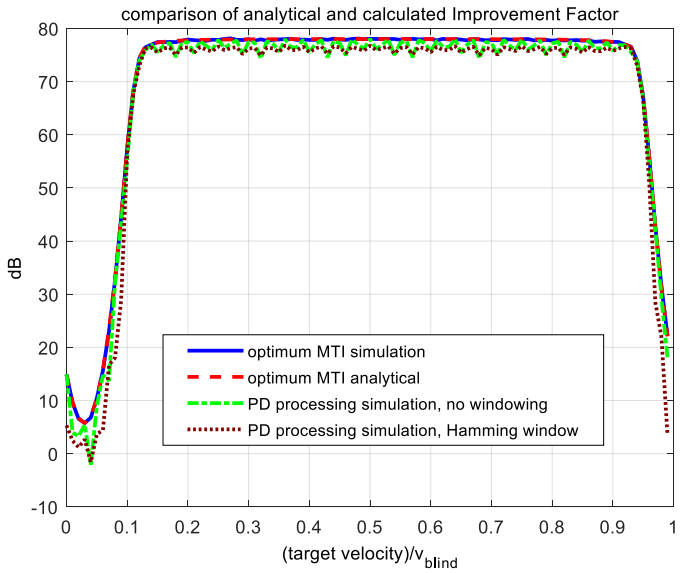

Figure 3.3. Improvement factor comparison for V_0=6.5 m/s and σ_v=3.93 m/s

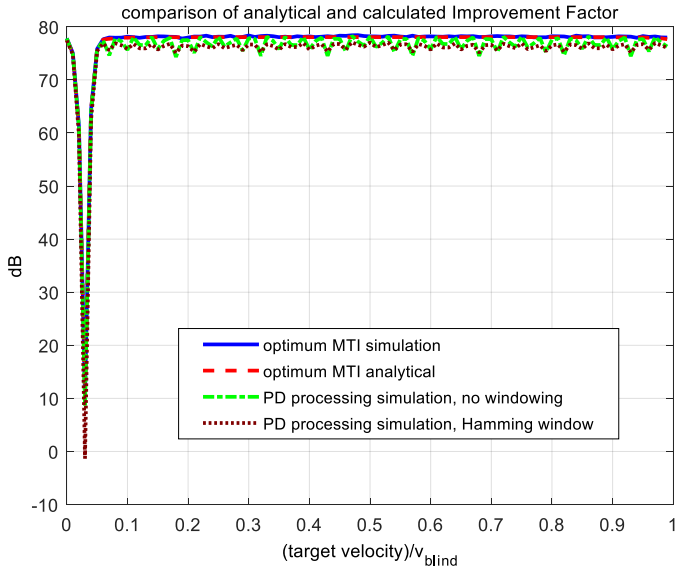

Figure 3.4. Improvement factor comparison for V_0=6.5 m/s and σ_v=0.1 m/s

Figure 3.5 shows the improvement factor when the clutter suppression filter assumes V_0=0 m/s while true mean clutter velocity is V_0=6.5 m/s. It is obvious that there is a performance degradation if the correct mean clutter velocity is not known.

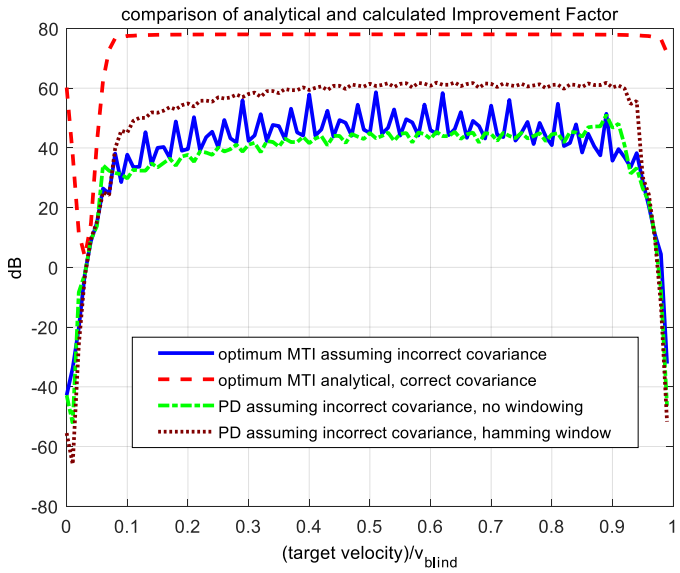

Figure 3.5. Improvement factor comparison for V_0=6.5 m/s and σ_v=0.1 m/s when clutter suppression filter assumes V_0=0 m/s

We have also investigated how the clutter suppression performance changes when correct standard deviation of Doppler velocity spectrum is not known for different target velocities. Figure 3.6 and Figure 3.7 present improvement factor versus ratio of assumed σ_v to true σ_v for MTI filtering and PD processing respectively. The figures show that we obtain higher MDV if we assume higher values of σ_v when we do not know exact value of σ_v. Hence, we can suggest to apply slightly higher values of σ_v in the clutter suppression filter when exact value of Doppler spread is not known.

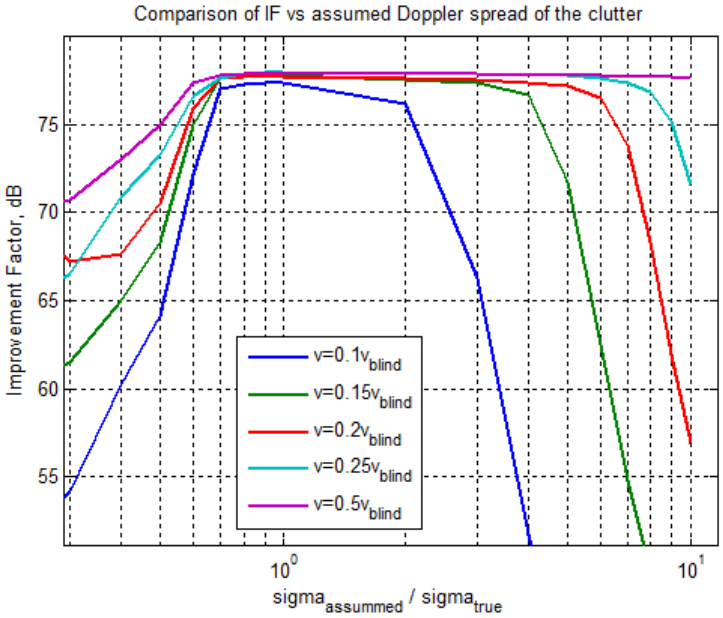

Figure 3.6. MTI filter - comparison of IF vs assumed Doppler spread of the clutter

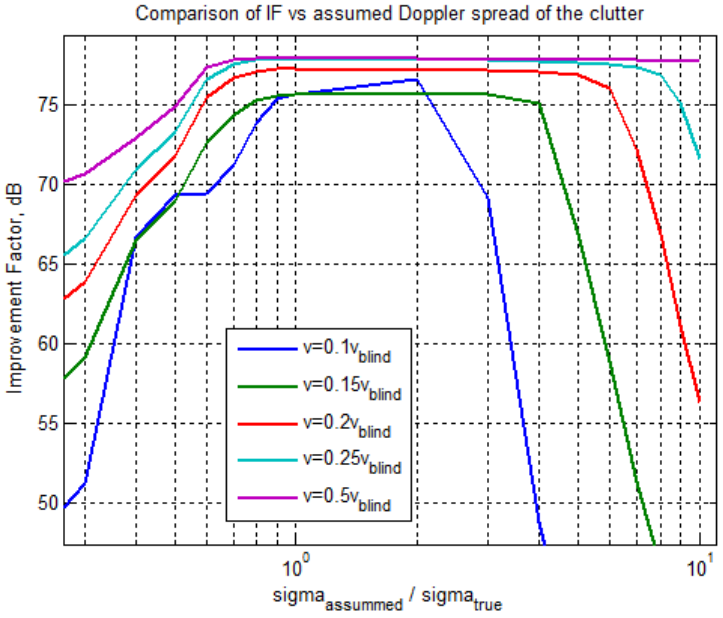

Figure 3.7. PD processing - comparison of IF vs assumed Doppler spread of the clutter

3.2 Target Fluctuation Model

In chapter 2, we supposed that the echo of an individual target did not change with time. However, we usually do not expect the amplitude of the received signal from a moving target to be constant [2]. A reasonable way of evaluating the impact of a fluctuating cross section is to suppose an acceptable model and to examine it analytically. In this section, we examine the target fluctuation models.

3.2.1 Swerling Target Models

The Swerling models are based on the probability density function (pdf) and time correlation characteristics of the received signals from a target [42]. The Swerling models are relevant to a finite set of pulses. A rotating surveillance radar was considered in the development of the Swerling models. When the radar beam scans through a target (a single *scan*), it accumulates returns from that target in the proper range resolution cell for multiple pulses. If the beam passes through the target, no more returns are received until the next scan. As the beam returns to the target position; then another set of multiple pulses is received. It is supposed that all of the pulses from a single scan are used for detection. Therefore, we are interested in the joint statistics of a set of target echo samples from contiguous pulses of a single scan.

The Swerling models are composed of the four combinations of 2 probability density functions (pdf's) for the individual echo powers and 2 presumptions concerning the correlation of pulses during a single sweep, as given in the following table:

Table 3.4 Swerling Target Models

probability density function of power	**decorrelation**	
	scan-to-scan	pulse-to-pulse
exponential	1	2
chi-square, degree 4	3	4

We assume the pdf of the particular echo powers are either exponential (Swerling 1 and 2) or fourth-degree chi-square (Swerling 3 and 4). The voltage distributions are the Rayleigh and the fourth-degree chi distributions. Regarding the correlation, the "scan-to-scan decorrelation" means that all the echoes have the same value during a particular scan, drawn from the same pdf. All of the pulses in the next scan are again same as one another, but not same as pulses in the previous scan. Rather, their value is new, drawn independently from the same pdf.

3.2.2 Moderately Fluctuating Targets

There are two main situations that are used in the literature to detect the pulse train reflected from a fluctuating target [41]: (i) fast fluctuation where the fluctuation correlation time is shorter than PRI (uncorrelated), (ii) slow fluctuation where the correlation time is longer than CPI (fully correlated).). For the target amplitude with Rayleigh distribution, the slow fluctuation corresponds to the Swerling-1 model, and the fast fluctuation corresponds to the Swerling-2 model. In practice, medium-speed fluctuating (partially correlated) targets occur, indicating the situations between these two extremes, that is, the correlation time of the fluctuation is short compared to the total observation time, but longer than the time between pulses [45] ($0 < \rho < 1$).

According to Table 3.4, Swerling-1 target fluctuation model has the assumption of scan-to-scan decorrelation. The "scan-to-scan decorrelation" means that all the

echoes have the same value during a particular scan, drawn from the same pdf. All of the pulses in the next scan are again same as one another, but not same as pulses in the previous scan. Rather, their value is new, drawn independently from the same pdf. However, it is not be the case in moderately fluctuating targets. We can assume that amplitude of target echo is decorrelated throughout a scan continuously. That is, amplitude is not fully correlated during a scan.

Hence, we can model target echo amplitude of moderately fluctuating target as correlated Rayleigh random variables.

Suppose that $\boldsymbol{N}$ represents number of samples in the signal amplitude fluctuation process, and N_j, the j^{th} element of $\boldsymbol{N}$, satisfies the recursion

$$N_j = \rho N_{j-1} + \sqrt{1-\rho^2}U_j,\ j = 2,3,\ldots$$

or equivalently in terms of N_{j-k} (k elements before j^{th} element of $\boldsymbol{N}$)

$$N_j = \rho^k N_{j-k} + \sum_{i=0}^{k-1} \rho^i \sqrt{1-\rho^2}U_{j-i} \tag{3.27}$$

with ρ real, $|\rho| < 1$, where U_j sequence consists of mean-zero independent complex Gaussian random variables with

$$E\{U_j^2\} = 0;\ E\left\{\left|U_j\right|^2\right\} = 1 \tag{3.28}$$

We can verify it simply if such a recursion begins with a zero-mean complex Gaussian random variable N_1 having

$$E\{N_1^2\} = 0;\ E\{|N_1|^2\} = 1 \tag{3.29}$$

Therefore, the covariance matrix C_N of $\boldsymbol{N}$ is represented by

$$C_N = \begin{bmatrix} 1 & \rho & \rho^2 & \dots & \rho^{N-1} \\ \rho & 1 & \rho & \dots & \rho^{N-2} \\ \rho^2 & \rho & 1 & \dots & \rho^{N-3} \\ . & . & . & \dots & . \\ \rho^{N-1} & \rho^{N-2} & \rho^{N-3} & \dots & 1 \end{bmatrix} \tag{3.30}$$

3.3 Detection of Moderately Fluctuating Targets by Hybrid Integration

In this section, we present a hybrid integration method to detect moderately fluctuating targets. Firstly, we describe the hybrid integration procedure. Secondly, we derive the expressions of detection and false alarm probability in hybrid integration for four different fluctuation types. Finally, we show simulation results after applying hybrid integration method for both static and range-migrating targets.

3.3.1 Procedure to perform Hybrid Integration

Integrating signals received from nonfluctuating or slowly-fluctuating targets coherently gives better P_d vs SNR performance, while noncoherent integration gives better performance for pulse-to-pulse fluctuations [46]. We can integrate the signals received from a fluctuating target in a more efficient manner,

i) divide the observation time into blocks where fluctuation is assumed not decorrelated,
ii) integrate the signals coherently in each block,
iii) integrate the resultant integrals noncoherently.

We want to examine the performance for this kind of hybrid integration. Hybrid integration scheme is given in Figure 3.8. Observation time is divided into *K* blocks, each block is a pulse train having *N* pulses. Each block is integrated coherently by collecting *N* pulses to obtain y_k's. Then resultant integration output *z* is obtained by integrating y_k's noncoherently.

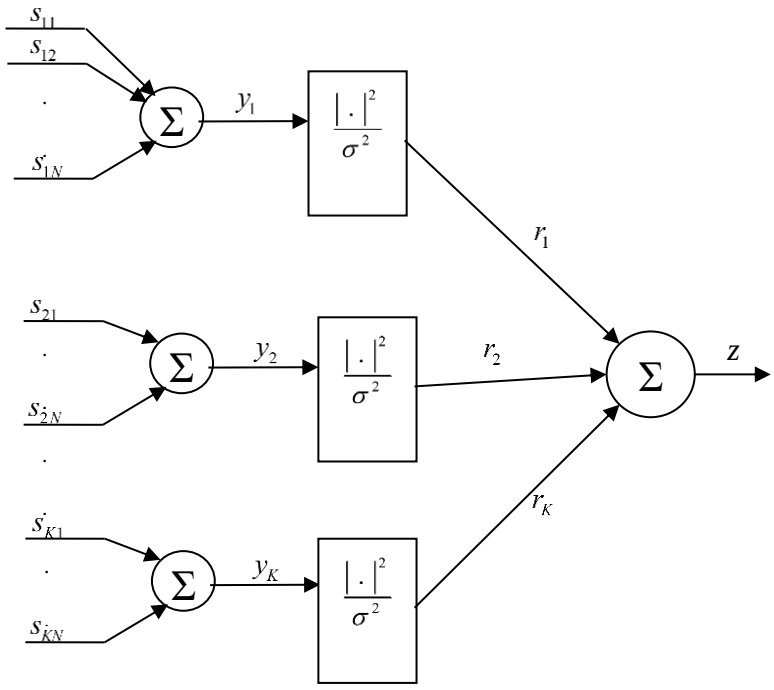

Figure 3.8 Hybrid integration scheme

3.3.2 False Alarm and Detection Probability

We derive the P_D and P_F expressions for four different cases when hybrid integration is performed:

1. Nonfluctuating target
2. Fully correlated Swerling-1 target

3. Statistically independent fully correlated Swerling-1 target in each block
4. Statistically independent partially correlated Swerling-1 target in each block

In cases 3 and 4, K' coherent pulse trains each consisting of N' pulses are transmitted for a total of $K'N'$ pulses. Each of the K' pulse trains is transmitted at a different frequency, spaced sufficiently far apart that the target fluctuation processes at the different frequencies can be assumed to be statistically independent. Analytical expressions of P_D and P_F will be given for the case $N=N'$ and $K=K'$. K' and N' values will be swept in the simulations.

We assume detection will be based on KN samples of data s_{kn} during a CPI, where s_{kn} is the signal received from a point-target.

H_1: $s_{kn} = a_{kn} + w_{kn}$

H_0: $s_{kn} = w_{kn}$

where a_{kn} is echo amplitude of target, and w_{kn} is complex Gaussian noise, in-phase and quadrature channels each contain i.i.d. $\sim N(0, \frac{\sigma^2}{2})$.

3.3.2.1 Case I - Nonfluctuating Target

For nonfluctuating target model, echo amplitude of target is deterministic,

$$a_{kn} = A \quad \forall k, n \tag{3.31}$$

$$SNR = \frac{|A|^2}{\sigma^2} \tag{3.32}$$

Coherent integration

N pulses are integrated coherently in each of K blocks.

$$y_k = \sum_{n=1}^{N} s_{kn} \tag{3.33}$$

$$\begin{aligned} &\text{H}_0: \quad y_k = \textstyle\sum_{n=1}^{N} w_{kn} \qquad\quad \sim NC(0, N\sigma^2) \\ &\text{H}_1: \quad y_k = NA + \textstyle\sum_{n=1}^{N} w_{kn} \sim NC(NA, N\sigma^2) \end{aligned} \tag{3.34}$$

SNR value for y_k can be given as

$$SNR_{coh} = N \cdot SNR \tag{3.35}$$

Noncoherent integration [42]

After normalizing the coherent integration outputs of each block, and performing square-low noncoherent integration, hybrid integration output *z* is obtained.

$$r_k = \frac{|y_k|^2}{\sigma^2} \tag{3.36}$$

Under hypothesis H_0, the pdf of r_k is exponential :

$$p_{r_k}(r_k|H_0) = \begin{cases} e^{-r_k} & r_k \geq 0 \\ 0 & r_k < 0 \end{cases} \tag{3.37}$$

Under hypothesis H_1, the pdf of r_k is Rician :

$$p_{r_k}(r_k|H_1) = \begin{cases} e^{-(r_k + SNR_{coh})} I_0(2\sqrt{SNR_{coh} r_k}) & r_k \geq 0 \\ 0 & r_k < 0 \end{cases} \tag{3.38}$$

where $I_0(.)$ is the modified Bessel function of the first kind.

$$z = \sum_{k=1}^{K} r_k \underset{H_0}{\overset{H_1}{\gtrless}} T \tag{3.39}$$

Since *z* is the sum of *K* scaled random variables, the pdf of *z* is the *K*-fold convolution of the pdf given in (3.37) and (3.38). This can be found using characteristic functions.

Under H_0 hypothesis:

Characteristic function of r_k is given by

$$C_{r_k}(q) = \int_{-\infty}^{\infty} p_{r_k}(r_k) e^{jqr_k} dr_k = \frac{1}{1 - jq} \tag{3.40}$$

Characteristic function of *z* is

$$C_z(q) = \frac{1}{(1 - jq)^K} \tag{3.41}$$

The pdf of *z* is obtained by inverting its characteristic function using the inverse Fourier transform

$$p_z(z|H_0) = \frac{1}{2\pi} \int_{-\infty}^{\infty} C_z(q) e^{-jqz} dq \tag{3.42}$$

Then, the Erlang density is obtained

$$p_z(z|H_0) = \begin{cases} \dfrac{z^{K-1}}{(K-1)!} e^{-z} & z \geq 0 \\ 0 & z < 0 \end{cases} \tag{3.43}$$

The false alarm probability can be obtained by integrating from the threshold to infinity. The result is

$$P_{FA} = \int_{T}^{\infty} p_z(z|H_0)dz = 1 - I\left(\frac{T}{\sqrt{K}}, K-1\right) \tag{3.44}$$

where $I(u,M) = \int_0^{u\sqrt{M+1}} \frac{e^{-\tau}\tau^M}{M!} d\tau$.

Now we determine the probability of detection P_D.

Under H_1 hypothesis:

Each individual data sample r_k is Rician; the corresponding characteristic function is

$$C_{r_k}(q) = \frac{1}{q+1} e^{-\left(\frac{q}{q+1}\right)SNR_{coh}} \tag{3.45}$$

and the characteristic function of the sum of *K* samples is

$$C_z(q) = \frac{1}{(q+1)^K} e^{-K\left(\frac{q}{q+1}\right)SNR_{coh}} \tag{3.46}$$

The pdf of *z* is given by

$$p_z(z|H_1) = \left(\frac{z}{K \cdot SNR_{coh}}\right)^{(K-1)/2} e^{-z-K\cdot SNR_{coh}} I_{K-1}\left(2\sqrt{KzSNR_{coh}}\right) \tag{3.47}$$

We can find P_D by integrating (3.47)

$$P_D = \int_T^{\infty} p_z(z|H_1)dz$$
$$= Q_M\left(\sqrt{K \cdot SNR_{coh}}, \sqrt{2T}\right)$$
$$+ e^{-(T+K \cdot SNR_{coh})} \sum_{r=2}^{K} \left(\frac{T}{K \cdot SNR_{coh}}\right)^{(r-1)/2} I_{r-1}\left(2\sqrt{K \cdot SNR_{coh} T}\right) \quad (3.48)$$

where Q_M is Marcum's Q-function.

Hence, we have obtained detection and false alarm probability expressions for non-fluctuating targets as given in (3.44) and (3.48).

3.3.2.2 Case II - Fully Correlated Swerling-1 Target

The signal received from fully correlated Swerling-1 target can be expressed as follows for two hypotheses:

$$\begin{aligned} &H_0: \quad s_{kn} = w_{kn} \\ &H_1: \quad s_{kn} = a_{kn} + w_{kn} \end{aligned} \quad (3.49)$$

For Swerling-1 target, echo amplitude of target $\tilde{A}$ is a Rayleigh distributed random variable but it is a fixed value for all *KN* pulses.

$$a_{kn} = \tilde{A} \quad \forall k, n \quad (3.50)$$

$$S\tilde{N}R = \frac{\left|\tilde{A}\right|^2}{\sigma^2} \quad (3.51)$$

Coherent integration

N pulses are integrated coherently in each of *K* blocks.

$$y_k = \sum_{n=1}^{N} s_{kn} \tag{3.52}$$

$$\begin{aligned} &\text{H}_0: \quad y_k = \textstyle\sum_{n=1}^{N} w_{kn} \qquad\quad \sim NC(0, N\sigma^2) \\ &\text{H}_1: \quad y_k = N\tilde{A} + \textstyle\sum_{n=1}^{N} w_{kn} \sim NC(N\tilde{A}, N\sigma^2) \end{aligned} \tag{3.53}$$

SNR value for y_k can be given as

$$\widetilde{SNR}_{coh} = N \cdot \widetilde{SNR}_{coh} \tag{3.54}$$

Noncoherent integration [42]

After normalizing the coherent integration outputs of each block, and performing square-low noncoherent integration, hybrid integration output *z* is obtained.

$$r_k = \frac{|y_k|^2}{\sigma^2} \tag{3.55}$$

$$z = \sum_{k=1}^{K} r_k \underset{H_0}{\overset{H_1}{\gtrless}} T \tag{3.56}$$

Since P_{FA} is determined only by the pdf when there is no target, target fluctuation has no effect on P_{FA}. Namely, the false alarm probability is same as given in (3.44).

Under H_1 hypothesis:

Similar to (3.45), characteristic function of *z* is as follows

$$C_z\left(q; \widetilde{SNR}_{coh}, K\right) = \frac{1}{(q+1)^K} e^{-K\left(\frac{q}{q+1}\right)\widetilde{SNR}_{coh}} \tag{3.58}$$

Equation (3.58) is the same expression as equation (3.45) except that now C_z is written explicitly as a function of $q, \widetilde{SNR}_{coh}, K$.

After taking expected value of the characteristic function over $\widetilde{SNR}_{coh}$,

$$\bar{C}_z(q; \bar{SNR}_{coh}, K) = \int_0^\infty P_{\widetilde{SNR}_{coh}}(\widetilde{SNR}_{coh}) C_z\left(q; \widetilde{SNR}_{coh}, K\right) d\widetilde{SNR}_{coh} \tag{3.59}$$

where $P_{\widetilde{SNR}_{coh}}(\widetilde{SNR}_{coh})$ is pdf of $\widetilde{SNR}_{coh}$ and will be exponential.

$$P_{\widetilde{SNR}_{coh}}\left(\widetilde{SNR}_{coh}\right) = \frac{1}{\widetilde{SNR}_{coh}} e^{-\widetilde{SNR}_{coh}/\overline{SNR}_{coh}} \tag{3.60}$$

$\overline{SNR}_{coh}$ is the average SNR of y_k over CPI.

$$\bar{C}_z(q; \overline{SNR}_{coh}, K) = \frac{1}{(q+1)^{K-1}(1 + q(1 + K \cdot \overline{SNR}_{coh}))} \tag{3.61}$$

The pdf of z is given by

$$p_z(z|H_1) = \frac{1}{K\overline{SNR}_{coh}} \left(1 + \frac{1}{K\overline{SNR}_{coh}}\right)^{(K-2)} \times I\left(\frac{z}{(1 + 1/(K\overline{SNR}_{coh}))\sqrt{K-1}}, K-2\right) e^{-z/(1+K\overline{SNR}_{coh})} \tag{3.62}$$

$$P_D = 1 - I\left(\frac{T}{\sqrt{K-1}}, K-2\right) +$$

$$\left(1 + \frac{1}{K\overline{SNR}_{coh}}\right)^{K-1} e^{-T/(1+K\overline{SNR}_{coh})}$$

$$\times I\left(\frac{T}{\left(1 + \frac{1}{K\overline{SNR}_{coh}}\right)\sqrt{K-1}}, K-2\right) \quad (3.63)$$

Hence, we have found the detection and false alarm probability expressions for fully correlated Swerling-1 targets as given in (3.44) and (3.63).

3.3.2.3 Case III - Statistically independent fully correlated Swerling-1 target in each block

In this target model, echo amplitude of target is assumed to have same value within N pulses drawn from Rayleigh pdf. The next N pulses are same as one another but not to ones in previous N pulses. Rather, their value is new, drawn independently from Rayleigh pdf.

$$a_{kn} = A_k \quad \forall n \quad (3.64)$$

A_i and A_j are independent if $i \neq j$.

SNR of s_{kn} for k^{th} block of N pulses in CPI is exponentially distributed, and can be given as

$$SNR_k = \frac{|A_k|^2}{\sigma^2} \quad (3.65)$$

Coherent integration

N pulses are integrated coherently in each of K blocks.

$$y_k = \sum_{n=1}^{N} s_{kn} \tag{3.66}$$

$$\begin{aligned} &\text{H}_0: \quad y_k = \textstyle\sum_{n=1}^{N} w_{kn} \qquad\quad \sim NC(0, N\sigma^2) \\ &\text{H}_1: \quad y_k = NA_k + \textstyle\sum_{n=1}^{N} w_{kn} \sim NC(NA_k, N\sigma^2) \end{aligned} \tag{3.67}$$

SNR of y_k is $SNR_{k,coh} = N \cdot SNR_k$

Noncoherent integration

After normalizing the coherent integration outputs of each block, and performing square-low noncoherent integration, hybrid integration output *z* is obtained.

$$r_k = \frac{|y_k|^2}{\sigma^2} \tag{3.68}$$

$$z = \sum_{k=1}^{K} r_k \underset{H_0}{\overset{H_1}{\gtrless}} T \tag{3.69}$$

<u>Under H_1 hypothesis:</u>

The characteristic function of r_k is as follows

$$C_{r_k}(q; SNR_{k,coh}) = \frac{1}{q+1} e^{-\left(\frac{q}{q+1}\right) SNR_{k,coh}} \tag{3.70}$$

Averaging $C_{r_k}(q)$ over $SNR_{k,coh}$ gives us

$$\bar{C}_r(q;S\bar{N}R) = \int_0^{\infty} SNR_{k,coh}(SNR_{k,coh})C_{r_k}\left(q;SNR_{k,coh}\right)dSNR_{k,coh} \tag{3.71}$$

$$\bar{C}_r(q;S\bar{N}R) = \frac{1}{1+q(1+S\bar{N}R)} \tag{3.72}$$

Then perform *N*-fold multiplication

$$\bar{C}_z(q;S\bar{N}R) = \left(\bar{C}_r(q;S\bar{N}R)\right)^K = \frac{1}{(1+q(1+S\bar{N}R))^K} \tag{3.73}$$

Inverse transforming

$$p_z(z|H_1) = \frac{z^{K-1}e^{-\frac{z}{(1+S\bar{N}R)}}}{(1+S\bar{N}R)^K(K-1)!} \tag{3.74}$$

$$P_D = 1 - I\left(\frac{T}{(1+S\bar{N}R)\sqrt{K}}, K-1\right) \tag{3.75}$$

3.3.2.4 Case IV: Statistically independent partially correlated Swerling-1 target in each block

Partially correlated Swerling-1 target model implies that fluctuations have a shorter correlation time than the CPI and longer than the PRI.

Scholtz [47] evaluated the receiver performance for the block-coherent frequency-hopping transmitter approach. In this approach, the observation time is divided into *K* intervals. A coherent pulse train is transmitted coherently during each interval, but

carrier frequency is changed between intervals. Coherent integration is employed during each interval and the results are noncoherently integrated over the *K* intervals.

Echo amplitude of target for *N* pulses in the i^{th} block $\{a_{i1} \cdots a_{iN}\}$ is drawn from correlated Rayleigh pdf. In the next *N* pulses, target amplitude $\{a_{(i+1)1} \cdots a_{(i+1)N}\}$ is drawn from the same pdf independent of previous pulses.

Covariance matrix of signal amplitude fluctuation process :

$$C_a = E\{\boldsymbol{a}\boldsymbol{a}^H\} \tag{3.76}$$

where $\boldsymbol{a} = [a_{11} \cdots a_{KN}]$.

$$C_a = \begin{bmatrix} C_a^{'} & O & \ldots & O \\ O & C_a^{'} & \ldots & O \\ \ldots & & & \ldots \\ O & O & \ldots & C_a^{'} \end{bmatrix} \tag{3.77}$$

where $C_a'$and O are *N*x*N* submatrices, O includes only zeroes. The matrix C_a' represents the covariance matrix of the elements of a_{kn} $(n = 1, \ldots, N)$ which correspond to measurements for a given coherent pulse train containing N pulses. Then, the covariance matrix becomes as follows

$$C_a^{'} = \begin{bmatrix} 1 & r & r^2 & \ldots & r^{N-1} \\ r & 1 & r & \ldots & r^{N-2} \\ r^2 & r & 1 & \ldots & r^{N-3} \\ . & . & . & \ldots & . \\ r^{N-1} & r^{N-2} & r^{N-3} & \ldots & 1 \end{bmatrix} \tag{3.78}$$

Decorrelation time t_{decor} of target fluctuation can be defined as $r^{\frac{t_{decor}}{PRI}} = \frac{1}{e}$

For example,$r = 0.9$ implies $t_{decor} = 9.5PRI$.

In this analysis:

While constituting target fluctuation model, CPI is divided into K' intervals, each of which is composed of N' pulses. A coherent pulse train composed of N' pulses is transmitted coherently during each of the K' intervals, but carrier frequency is changed between intervals such that another statistically independent fluctuation process is utilized within each of the K' intervals.

In order to perform block-coherent integration, CPI is divided into K blocks, each of which is composed of N pulses. A block of N pulses is predetection integrated during each of K intervals, and the results are postdetection integrated over the K intervals.

In [47], Scholtz found analytical expression of detection probability for the case $N = N'$, $K = K'$ which is given by

$$P_D = 1 - I\left(\frac{T}{{\sigma_1}^2}, K\right) \tag{3.79}$$

where ${\sigma_1}^2$ is the conditional variance

$${\sigma_1}^2 = E\{({r_k}^2 | H_1)\} \tag{3.80}$$

3.3.3 Simulation Results

Since we are interested in moderately fluctuating targets, we performed two groups of simulations for Case III (3.3.2.3) and Case IV (3.3.2.4) in this subsection.

3.3.3.1 Simulations: Case III

Simulations are carried out in order to see if theoretical P_D values coincide with simulation results. Simulation parameters are given in Table 3.5. After applying Keystone Transform, hybrid integration has been performed. In this target model, echo amplitude of target is assumed to have same value within N pulses drawn from Rayleigh pdf. The next N pulses are same as one another but not as ones in previous N pulses. Rather, their value is new, drawn independently from Rayleigh pdf.

P_D versus $\log_2(N)$ is shown in Figure 3.9 where N' (number of pulses during which echo amplitude of target is same) is swept. SNR per pulse is adjusted such that P_D=0.9 and P_F=10^{-4} for $N = N'$. In addition, theoretical P_D value [47] for $N = N'$ is shown in the figure. It is seen that P_D values obtained in the simulation is consistent with the theoretical P_D. We also note that selecting $N = N'$ gives best achievable P_D for a given N'.

Figure 3.10 shows SNR per pulse required to obtain P_D=0.9, P_F=10^{-4} for $N = N'$. Lowest SNR per pulse can be achieved when N=8.

Table 3.5 Simulation parameters

Carrier frequency	9GHz
Bandwidth	20MHz
PRI	10μs
Number of pulses in a CPI	64
Radial velocity	0 m/s

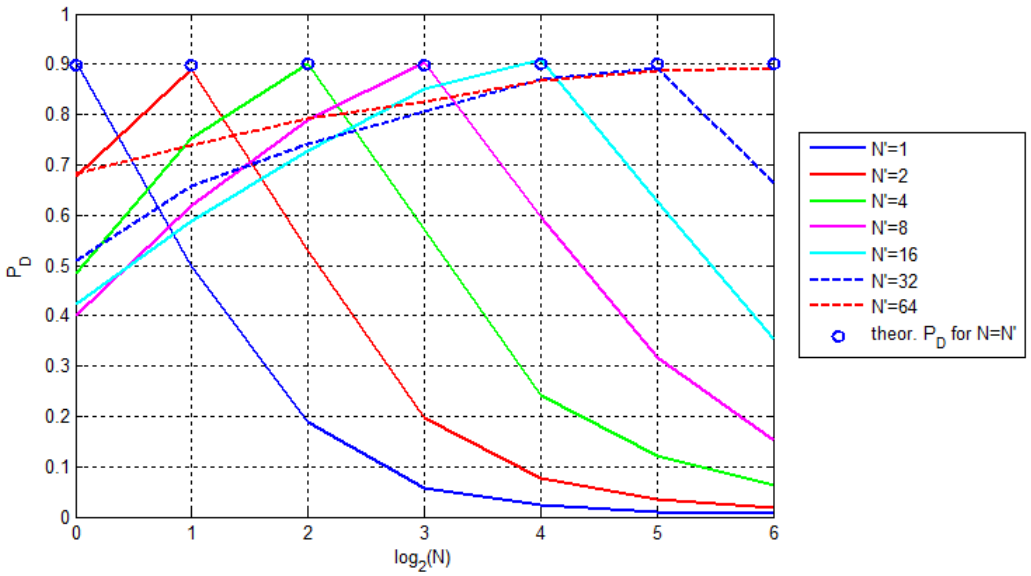

Figure 3.9. P_D versus $\log_2(N)$ when $P_F=10^{-4}$

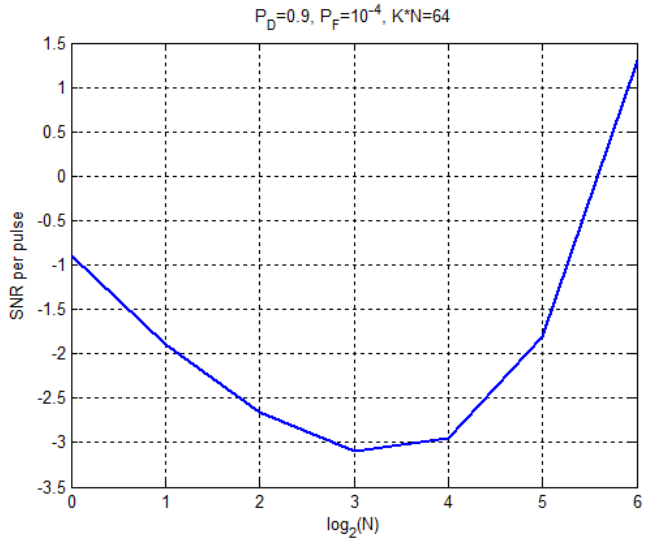

Figure 3.10. SNR per pulse required to obtain $P_D=0.9$, $P_F=10^{-4}$

3.3.3.2 Simulations: Case IV

Echo amplitude of target for N pulses in each block is drawn from correlated Rayleigh pdf. In the next N pulses, target amplitude is drawn from the same pdf independent of previous N pulses.

We explored the performance for different values of N' in the simulations. Total number of pulses in CPI is kept constant KN=64. We swept both K and K' in $\{2^0,2^1,...,2^6\}$. P_D versus $\log_2(N)$ is shown in Figure 3.11 -Figure 3.16 for different values of r and corresponding decorrelation time , which is defined as the time for r to fall to 1/e, as shown in Table 3.7 where $P_F=10^{-4}$. N'=64 corresponds to the case where carrier frequency is constant during observation time, while N'=1 corresponds to the case where each pulse has different carrier frequency. Keystone Transform has been applied before hybrid integration.

Table 3.6 Simulation parameters

Carrier frequency	9GHz
Bandwidth	20MHz
PRI	500μs
Number of pulses in a CPI	64
Radial velocity	0 m/s

Remarks regarding Figure 3.11 -Figure 3.16 are as follows:

- Theoretical P_D values given by Scholtz [47] for $N'=N$ cases are consistent with P_D values obtained in simulations.

- For a given N, maximum P_D can be achieved when $N'=N$.
- For a given N', maximum P_D may not be achieved when $N=N'$ depending on correlation coefficient r. For example, $N=1$ gives the maximum P_D for all values of N' when $r=0.3$. On the other hand, $N=N'$ gives the maximum P_D for all values of N' when $r=1$.When the correlation between pulses in each block is low enough e.g. $r=0.3$, integrating non-coherently all pulses (i.e. $N=1$) gives the best detection performance independent of N' (number of pulses transmitted with same frequency in each block). On the other hand, if the pulses in each block are fully correlated (e.g. $r=1$), we can achieve the best detection performance with coherent integration of the pulses which has the same transmission frequency in hybrid integration scheme. Hence, we expect for a given N' that $N=N'$ gives the maximum P_D only if the correlation between pulses in each block is very high.

Table 3.7 Decorrelation times for correlation coefficients

r	t_{decor} / *PRI*
0.3	0.83
0.6	1.96
0.8	4.48
0.9	9.49
0.95	14.50
1	∞

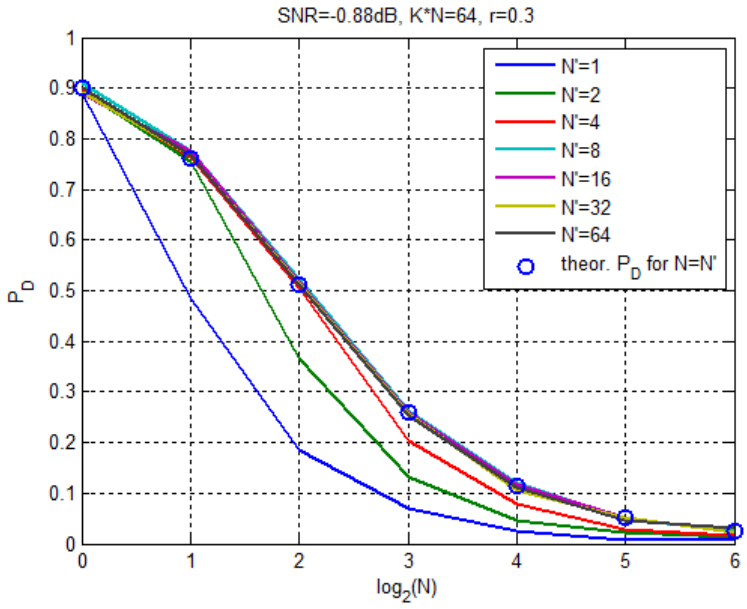

Figure 3.11. P_D versus $\log_2(N)$ for r=0.3

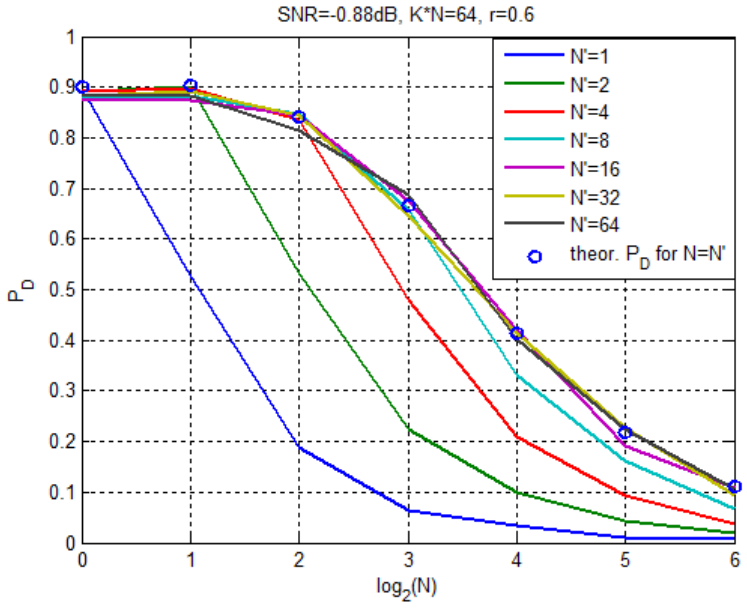

Figure 3.12. P_D versus $\log_2(N)$ for r=0.6

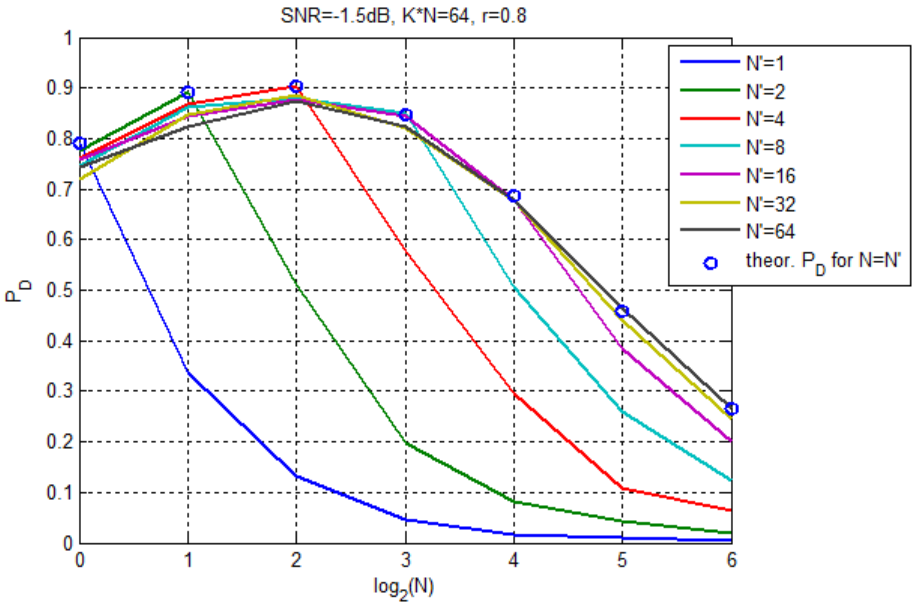

Figure 3.13. P_D versus $\log_2(N)$ for r=0.8

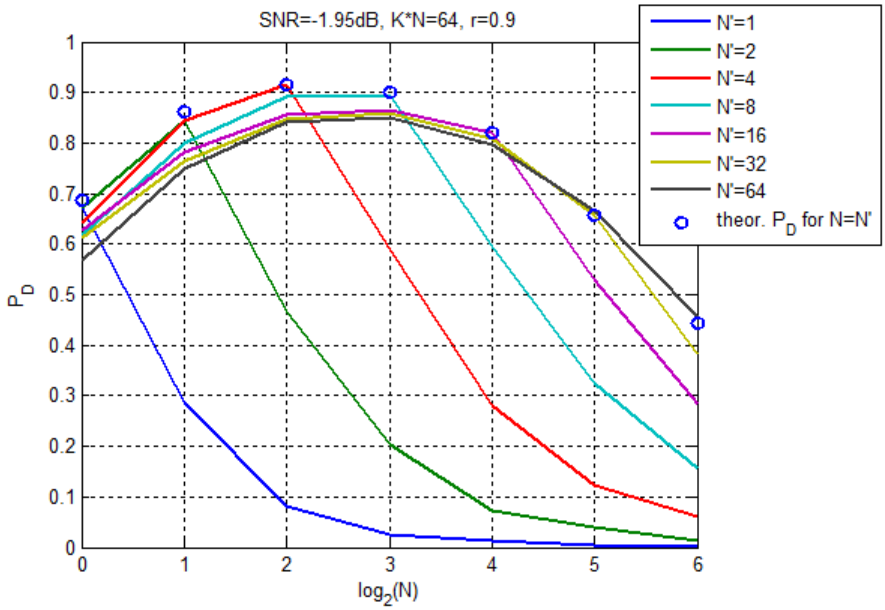

Figure 3.14. P_D versus $\log_2(N)$ for r=0.9

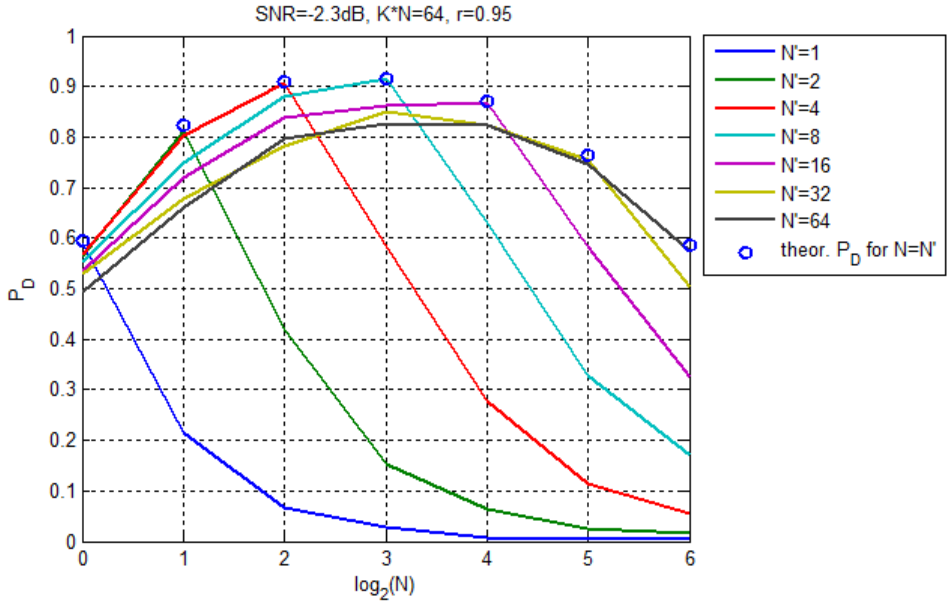

Figure 3.15. P_D versus $\log_2(N)$ for r=0.95

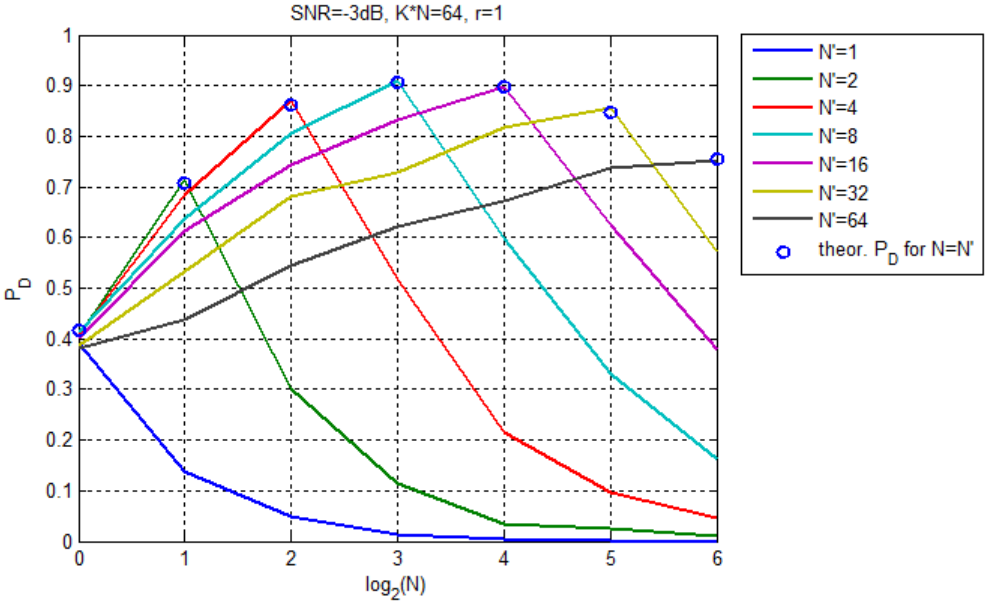

Figure 3.16. P_D versus $\log_2(N)$ for r=1

Another aim of the simulations is to examine the detection performance when there is range migration and Keystone Transform is applied to mitigate range migration

effect before integration. In the simulations, radial velocity is taken v=500m/s which causes to 2.13 range resolution cell migration. P_D versus $\log_2(N)$ is shown in Figure 3.17 - Figure 3.22 for different values of r and corresponding decorrelation time as shown in Table 3.7.

Following remarks can be noted on Figure 3.17 - Figure 3.22:

- There is a degradation on P_D compared to theoretical formula given by Scholtz [47] because KT can't eliminate the range migration perfectly due to interpolation loss.
- For a given N, maximum P_D can be achieved when $N'=N$.
- For a given N', maximum P_D may not be achieved when $N=N'$ depending on correlation coefficient r. As explained for the zero velocity case, we expect for a given N' that $N=N'$ gives the maximum P_D only if the correlation between pulses in each block is very high.

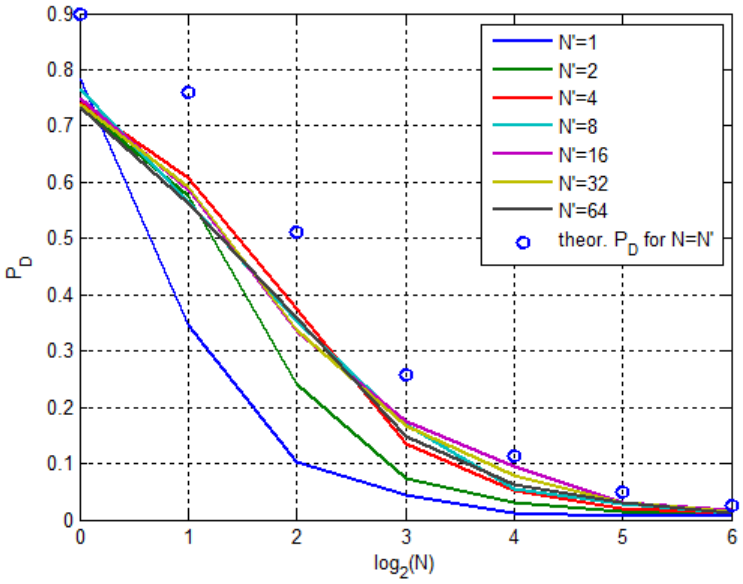

Figure 3.17. P_D versus $\log_2(N)$ for r=0.3 v=500m/s

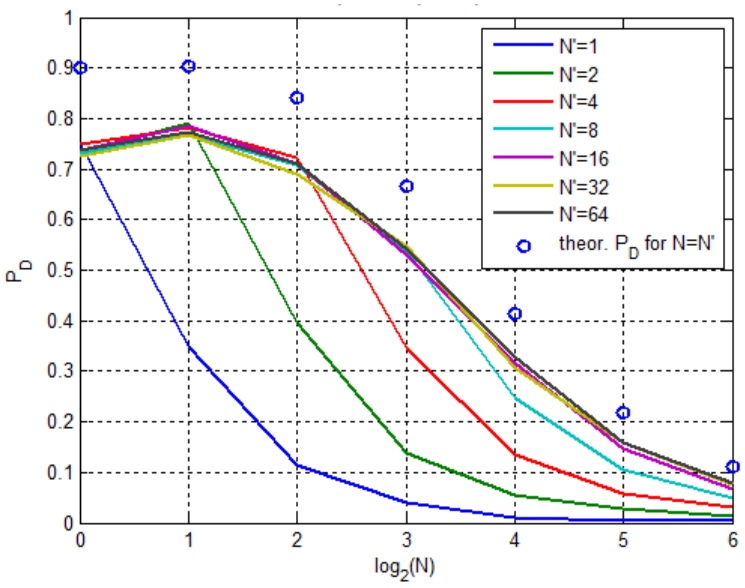

Figure 3.18. P_D versus $\log_2(N)$ for r=0.6 v=500m/s

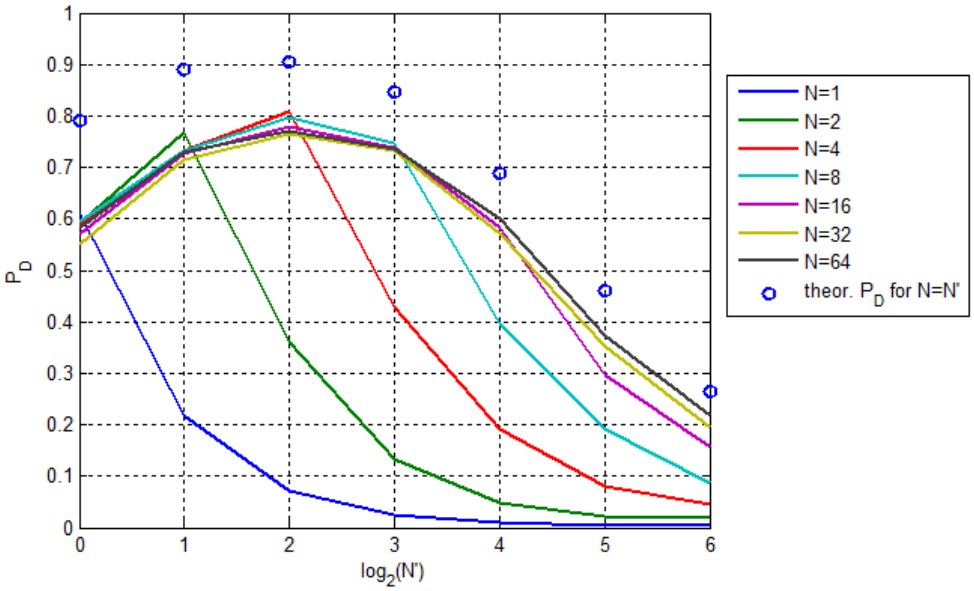

Figure 3.19. P_D versus $\log_2(N)$ for r=0.8 v=500m/s

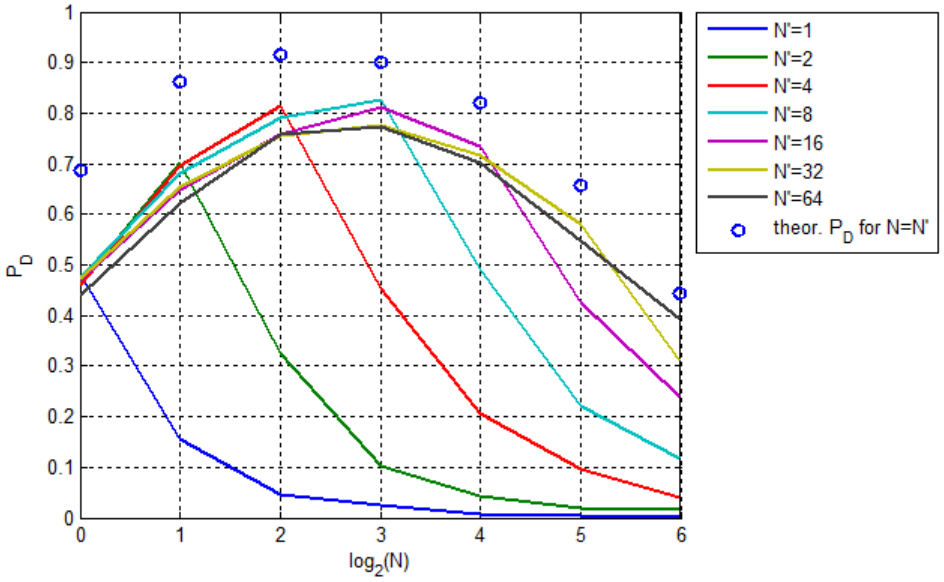

Figure 3.20. P_D versus $\log_2(N)$ for r=0.9 v=500m/s

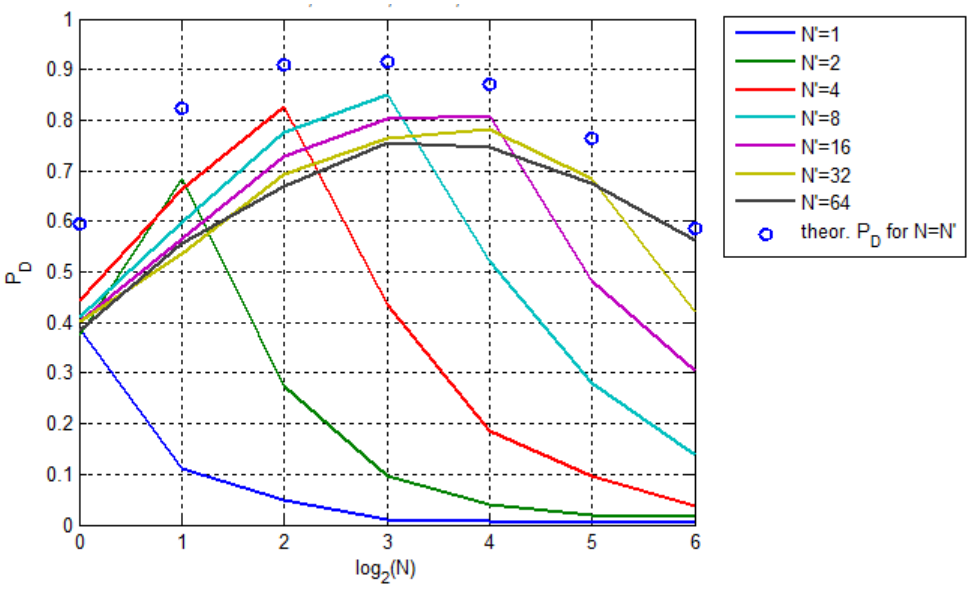

Figure 3.21. P_D versus $\log_2(N)$ for r=0.95 v=500m/s

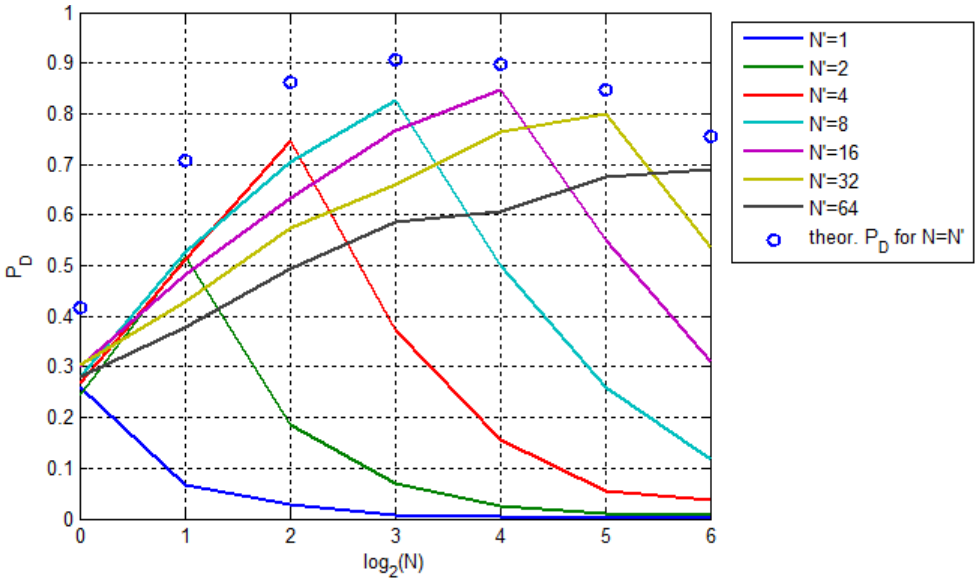

Figure 3.22. P_D versus $\log_2(N)$ for r=1 v=500m/s

Figure 3.23 shows P_D versus $\log_2(N)$ when SNR is increased 0.8dB with respect to Figure 3.21. It shows that almost same P_D curve can be obtained with a 0.8 dB SNR loss for r=0.9 when there is range migration and Keystone Transform is applied.

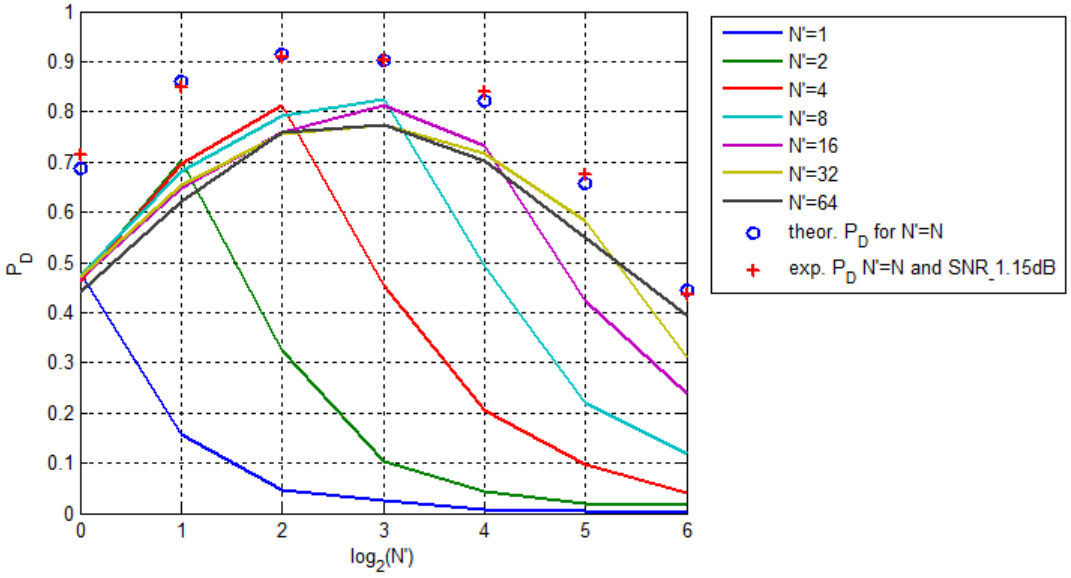

Figure 3.23. P_D versus $\log_2(N)$ for r=0.9 v=500m/s

To summarize, simulation results show that **(i)** it is possible to find which *N* value gives the best detection probability for a given combination of SNR, correlation coefficient and total number of pulses, and **(ii)** there is a degradation in detection performance of about 0.8 dB SNR due to interpolation loss during KT when KT is applied to remove range migration for moderately fluctuating targets.

3.4 Range Migration Compensation by KT Under Sea Clutter

In this section, we examine the case where both range migration and sea clutter exist. Firstly, we generate realistic synthetic clutter data. Next, we perform a numerical simulation where we suppress the clutter and apply KT.

3.4.1 Realistic Synthetic Clutter Generation

In order to see the effect of the sea clutter on the performance of Keystone Transform, a simulation has been implemented. Real data [48] is used to generate realistic clutter. Environment information and radar parameters associated with the data is given in Table 3.8. Real data is composed of radar echo collected for 14 seconds. Real data is composed of 33001×31 array as shown in Figure 3.24, corresponding to 31 range gate and 33001 pulses. In Figure 3.25, range-time intensity plot of the real data is shown. In this dataset, a pencil duck has been deployed at sea in the range of 3485m. We can obtain clutter data if we crop the part of the data corresponding to the range up to 3500m. After cropping, the new range-time intensity plot of the clutter data is shown in Figure 3.26.

Table 3.8 Environment information and radar parameters associated with the real clutter data

Wind speed [m/s]	9.1
Maximum (gust) speed [m/s]	13.4
Direction of wind [°N]	191
Maximum height of wave [m]	4.56
Wave direction [°N]	160
Wave period [s]	14.29
Pulse repetition interval [s]	4e-4
Sampling period [s]	1e-7
Pulse width [s]	1e-7
Polarization of antenna	VV
Transmit frequency [Hz]	9e9

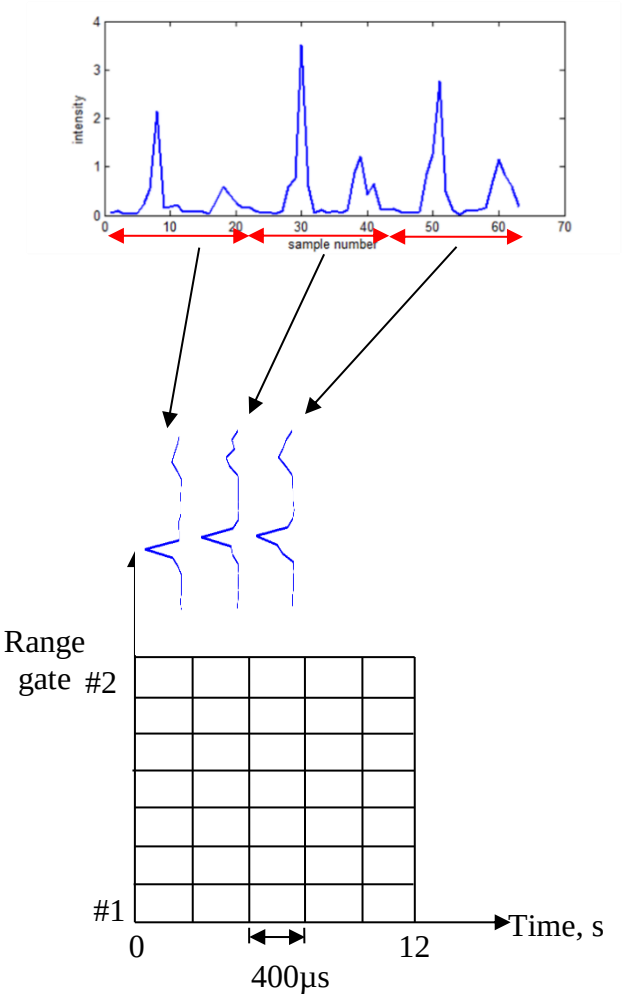

Figure 3.24. Real array data

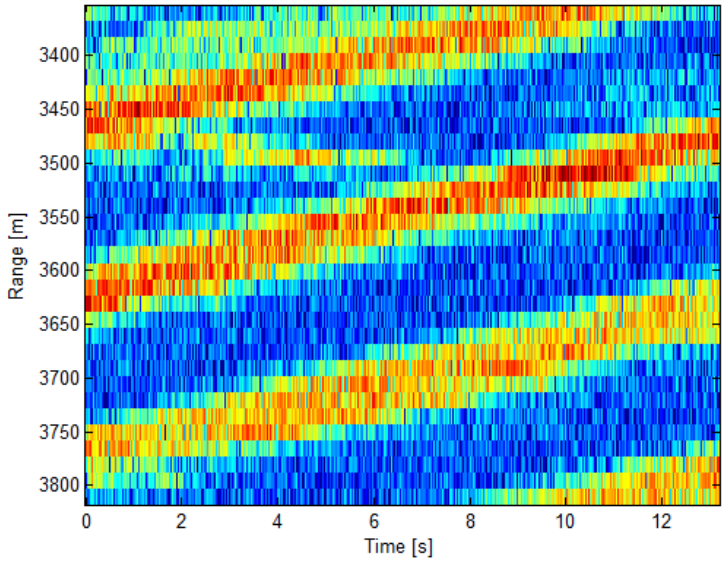

Figure 3.25. Range-time intensity plot of the real data

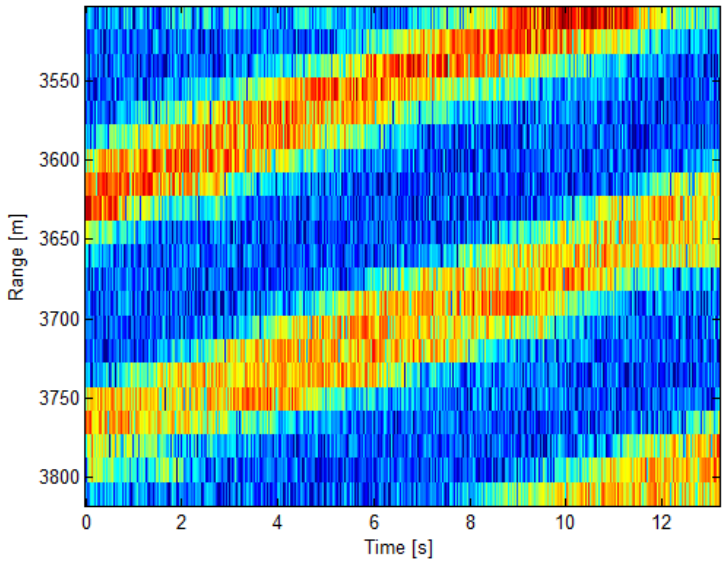

Figure 3.26 Range-time intensity plot of the clutter data

The goal is to generate a synthetic clutter data which has similar characteristics of the real clutter data. Firstly, the texture component of the real clutter data can be obtained by averaging the intensity of the clutter. Then, we generate a new speckle

component. Finally, by combining the speckle and the texture components we obtain a generated clutter data which has a similar characteristics of real clutter data.

According to compound K-distribution model [37], samples of the complex envelope of the sea clutter process are stated as the multiplication of two components $c(t_f, t_s) = \sqrt{\tau(t_f, t_s)}x(t_f, t_s)$ where τ is gamma distributed texture component, and $x(t_f, t_s) = x_I(t_f, t_s) + x_Q(t_f, t_s)$ is a complex Gaussian process; x_I and x_Q are the in-phase and quadrature components which are supposed to meet $E_{t_s}\{x_I(t_f, t_s)\} = 0$, $E_{t_s}\{x_Q(t_f, t_s)\} = 0$ with $E_{t_s}\left\{\left(x_Q(t_f, t_s)^2\right)\right\} = E_{t_s}\left\{\left(x_I(t_f, t_s)^2\right)\right\} = \frac{1}{2}$, t_f is fast time, t_s is slow time.

Average power of the backscattered signal over time T is as follows

$$\frac{1}{T}\int_T |c(t_f, t_s)|^2 dt_s = \frac{1}{T}\int_T |\tau(t_f, t_s)||x(t_f, t_s)|^2 dt_s \tag{3.81}$$

In fact, the texture is assumed to be constant during each CPI due to its long correlation time. When T is less than or comparable with CPI, texture can be considered constant. Using the assumption $E_{t_s}\left\{\left(x(t_f, t_s)^2\right)\right\} = 1$, we obtain average power gives estimate of texture.

$$\frac{1}{T}\int_T |c(t_f, t_s)|^2 dt_s = |\tau(t_f, t_s)|\frac{1}{T}\int_T |x(t_f, t_s)|^2 dt_s \approx |\tau(t_f, t_s)| \tag{3.82}$$

To get an estimate of the texture component, we find the average intensity of the array for each range bin in Figure 3.26. For instance, Figure 3.27 shows intensity of the original data for 16th range bin and the average intensity for a moving window of

length 256. Figure 3.28 shows range-time plot of the estimated texture component for whole array.

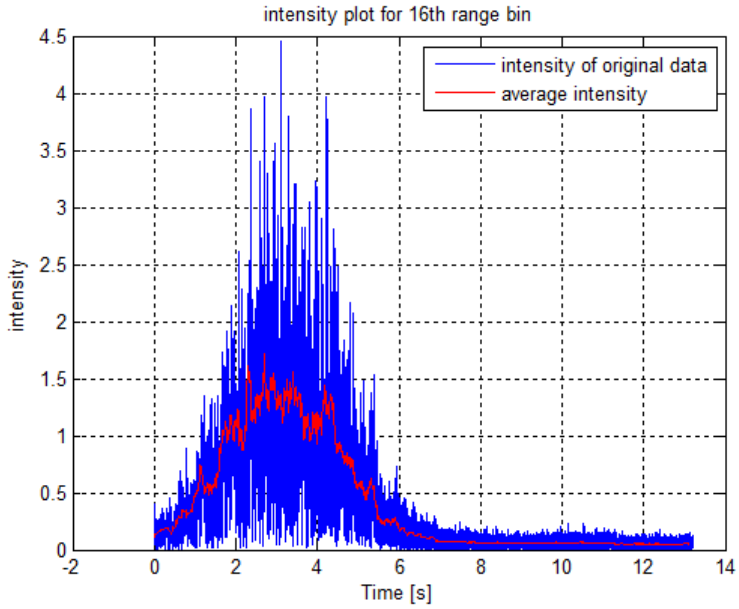

Figure 3.27. Range-time intensity plot

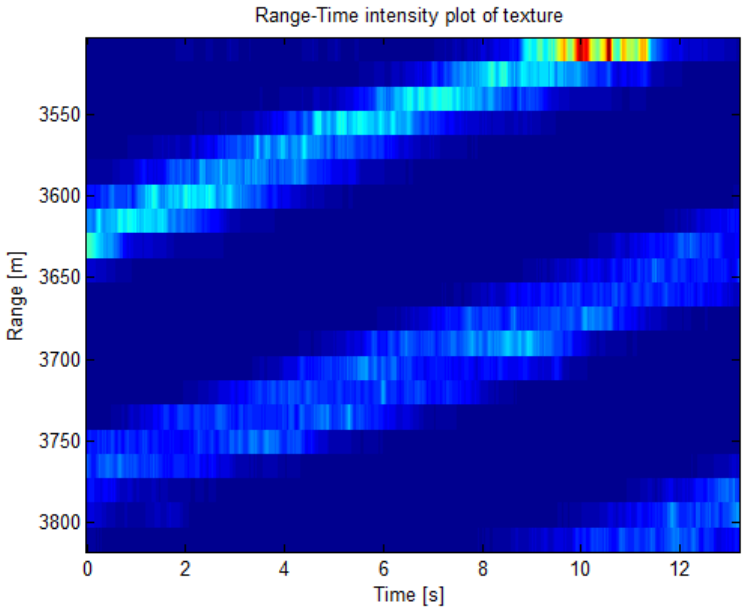

Figure 3.28. Range-time plot of the estimated texture

In the simulation, we will take the number of pulses in a coherent pulse interval (CPI) as N=256. So, first 256 samples for each range bin are used in the simulations. Range-Time intensity plot of the original data in the 1st CPI is given in Figure 3.29. Figure 3.30 shows the range-time intensity plot of texture in the first CPI.

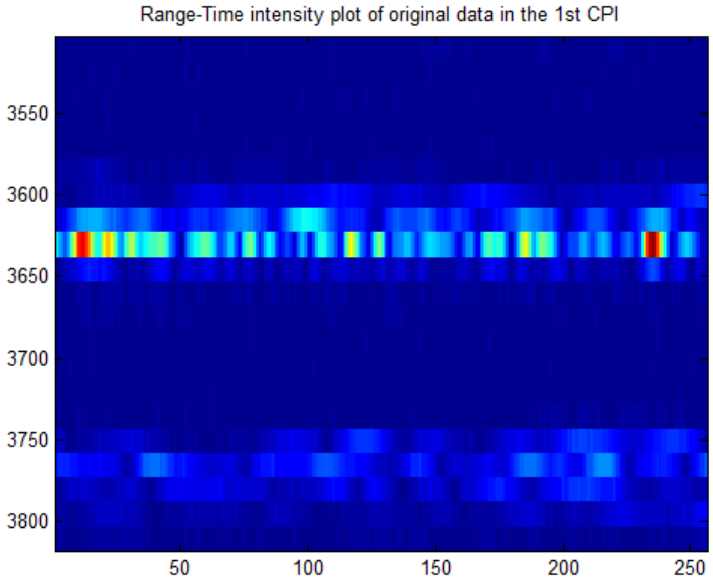

Figure 3.29. Range-Time intensity plot of original data in the 1st CPI

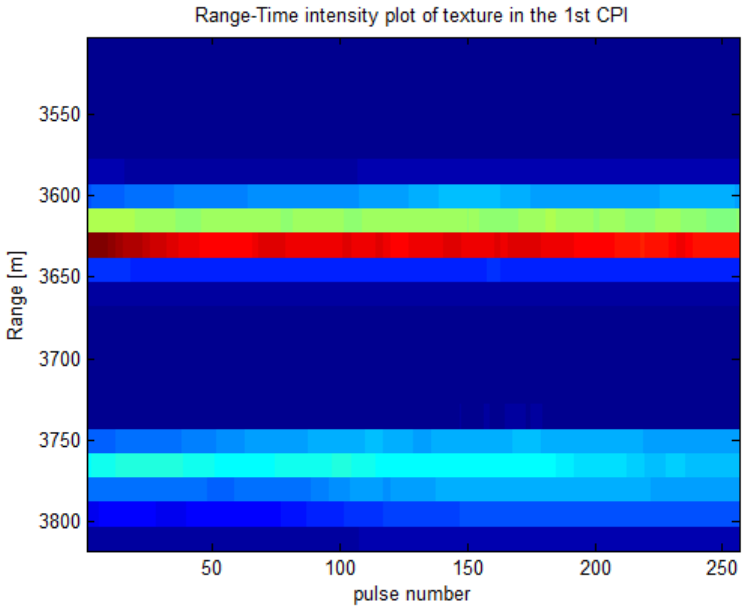

Figure 3.30. Range-time intensity plot of texture in the first CPI

Since it is stated in [37] that speckle component decorrelates in the order of 10ms, we can generate correlated Rayleigh random variables with decorrelation time of 10ms to obtain our speckle component of clutter. Range time plot of the generated speckle is given in Figure 3.31.

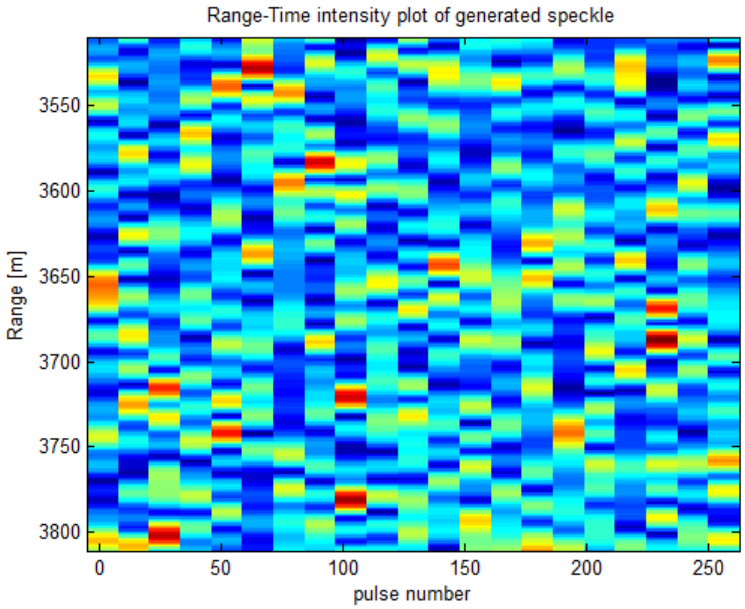

Figure 3.31. Range time plot of the generated speckle

By multiplying the square-root of the texture with generated speckle, we get a generated clutter data which has a similar characteristics of real clutter data. Figure 3.32 shows the range time plot of generated clutter.

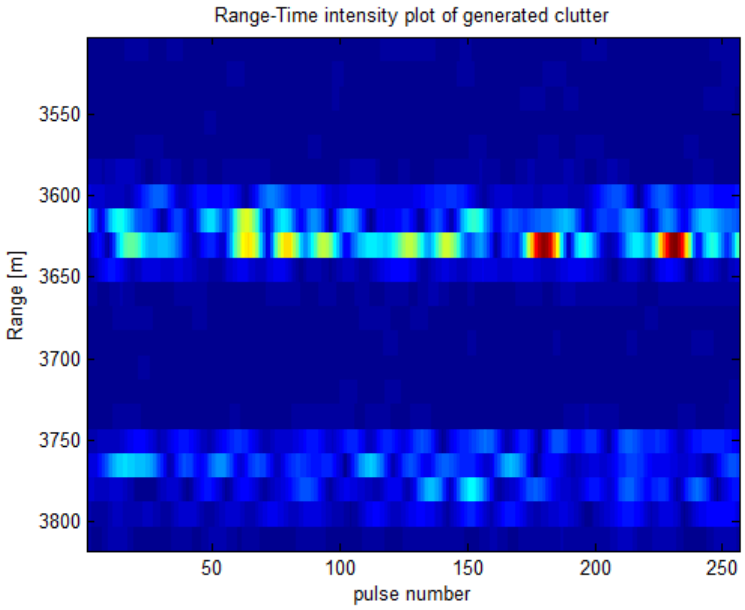

Figure 3.32. Range time plot of the generated clutter

Now, we can compose the signal backscatters from the target. It is assumed the target has a radial velocity of v=300m/s and an initial range of 3555m. In this simulation, Swerling-0 type nonfluctuating target has been created.

The received signal is the summation of clutter echo, target echo and additive white Gaussian noise of 3dB.

The clutter echo can be constituted by using a tapped-delay line channel model as assumed in [49]. The truncated tapped-delay line model is shown in Figure 3.33. Assuming the channel is slowly fading and frequently selective, the noiseless received signal from the channel can be expressed in the form

$$r_l(t) = \sum_{n=1}^{L} c_n(t)\, s_l(t - n/W) \tag{3.83}$$

where W is the bandwidth used by the real bandpass signal, $s_l(t)$ is lowpass equivalent signal transmitted through the channel, $c_n(t)$ is time-variable channel coefficients, and L is the truncation size.

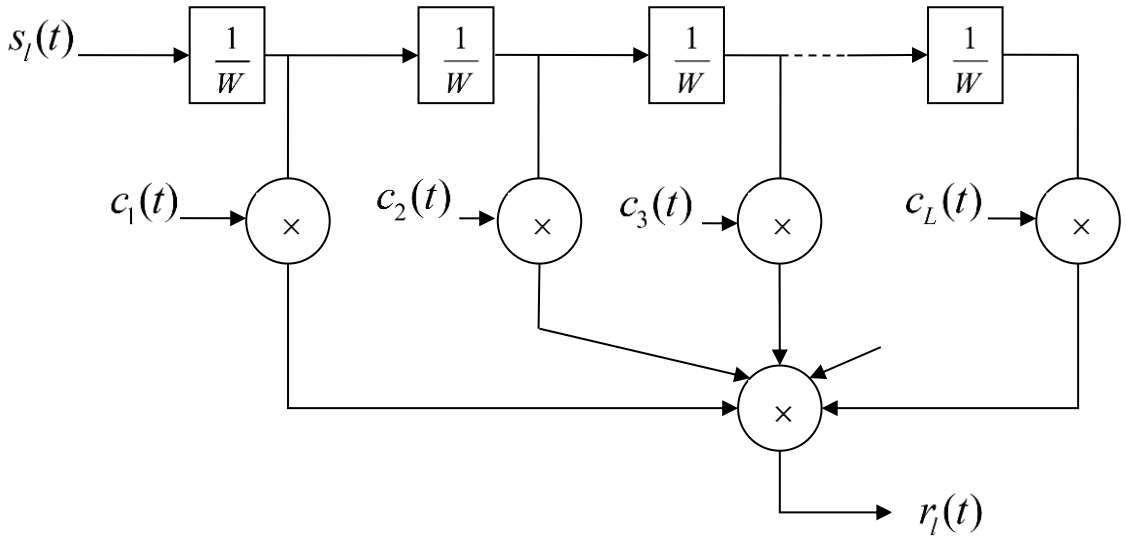

Figure 3.33. Tapped-delay line model of the channel

3.4.2 Numerical Simulation

A numerical simulation has been performed to examine the performance of KT and clutter suppression together. Simulation parameters are shown in Table 3.9.

Table 3.9 Simulation parameters

Signal to Clutter Ratio	-10.7dB
Signal to Noise Ratio	3 dB
Radial target velocity	300 m/s
Number of pulses in CPI	256
Decorrelation time of speckle component	10 ms

It is observed in real data that the clutter echoes are not stationary and have a speed of about 4m/s. Hence, the output of the tapped-delay line channel is created as it has a speed of 4m/s.

Range-Time plot for this received signal is given in Figure 3.34.

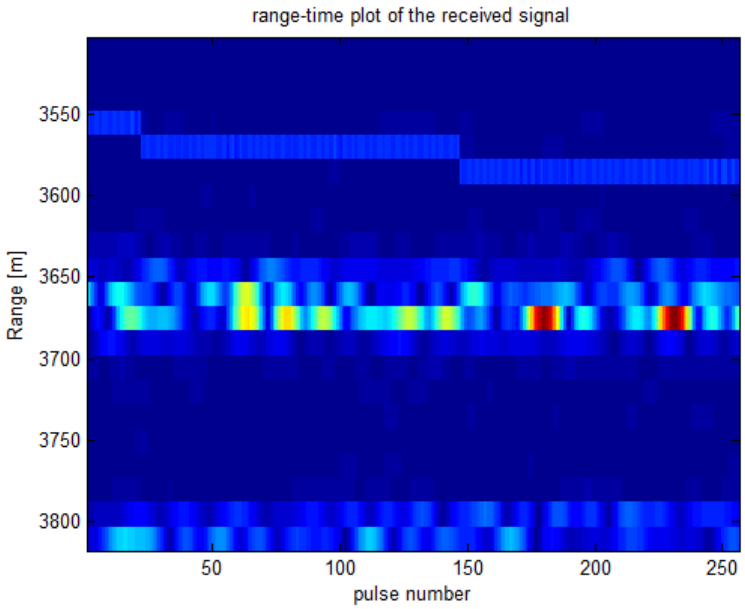

Figure 3.34. Range-Time plot of the received signal

Range-Doppler plot of the received signal is shown in Figure 3.35.

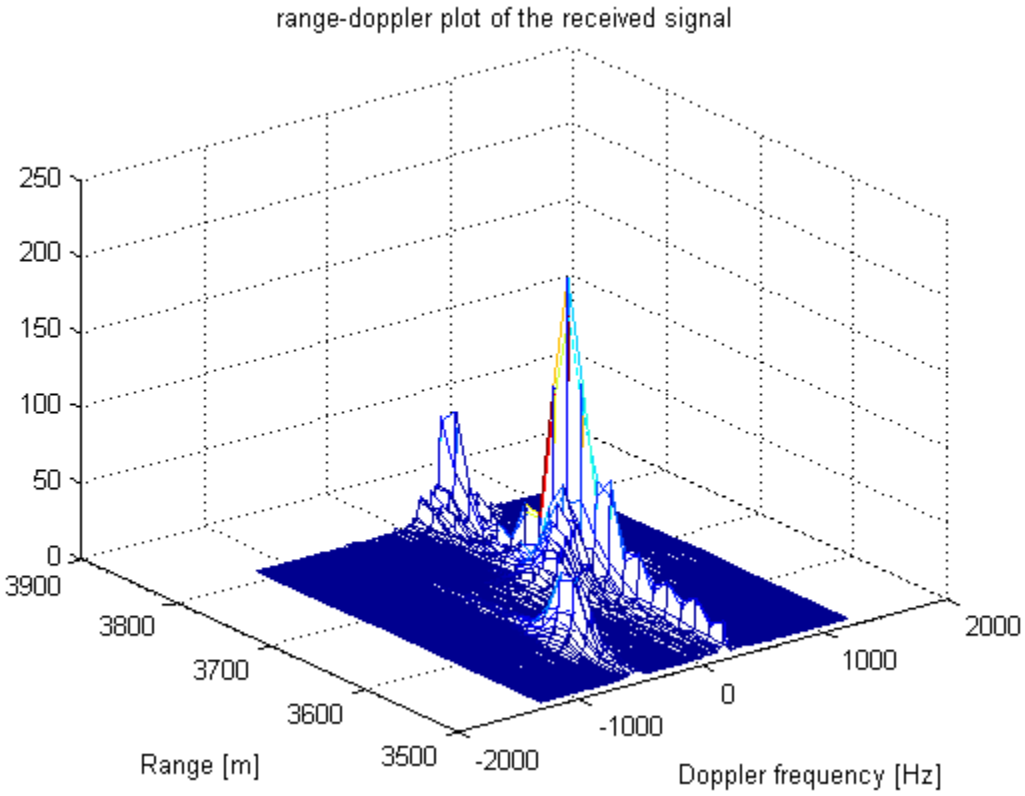

Figure 3.35. Range-Doppler plot of the received signal

Clutter effects can be reduced by suppressing the low Doppler frequencies. A simple 4-delay line canceller can be used to suppress the signals having low Doppler frequencies [2].

After reducing the clutter, the Range-Doppler plot is as shown in Figure 3.36.

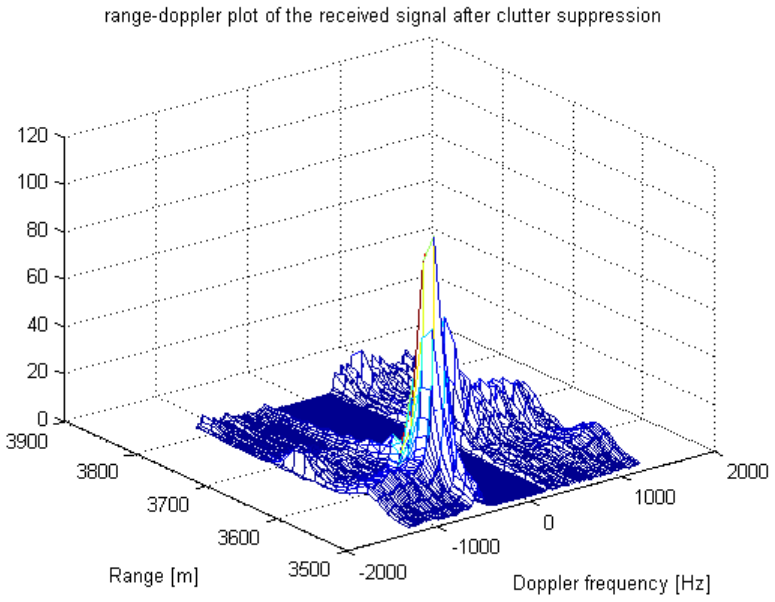

Figure 3.36. Range-Doppler plot after clutter reduction

Coherent integration output of the received signal after clutter suppression and KT applied is shown in Figure 3.37.

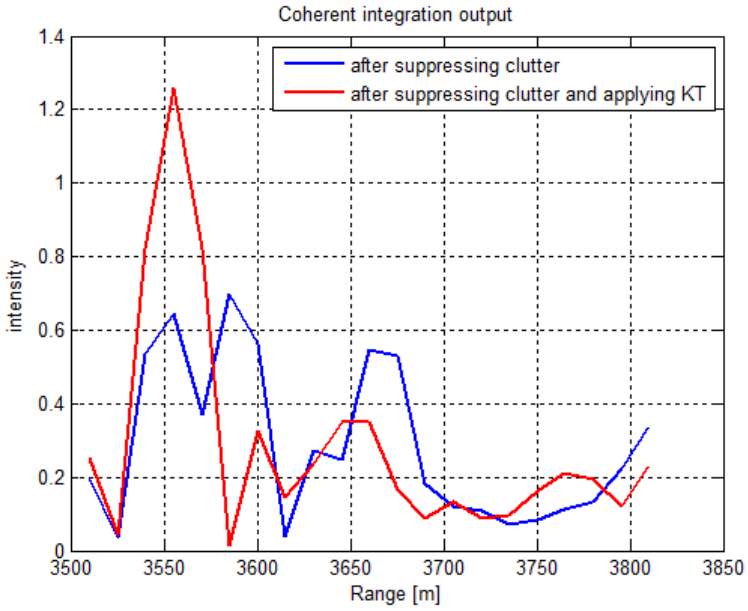

Figure 3.37. Coherent integration output of the received signal after clutter suppression and KT applied

Note that amplitude of coherent integration output is higher in range of 3555m when KT is applied. Hence, we have shown that detection performance can be improved if KT is applied after suppressing the clutter.

3.5 Range Migration Compensation by KT under Rain Clutter

In this section, we investigate the case where KT is applied for range migrating targets under rain clutter. We will compare performances for both cases where

i. we suppress the rain clutter first and then apply KT,

ii. we apply KT first before suppressing the rain clutter.

We used the following parameters in the simulations:

Table 3.10 Simulation Parameters

Parameters	**Value**
Carrier frequency	9 GHz
Pulse width	30μs
Bandwidth	20MHz
N -number of pulses in CPI	64
PRI	75μs
Target velocity	15.125 v_{blind}
Range resolution	7.5m

Range migration during one CPI	16.13m
SCR	-30B

The received signal is composed of target and clutter component. Range-Doppler plot of the received signal is given in Figure 3.38.

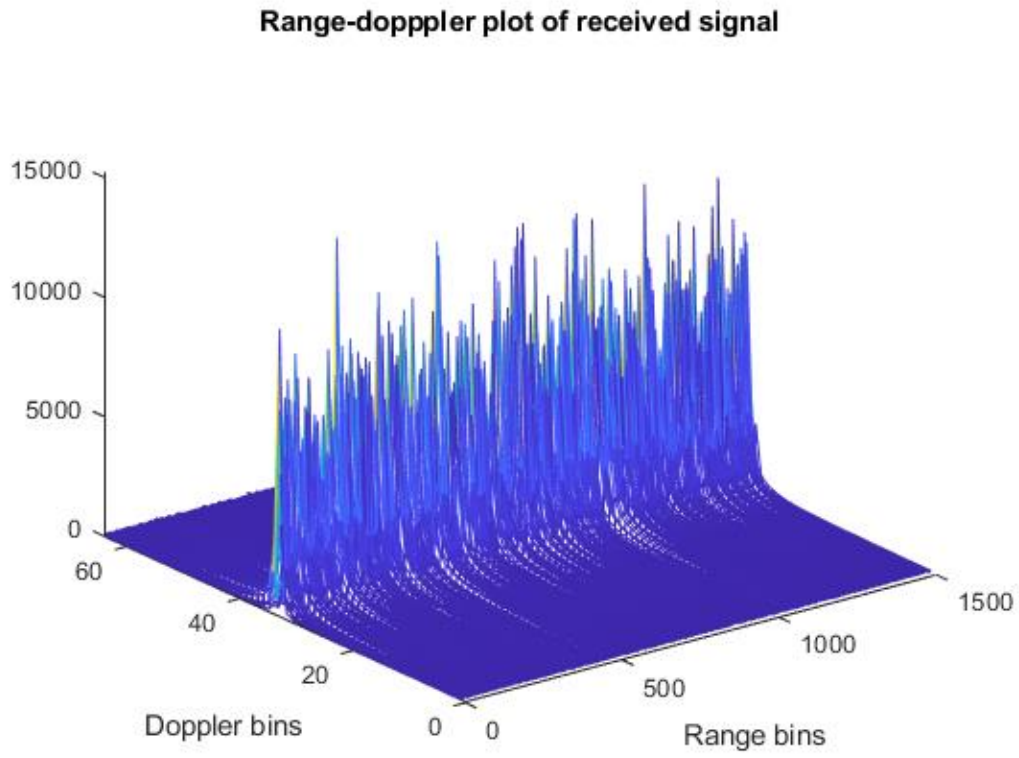

Figure 3.38. Range-Doppler plot of the received signal

Range-Doppler plot after applying sinc interpolation is given in Figure 3.39

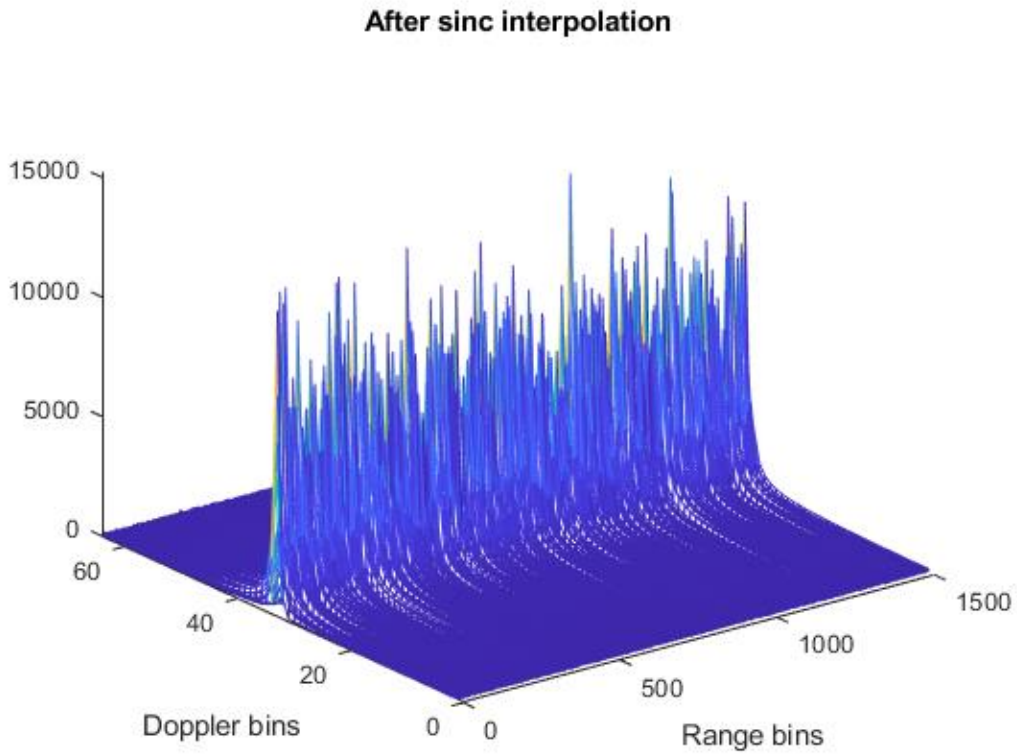

Figure 3.39. Range-Doppler plot after applying sinc interpolation

Figure 3.40 shows the Range-Doppler plot after sinc interpolation and Doppler ambiguity correction has been applied respectively. It is seen that Doppler spectrum has been enlarged after Doppler ambiguity correction. MTI filter after Doppler ambiguity correction is not expected to suppress clutter perfectly since the MTI filter is applied according to clutter covariance matrix before Doppler ambiguity correction.

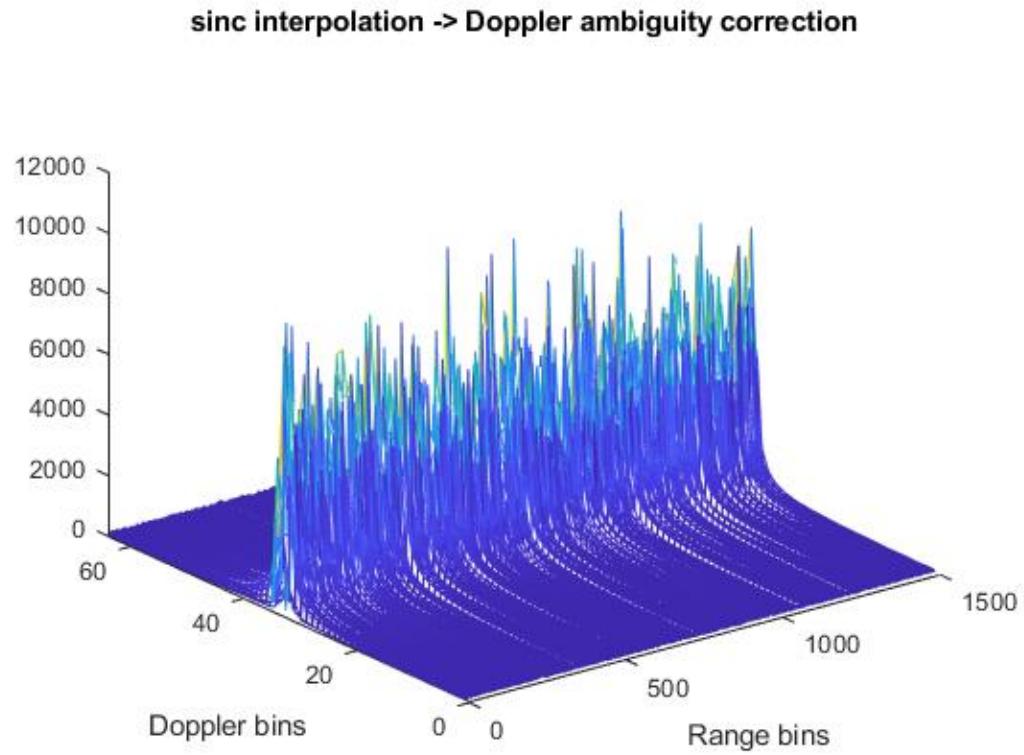

Figure 3.40. Range-Doppler plot after sinc interpolation, Doppler ambiguity has been applied respectively

Figure 3.41 shows Range-Doppler plot after sinc interpolation, Doppler ambiguity and MTI filter has been applied respectively.

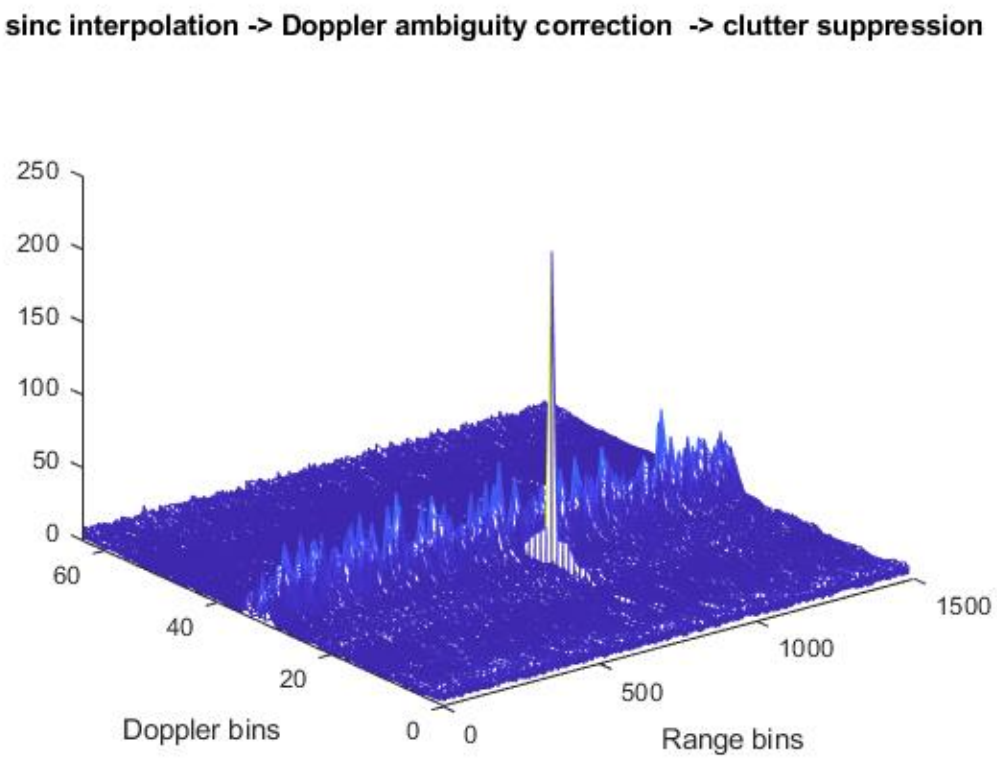

Figure 3.41. Range Doppler plot after KT and clutter suppression applied respectively.

Figure 3.42 shows Range-Doppler plot when we apply sinc interpolation, clutter suppression and Doppler ambiguity correction respectively. Clutter has been suppressed better with respect to Figure 3.41, as expected.

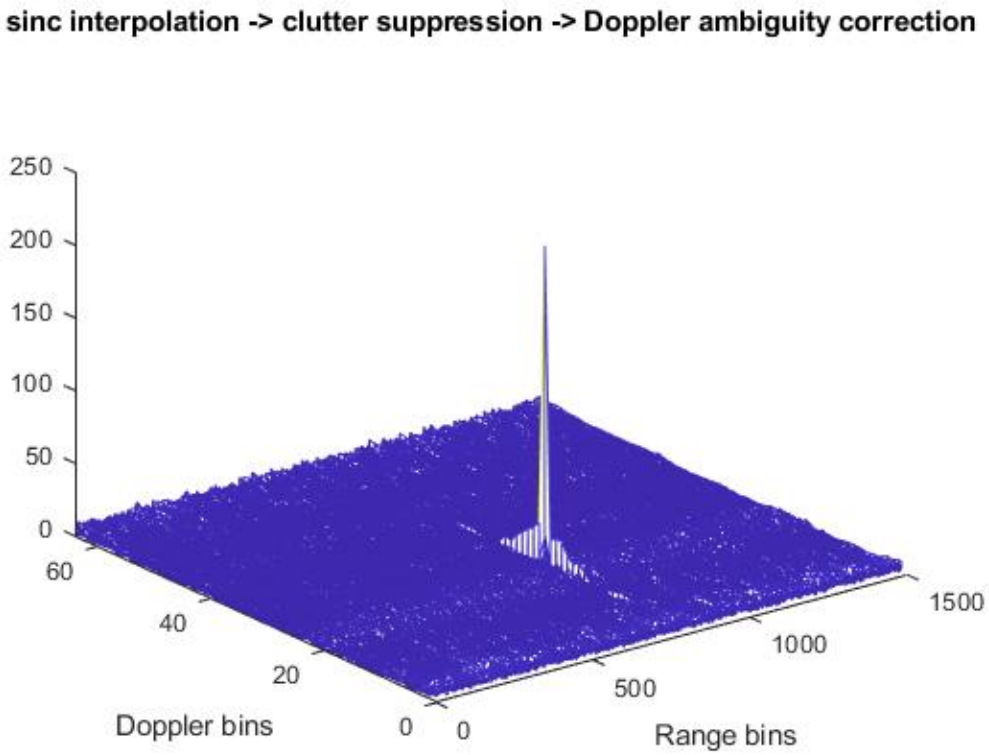

Figure 3.42. Range-Doppler plot when we apply sinc interpolation, clutter suppression and Doppler ambiguity correction respectively

Figure 3.43 shows Range-Doppler plot when clutter is suppressed and KT is applied respectively. It has better clutter suppression performance with respect to Figure 3.41.

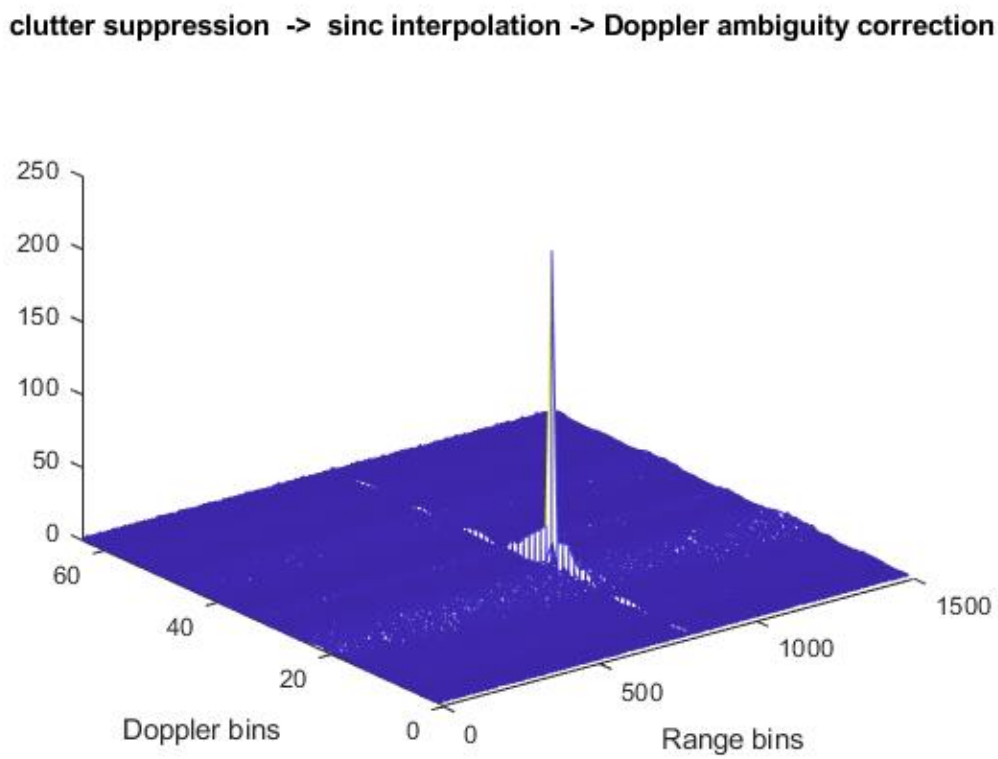

Figure 3.43. Range-Doppler plot when clutter is suppressed and KT is applied respectively

Hence, we can conclude that suppressing the clutter before applying KT improves performance more especially in clutter suppression compared to applying KT before suppressing the clutter.

Note that we assume static clutter covariance for rain clutter. In case of variable clutter characteristics, adaptive clutter estimation methods [50] can be applied. In such a case, performance could be improved by joint methods, i.e. considering solving clutter suppression and targeting detection problems together instead of sequential operations.

3.6 Range Migrating Target Detection in Range Migrating Clutter

When the radar has high velocity motion, range of clutter backscattered from rain or cloud will migrate, and classical clutter suppression techniques will not work due to range migration of clutter. In this section, we propose a method to solve range migration problem jointly for range migrating clutter and the range migrating target. In such a case, we need to align range profiles of clutter before suppressing clutter. Then, we can align range profiles of target. The flow diagram of the proposed algorithm is given in Figure 3.44.

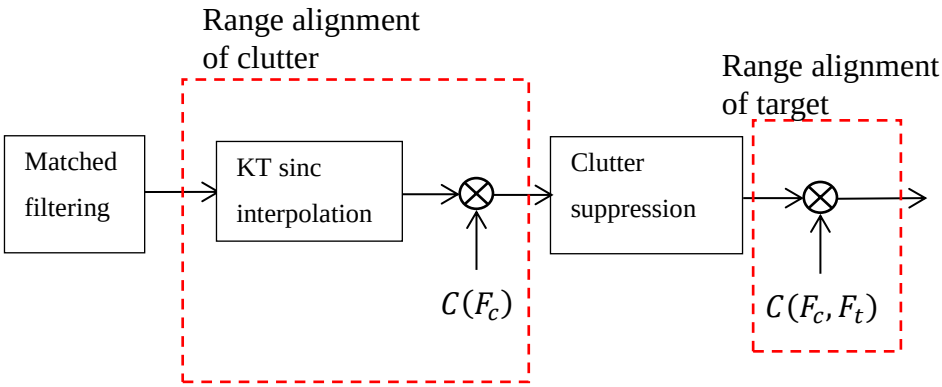

Figure 3.44. Range alignment of range migrating clutter and target

After matched filtering, range alignment of clutter can be done by applying KT without sweeping all possible Doppler ambiguity factors, because we know radar platform's velocity and find Doppler ambiguity factor corresponding to platform's velocity. Thus, range alignment of clutter includes sinc interpolation and Doppler ambiguity correction, which can be performed by employing (2.12) and (2.16) respectively. Doppler ambiguity correction term can be found by following expression:

$$C(F_c) = \exp\left[-j2\pi F_c \frac{mf_c}{(f_c + f)}\right] \tag{3.84}$$

where F_c is Doppler ambiguity factor for radial speed between clutter and radar.

Then, clutter can be suppressed easily if we have clutter statistics. Since we performed interpolation step of KT while we are aligning clutter range profiles, we do not need to perform interpolation step of KT again for range alignment of target once more. It will be sufficient to correct Doppler ambiguity for target. However, we should take into consideration that we corrected Doppler ambiguity for clutter. Doppler ambiguity correction can be performed as given in (2.16). Therefore, we will update Doppler ambiguity correction term as follows:

$$C(F_c, F_t) = exp\left[-j2\pi(F_t - F_c)\frac{mf_c}{(f_c + f)}\right] \tag{3.85}$$

where F_t is Doppler ambiguity factor for radial velocity between target and radar.

By this proposed method, we can align range profiles of both clutter and target without bringing additional computational cost with respect to only range alignment of target.

3.6.1 Simulation

We have the following scenario and radar parameters:

Table 3.11 Scenario and radar parameters

Radar platform velocity	312 m/s
Target velocity	616 m/s (approaching)
Carrier frequency	9 GHz
Pulse width	30μs
Bandwidth, B	20MHz
N -number of pulses in CPI	32

Table 3.11 continues

PRI	480μs
Range resolution	7.5m
SCR	-30B

Table 3.12 Rain clutter simulation parameters

Parameter	**Value**	**Explanation**
R	15000	the slant range to clutter in m
ΔR	7.5	Range resolution, m
η	-62dB	Volume reflectivity of rain for 9.3GHz, m^{-1}
φ_2	2.8	the two-way half power antenna elevation beamwidth in degree
k	4	the velocity gradient in the vertical direction of the beam in m/s/km
V_0	10	the wind speed in the beam center in m/s
θ_2	2.8	the two-way half power antenna azimuth beam width in degree
β	45	the azimuth angle relative to the wind direction at beam center in degree
ψ	10	the elevation angle in degree
σ_{turb}	1	m/s
σ_{shear}	0.82	m/s

Table 3.12 continues

σ_{beam}	0.16	m/s
σ_{fall}	0.17	m/s
σ_v	1.31	Standard deviation of Doppler velocity spectrum m/s
σ_f	78.6	Standard deviation of Doppler frequency spectrum Hz
V	3.3e4	Volume resolution cell
SCR	-1.92dB	Signal to clutter ratio (before considering attenuation)
v_z	5	Rain fall velocity, m/s
v_w	8 : upper limit Beaufort-4	Wind speed, m/s
v_p	0	Radar platform velocity, m/s
$A_w - A_b$	45	Azimuth angle between beam axis and wind, degrees
v_0	6.5	Mean clutter velocity, m/s

In simulations, optimum MTI filter is used for clutter suppression. Figure 3.45-Figure 3.47 show range - Doppler plot after range alignment of clutter, clutter suppression and range alignment of target, respectively, which are the steps of block diagram shown in Figure 3.44.

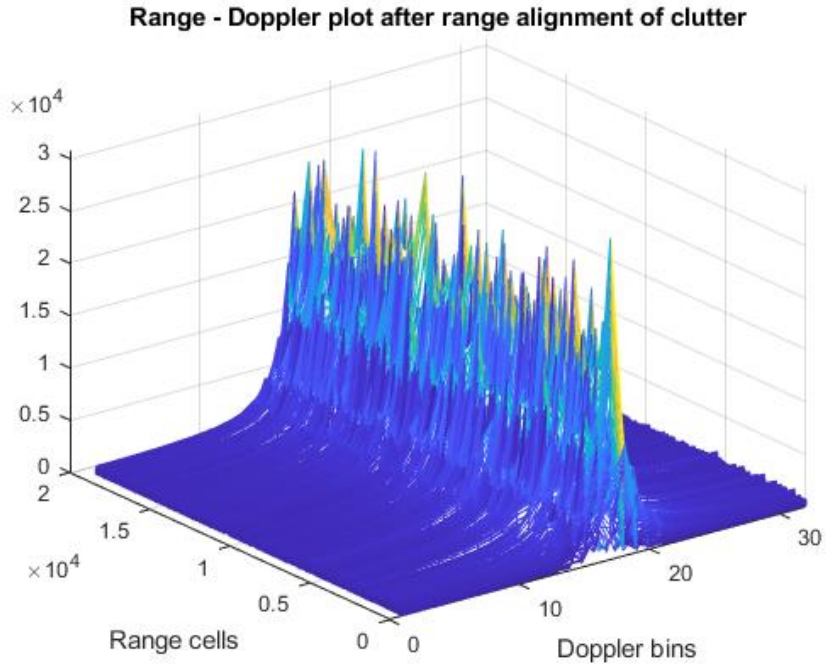

Figure 3.45. Range - Doppler plot after range alignment of clutter

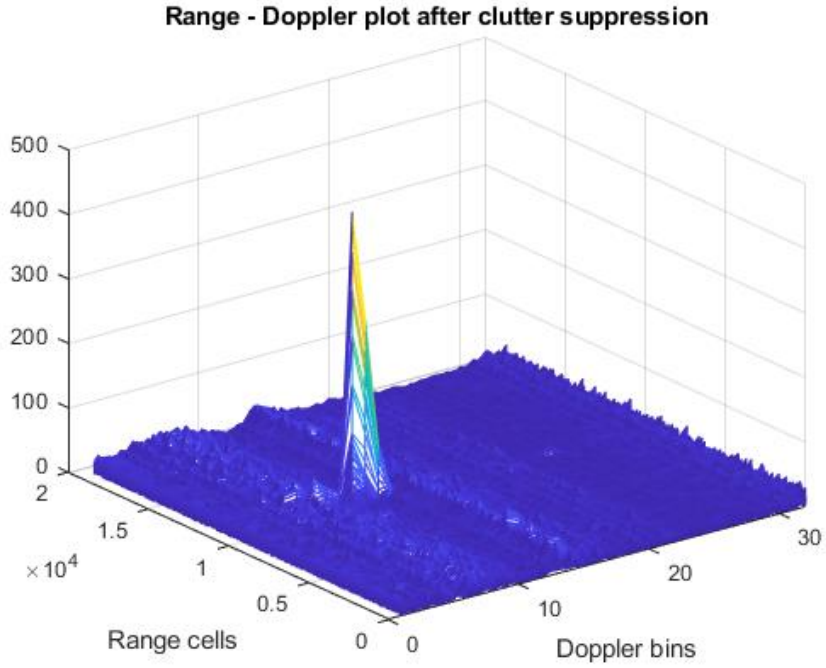

Figure 3.46. Range - Doppler plot after clutter suppression

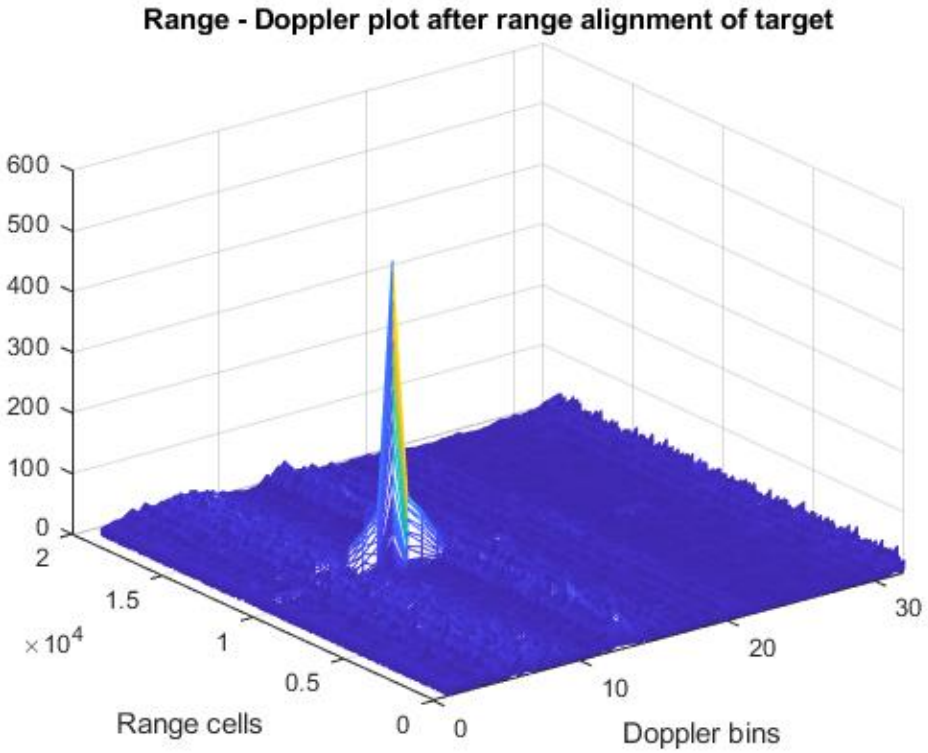

Figure 3.47. Range - Doppler plot after range alignment of target

Comparing Figure 3.46 with Figure 3.45, we note that clutter has been suppressed and we have only range migrating target in range-Doppler plot. We can notice that amplitude of range-Doppler plot has been amplified after aligning the target's range profiles in Figure 3.47.

In addition, performance for different Doppler velocity of target are examined. Figure 3.48 shows IF vs ratio of Doppler velocity to blind speed. As expected, we obtain higher IF performance when target velocity is further away from clutter speed.

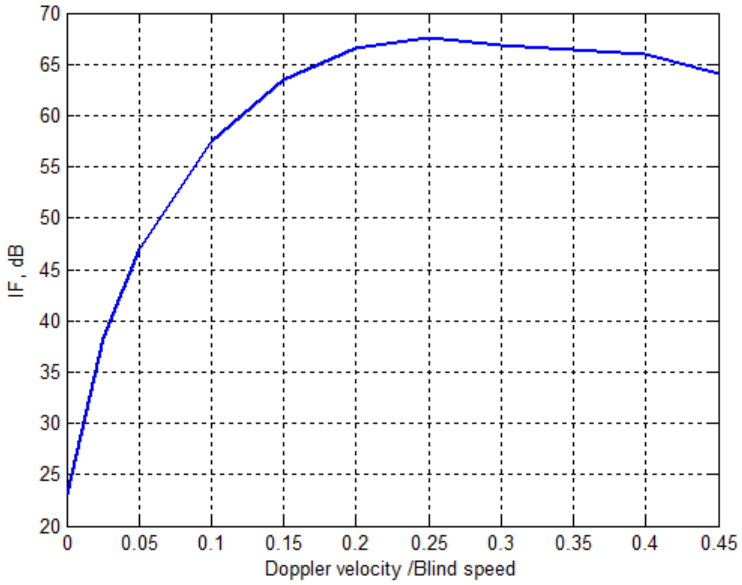

Figure 3.48. IF vs ratio of Doppler velocity to blind speed

Furthermore, IF performance against Doppler spread of clutter is examined and shown in Figure 3.49. We observe that IF performance degrades with increasing Doppler spread.

Hence, we have shown effectiveness of the proposed method by numerical simulations.

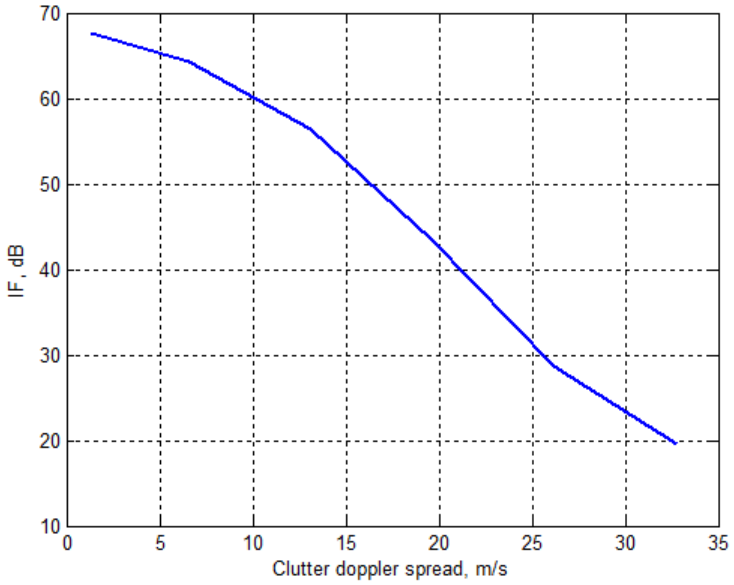

Figure 3.49. IF against Doppler spread of clutter

CHAPTER 4

PROPOSED RANGE MIGRATION COMPENSATION METHODS

In this chapter, we propose two different methods (published in [51] and [52]) to compensate range migration with lower computational complexity than the KT and the RFT while achieving similar detection performance.

4.1 Efficient Implementation of KT and RFT Utilizing CZT [51]

We propose an efficient new technique to repeat execution of the CZT with different initial points and the same angular distance on the spiral contour. Consequently, not only the KT and the RFT can be applied with lower computational load using the proposed method but also possibly other applications demanding to repeat execution of the CZT. Mathematical analysis shows that the proposed technique is same as the standard CZT algorithm. Therefore, the same detection performance can be achieved with lower computational load as the existing KT and RFT implementations by implementing the KT and the RFT using the proposed method. In addition, we show by computer simulations that there is no performance loss compared to the standard KT and RFT.

Implementation of the KT algorithm using the repeated execution of the CZT has been reviewed in 2.2.4. Doppler ambiguity compensation, CZT and IFFT over range frequency is repeated N_F times, where N_F denotes the number of possible values of Doppler ambiguity factor F.

4.1.1 A New RFT method to execute repeated CZT

We can write the matched filter output as given in (4.1).

$$Y(f,n) = |P(f)|^2 \exp[-j4\pi(f+f_c)\frac{(R_0 + vnT_r)}{c}] \tag{4.1}$$

Radial velocity between the radar and the target is represented as follows

$$v = Fv_{blind} + v_{res} \tag{4.2}$$

where Doppler ambiguity factor is $F = round(v/v_{blind})$; $round(.)$ is the function which returns the nearest integer, blind speed is defined as $v_{blind} = \frac{c}{2f_cT_r}$, v_{res} is the residual velocity with $|v_{res}| < \frac{v_{blind}}{2}$.

If (4.2) is substituted in (4.1), we obtain the following expression:

$$\begin{aligned} Y(f,n,F) &= |P(f)|^2 \exp[-j2\pi(f+f_c)\frac{2R_0}{c}] \\ &\times \exp[-j2\pi(f+f_c)\frac{2v_{res}}{c}T_r n]\exp[-j2\pi F\alpha_f n] \end{aligned} \tag{4.3}$$

where $\alpha_f = \frac{f_c+f}{f_c}$.

Doppler ambiguity compensation can be performed as follows

$$Y_{c,RFT}(f,n,F) = Y(f,n,F)C_{RFT}(f,n,F) \tag{4.4}$$

where we define Doppler ambiguity compensation factor as

$C_{RFT}(f,n,F) = \exp[j2\pi F\alpha_f n]$.

After compensating the Doppler ambiguity, we have the following expression

$$Y_{c,RFT}(f,n,F) = |P(f)|^2 \exp\left[-j2\pi(f+f_c)\frac{2R_0}{c}\right] \exp[-j2\pi(f+f_c)\frac{2v_{res}}{c}T_r n] \quad (4.5)$$

We do not have to search for all possible velocity values. Rather, the ambiguity is compensated and the residual velocity is searched assuming known Doppler ambiguity factor *F*. Thanks to the CZT[1], we can search the residual velocity index *k*:

$$Z_{RFT}(f,k,F) = \underset{n}{CZT}[Y_{c,RFT}(f,n,F)] \quad (4.6)$$

where CZT parameters are given as A=1 and $W_f = \exp[j2\pi(f+f_c)\frac{2\Delta v}{c}T_r]$. If there is equality between the searching residual velocity and the true residual velocity, i.e. $v_{res} = k\Delta v$, amplitude of the coherent integration output shown in (4.6) is maximum.

If the Doppler ambiguity is unknown, it can be found by searching coherent integration outputs giving the maximum peak amplitude over the potential ambiguity factor *F* values. The following expression shows how to find coherent integration

$$z_{RFT}(\tilde{t},k,F) = \underset{f}{IFFT}[Z_{RFT}(f,k,F)] \quad (4.7)$$

where *k* is the search velocity index.

[1] CZT is defined in 2.2.4

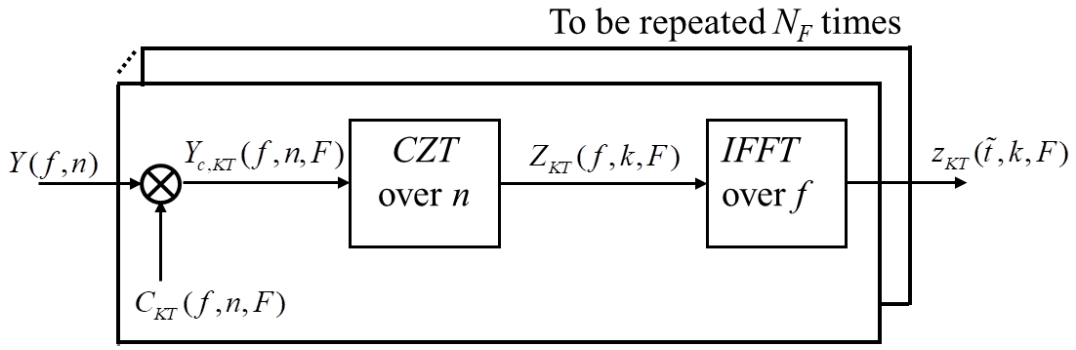

Figure 4.1. Implementation of KT employing repeated CZT operations

To summarize, we represent single formulation to implement both the KT and the RFT using repeated CZT. Figure 4.1 represents not only implementation of the KT with repeated CZT but also block diagram of the RFT using repeated CZT.

4.1.2 Proposed method for efficient implementation of recurrent CZT

As mentioned in 4.1.1, Doppler ambiguity compensation and CZT operation is repeated for possible values of ambiguity factor in the RFT and the KT implementations. There are 2 tricks to be employed for reduction of computational load of both implementations:

1. Instead of multiplying with an ambiguity correction term, initial point of CZT can be set in terms of f and F. We set $A_f(F) = \exp(-j2\pi F\alpha_f)$ for the RFT and $A_f(F) = \exp(j2\pi F/\alpha_f)$ for the KT.(See Eq. 3.3)
2. We can reduce the computational load of the repetition of CZT operation for various $A_f(F)$ values in the following way.

Calculation of the CZT operation for a particular value of F is given as follows

$$Z(f,k,F) = \sum_n Y(f,n)[A_f(F)]^{-n} W_f^{nk} \tag{4.8}$$

where $Y(f,n)$ is the matched filter output in range frequency and slow time index.

Regarding the 2nd trick, (4.9) is substituted in (4.8):

$$[A_f(F)]^{-n}W_f^{nk} = [A_f(F)]^{k-n}[A_f(F)]^{-k}W_f^{nk} = W_f^{\frac{n^2+k^2-(k-n)^2}{2}} \tag{4.9}$$

$$\begin{aligned} &Z(f,k,F) \\ &= [A_f(F)]^{-k}W_f^{k^2/2}\sum_n W_f^{n^2/2}x(n)W_f^{-(k-n)^2/2}[A_f(F)]^{k-n} \end{aligned} \tag{4.10}$$

Actually $Z(f,k,F)$ includes a convolution:

$$Z(f,k,F) = [A_f(F)]^{-k}W_f^{k^2/2}\sum_n u_f(n)v_f(k-n,F) \tag{4.11}$$

$$Z(f,k,F) = [A_f(F)]^{-k}W_f^{k^2/2}[u_f(n) * v_f(n,F)] \tag{4.12}$$

where $u_f(n) = W_f^{n^2/2}Y(f,n)$, $v_f(n,F) = W_f^{-n^2/2}[A_f(F)]^n\}$ and

* represents convolution.

Convolution operation can be computed by employing IFFT and FFT's:

$$Z(f,k,F) = [A_f(F)]^{-k}W_f^{k^2/2}\underset{n}{IFFT}[\underset{n}{FFT}[u_f(n)]\underset{n}{FFT}[v_f(n,F)]] \tag{4.13}$$

Hence, we obtain (4.13) for the computation of CZT of $Y(f,n)$. The new method proposed to implement CZT is shown in Figure 4.2 as a block diagram.

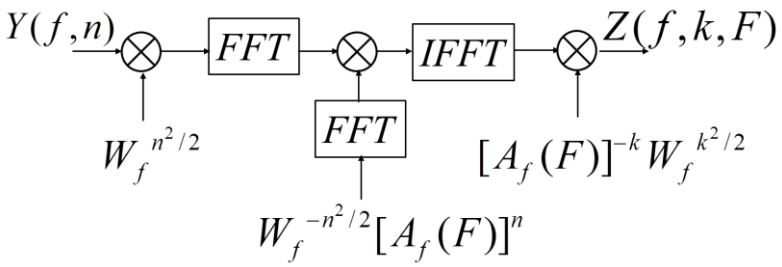

Figure 4.2. New method to implement CZT

If the two tricks are applied, we obtain the block diagram of the proposed RFT and KT implementation as given in Figure 4.3. Note that we must repeat only 1 IFFT operation in the proposed CZT implementation, because we can compute and store FFT of $W_f^{-n^2/2}[A_f(F)]^n$ for all values of F.

After applying the two previously mentioned maneuvers, a modified implementation of KT and RFT employing recurrent CZT operations is obtained as shown in Figure 4.3. Since the prestored values of FFT of $W_f^{-n^2/2}[A_f(F)]^n$ can be used, only one IFFT will be required to be repeated. On the contrary, the RFT and the KT implementations with repeated CZT shown in Figure 4.1 can be performed by repeating single IFFT and FFT for each F.

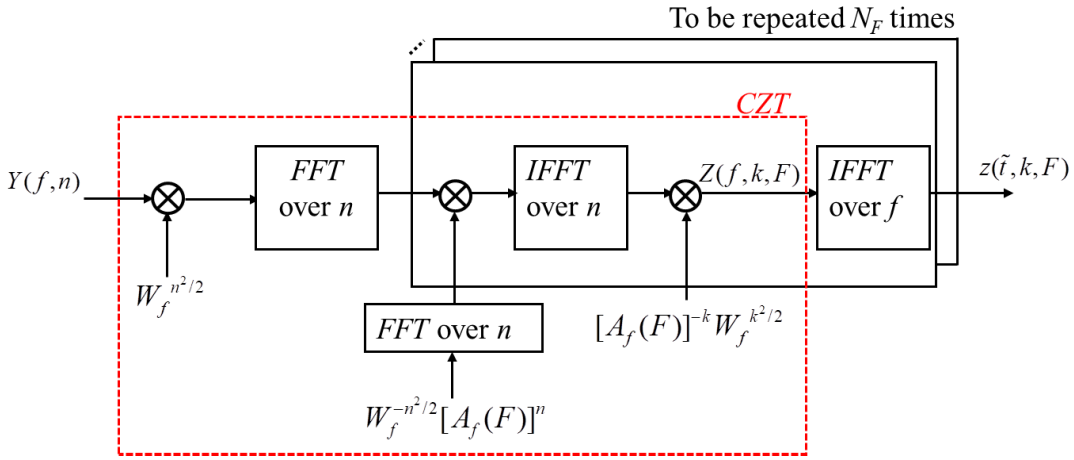

Figure 4.3. Proposed implementation of KT and RFT employing recurrent CZT operations

4.1.3 Computational Load Comparison

Processes in the implementation of the existing RFT and KT algorithms and computational complexity of these processes are given in Table 4.1 –

Table 4.4, where N is the number of pulses to be integrated, M is the number of range bins in PRI, N_F is the total number of ambiguity factors, N_v is the number of searched velocities, and K is the number of search residual velocities. We assume that K is an integer satisfying $N_v = KN_F$. To simplify the investigation, we set $J = N_v + N$, and $T = K + N$.

Table 4.1 Computational load of processes in the existing KT with CZT

Step	**Processing**	**Number of complex multiplications**
Obtaining Y(f,n)	*MN*-point complex multiplication and *N* groups of *M*-point FFT	$MN + \frac{MN}{2} logM$
Ambiguity compensation	N_F groups of *MN*-point complex multiplication	$N_F MN$
CZT over n	N_F repetition of *M* groups of *N*-point CZT of *N*-point input	$2N_F MN log2N$
IFFT over f	N_F repetition of *N* groups of *M*-point IFFT	$N_F \frac{MN}{2} logM$

Table 4.2 Computational load of processes in the proposed KT with CZT

Step	**Processing**	**Number of complex multiplications**
Obtaining Y(f,n)	*MN*-point complex multiplication and *N* groups of *M*-point FFT	$MN + \frac{MN}{2} logM$
CZT over n	N_F repetition of *M* groups of *N*-point modified CZT of *N*-point input	$(N_F + 1)MNlog2N$
IFFT over f	N_F repetition of *N* groups of *M*-point IFFT	$N_F \frac{MN}{2} logM$

Table 4.3 Computational load of processes in the existing RFT with CZT

Step	**Processing**	**Number of complex multiplications**
Obtaining Y(f,n)	*MN*-point complex multiplication and *N* groups of *M*-point FFT	$MN + \frac{MN}{2} logM$
CZT over n	M groups of N_v -point CZT of *N*-point input	$MJlogJ$
IFFT over f	*N* groups of *M*-point IFFT	$\frac{MN}{2} logM$

Table 4.4 Computational load of processes in the proposed RFT with CZT

Step	**Processing**	**Number of complex multiplications**
Obtaining Y(f,n)	*MN*-point complex multiplication and *N* groups of *M*-point FFT	$MN + \frac{MN}{2} logM$
CZT over n	N_F repetition of *M* groups of *K*-point modified CZT of *N*-point input	$M\frac{(N_F+1)}{2} T\log T$
IFFT over f	N_F repetition of *N* groups of *M*-point IFFT	$\frac{N_F MN}{2} logM$

Table 4.1 and Table 4.3 show computational load of the processes in the existing KT and RFT using CZT, while Table 4.2 and

Table 4.4 show computational load of the processes in the existing KT and RFT using CZT, respectively.

Table 4.5 depicts the total number of complex multiplications required in the proposed and the standard RFT and KT algorithms.

The ratios of the proposed methods' computational complexity to the existing methods' complexity are shown in Figure 4.4 where $M = 512, N = 4, N_v = 1024$. The reduction in the computational load of the KT is a factor of 1.5 for moderate and

high N_F. The reduction in the computational load of the RFT is more than a factor of 2 for moderate N_F. However, the proposed RFT is not favorable for extreme N_F.

Table 4.5 Computational load of the existing and the proposed methods

Algorithm	**Number of complex multiplications**
Standard KT	$MN[1+\frac{(N_F+1)}{2}\log M + N_F(1+2\log 2N)]$
Proposed KT	$MN[1+\frac{(N_F+1)}{2}\log M + (N_F+1)log2N]$
Standard RFT	$M[N+(N\log M + J\log J)]$
Proposed RFT	$M[N+\frac{(N_F+1)}{2}(N\log M + T\log T)]$

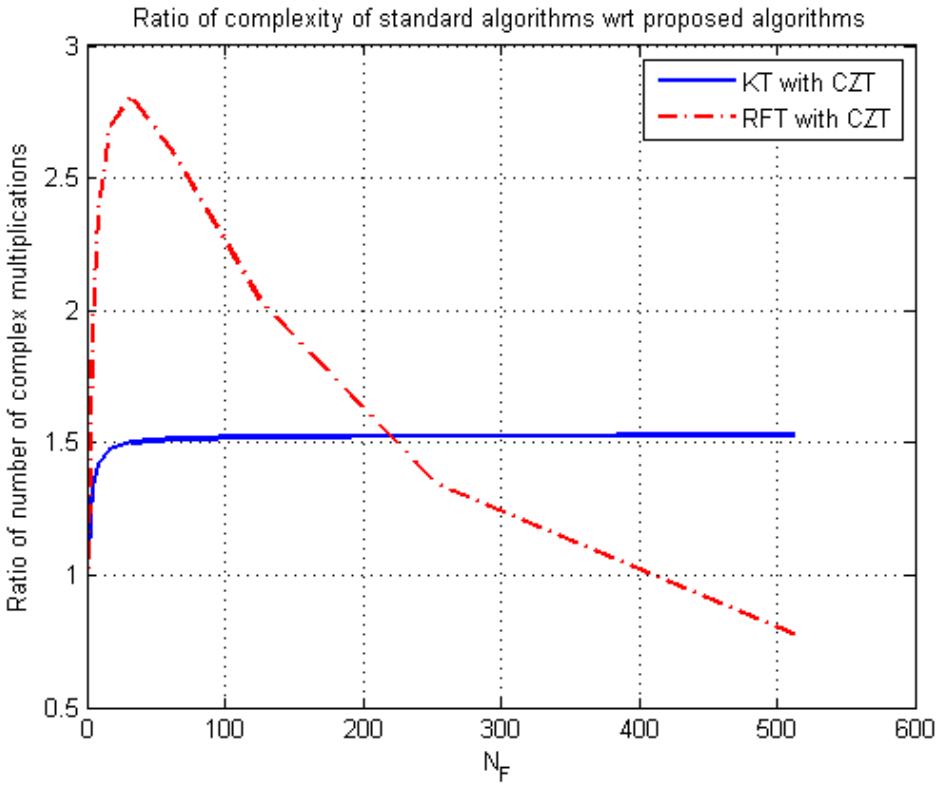

Figure 4.4. The ratios of the proposed methods' computational complexity to the existing methods' complexity over N_F

Furthermore, we have investigated the impact of N on the efficiency. The proposed KT is more favorable for higher values of N, on the contrary to the proposed RFT.

We also find that the proposed RFT is more advantageous if N_F and K values are close.

The four algorithms' computational load over N_v is shown in Figure 4.5 for $M = 512, N = 4, N_F = K$. It is clear that the proposed methods are more efficient than the existing methods.

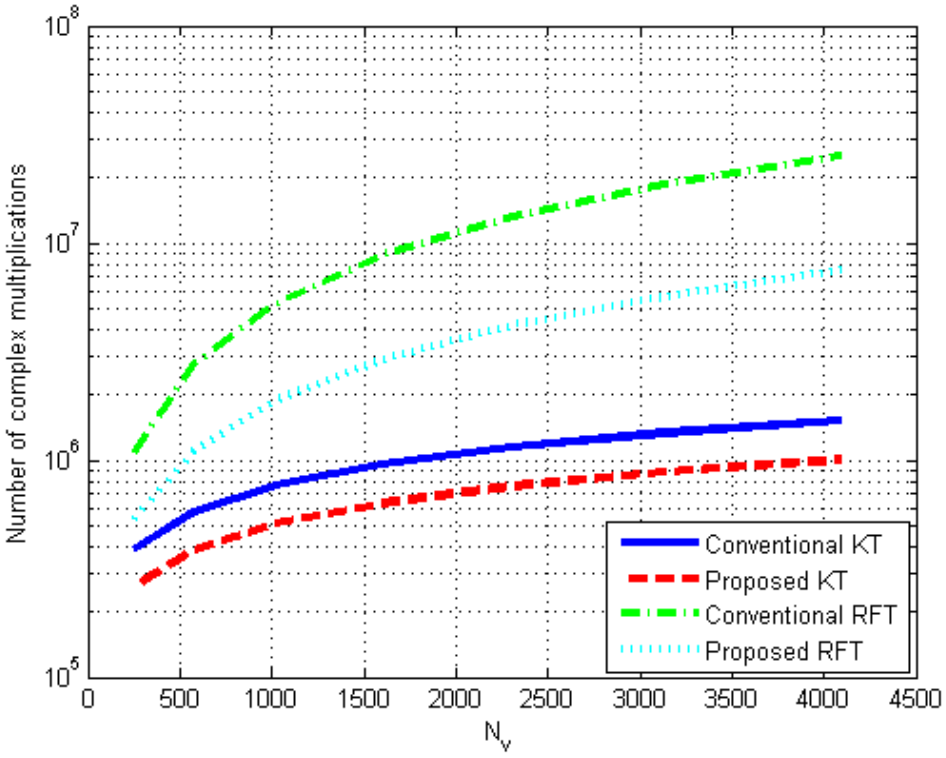

Figure 4.5. The algorithms' computational load over N_v

4.1.4 Simulations

A computer simulation has been carried out to observe the equality between the coherent integration output of the existing and the proposed methods. Radar parameters are given as carrier frequency $f_c = 3$ GHz , bandwidth $B = 10\ M$Hz, sampling frequency is 10 MHz, pulse width is 100 μs, pulse repetition interval $T_r = 0.5\ ms$.

Simulation parameters are set as: $R_0 = 60\ km, v = 500\ \frac{m}{s}, N_v = 800, N_F = 8, K = 100, M = 5000$, the single-sample SNR after matched filtering is 0dB. Amplitude of the coherent integration output of the proposed RFT is depicted in Figure 4.6. The maximum differences between normalized coherent integration output results of the existing and the proposed methods are 1.08 10^{-12} for RFT and 1.65 10^{-12} for KT.

Namely, both are equal within the numerical precision tolerances offered by the computers used.

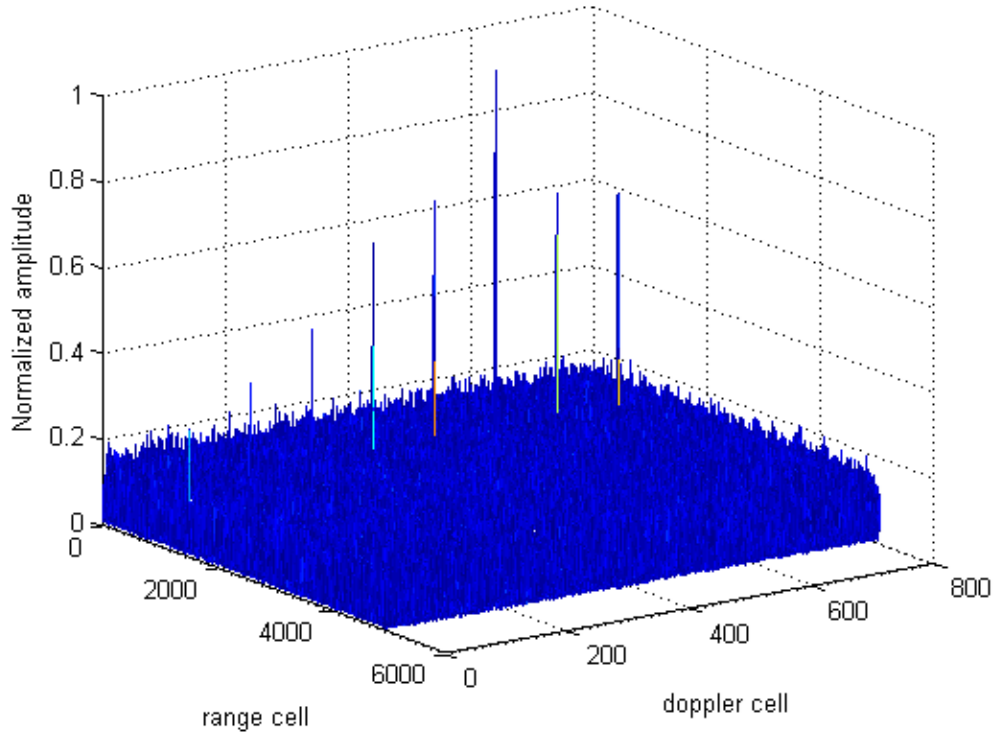

Figure 4.6. Amplitude of the coherent integration output of the proposed RFT

4.1.5 Summary

We proposed a lower complexity method to execute repeated CZT operations with differing initial points and constant angular distance on the spiral contour. We have depicted that the KT can be implemented with o loss in performance using the proposed method. In addition, a new method to implement the RFT using repeated CZT has been developed. Then, we have developed a new RFT implementation with lower computational complexity and the same performance compared to the existing RFT. Consequently, we have provided a computer simulation, which demonstrates the equality of integration performances of both the existing and the proposed RFT.

Both KT and RFT implementations proposed in this work are more favorable when there is Doppler ambiguity. The proposed KT implementation is more advantageous for higher number of pulses to be integrated and higher number of possible ambiguity factors. The proposed RFT implementation is computationally efficient when a low number of pulses are integrated which is commonly encountered for low PRF mode due to limited integration time and the searching ambiguity factor number N_F is not too high.

4.2 Low Complexity Range Alignment Technique Based on Doppler Ambiguity Shift Transform [52]

In this section, a low complexity method to compensate range migration is proposed. The proposed method searches for the Doppler ambiguity factor and the residual velocity jointly. Besides, a novel method, called Doppler ambiguity shift transform (DAST) is introduced to search for Doppler ambiguity factor. We show with analysis and simulations that the proposed method achieves almost same detection performance as the standard RFT method.

4.2.1 Proposed algorithm

We can write the matched filter output as given in (4.14).

$$Y(f,n) = |P(f)|^2 exp[-j\frac{4\pi}{c}(f+f_c)(R_0 + vnT_r)] + P^*(f)U(f,n) \quad (4.14)$$

Instead of searching for the velocity by using CZT in the existing RFT, we can correct Doppler ambiguity and search for the residual velocity.

We express radial velocity in terms of the blind and the residual velocity:

$$v = F_{amb}v_{blind} + v_{res} \quad (4.15)$$

where the Doppler ambiguity factor is represented by $F_{amb} = round(v/v_{blind})$, the blind speed is given as $v_{blind} = \frac{c}{2f_cT_r}$, and v_{res} is the residual velocity with $|v_{res}| < \frac{v_{blind}}{2}$.

Inserting (4.15) into (4.14), we get the following expression:

$$Y(f,n) = |P(f)|^2 exp[-j\frac{4\pi}{c}(f+f_c)(R_0 + v_{res}nT_r)] \times exp[-j2\pi F_{amb}\frac{f}{f_c}n] + P^*(f)U(f,n) \quad (4.16)$$

We suggest to use CZT in order to search for the Doppler ambiguity factor and the residual velocity different from the existing RFT. CZT of $Y(f,n)$ is computed as follows

$$Z(f,k) = \underset{n}{CZT}[Y(f,n)] = \sum_n Y(f,n)A^{-n}W^{nk} \quad k = 0,1,\ldots,K-1 \quad (4.17)$$

where we $K = \frac{v_{blind}}{\Delta v}$ is defined as the number of the residual velocities to be searched.

Inserting $Y(f,n)$, A , and Winto (4.17), we have the following expression

$$Z(f,k) = \sum_n Y_c(f,n)exp[-j2\pi F_{amb}\frac{f}{f_c}] \times \exp[j2\pi nk(f+f_c)\frac{2\Delta v}{c}T_r] + H(f,k) \quad (4.18)$$

where $Y_c(f,n)$ can be expressed as given in (4.19).

$$Y_c(f,n) = |P(f)|^2 \exp[-j4\pi(f+f_c)(R_0 + v_{res} n T_r)/c] \tag{4.19}$$

We can rewrite (4.18):

$$Z(f,k) = \sum_n Y_c(f,n) exp[-j2\pi(k_{amb} - k)\frac{(f+f_c)}{f_c}\frac{n}{K}] + H(f,k) \tag{4.20}$$

where

$k_{amb} = F_{amb} K \frac{f}{(f+f_c)}$, and $H(f,k) = \underset{n}{CZT}[P^*(f)U(f,n)]$.

the Doppler-ambiguity-compensated CZT output can be obtained after substituting $k + k_{amb}$ for k in the signal component of (4.20).

$$Z_c(f,k) = \sum_n Y_c(f,n) exp[j2\pi \frac{(f+f_c)}{f_c}\frac{nk}{K}] \tag{4.21}$$

That is to say, the Doppler ambiguity can be compensated if we shift $Z(f,k)$in Doppler frequency for each f, but one should consider the change in phase and amplitude of $Z(f,k)$ while shifting $Z(f,k)$

in k. Substituting $Y_c(f,n)$ in (4.20), we get

$$Z(f,k) = |P(f)|^2 exp[-j2\pi(f+f_c)\frac{2R_0}{c}] \sum_n exp[-j2\pi x n] + H(f,k) \tag{4.22}$$

where $x = (f+f_c)\frac{2v_{res}}{c} T_r + F_{amb}\frac{f}{f_c} + \frac{(f+f_c)}{f_c}\frac{k}{K}$.

The expression (4.22) can be rearranged as

$$Z(f,k) = |P(f)|^2 \exp\left[-j2\pi(f+f_c)\frac{2R_0}{c}\right]\frac{\sin(\pi Nx)}{\sin(\pi x)}\exp[j\pi x(N-1)]] + H(f,k) \tag{4.23}$$

Obviously, phase and amplitude variations exist due to the shifting of $Z(f,k)$ k_{amb} samples. Therefore, we introduce a novel technique, DAST (Doppler ambiguity shift transform), for the Doppler ambiguity compensation. DAST can be applied by shifting $\hat{k}_{amb} = round(k_{amb})$ samples for each f in $Z(f,k)$ and correcting the phase and amplitude variation coming from shifting:

$$DAST[Z(f,k), F_{amb}]$$
$$= Z(f, k+\hat{k}_{amb}) \times exp[j\pi(N-1)\frac{(f+f_c)}{f_c}\frac{\hat{k}_{amb}}{K}]|\frac{sin(\pi y)}{sin(\pi N y)}| \tag{4.24}$$

where $y = F_{amb}\frac{f}{f_c} - \frac{f+f_c}{f_c}\frac{k_{amb}}{K}$.

The Doppler ambiguity factor can be searched by applying coherent integration for each F_{amb} value, and choosing F_{amb} value giving the maximum peak amplitude. One can perform coherent integration by taking IDTFT on (4.24):

$$z_c(\tilde{t}, k, F_{amb}) = \underset{f}{IDTFT}[DAST[Z(f,k), F_{amb}]]\hat{F}_{amb}$$
$$= \underset{F_{amb}}{argmax}[|z_c(\tilde{t}, k, F_{amb})|] \tag{4.25}$$

Figure 4.7 shows the block diagram of the proposed method.

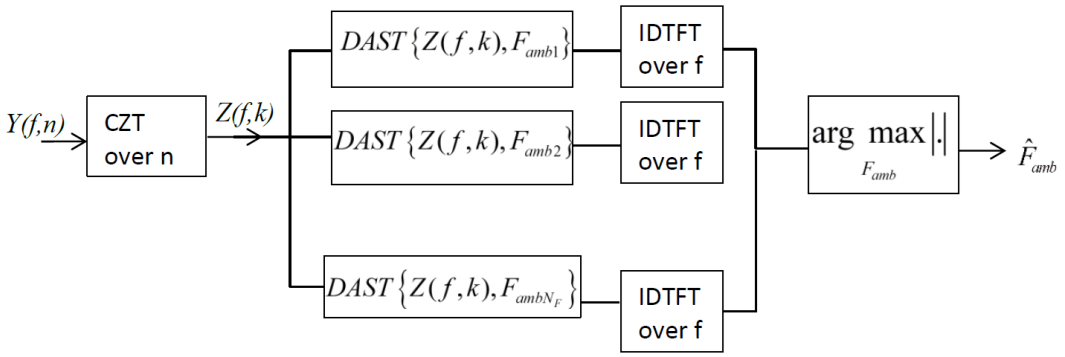

Figure 4.7. Block diagram of the proposed algorithm employing DAST

Section 4.1 [51] , we developed a low complexity method to repeat execution of CZT for searching the Doppler ambiguity number and the residual velocity. Although in this way we can reduce the computational complexity compared to the RFT [21] realized with CZT, there would be a significant improvement in complexity reduction if we could get rid of repeating CZT. For this reason, we propose a new method to perform single CZT instead of repeating CZT many times in searching for the Doppler ambiguity number and the residual velocity.

4.2.2 Computational Load Analysis

Table 4.6 depicts the number of complex multiplications required in the existing RFT [19] examined in 2.3.4, the RFT realized with CZT [21] examined in 2.3.5, and the proposed method. where N is the number of pulses to be integrated, M is the number of range bins in PRI, N_F is the total number of ambiguity factors, N_v is the number of searched velocities, and K is the number of search residual velocities. We assume that K is an integer satisfying $N_v = KN_F$. To simplify the investigation, we set $J = N_v + N$, and $T = K + N$.

Table 4.6 Number of complex multiplications for algorithms

Algorithm	**Number of complex multiplications**
Conventional RFT [19] (see in 2.3.4)	$M[N + NlogM + NN_V + N_V/2]$
CZT-based RFT [21] (see in 2.3.5)	$M[N + NlogM + JlogJ]$
Proposed method	$M[N + \frac{N}{2}logM + TlogT + N_FK + \frac{NN_F}{2}logM]$

Figure 4.8 shows the ratio of the proposed method's computational complexity to the existing method's [21] complexity depending on the velocity search resolution Δv. We assume $f_c = 0.5$ GHz, $f_s = B = 20$ MHz, pulse repetition interval $T_r = 240\mu s$, $N = 32$, $v_{max} = 15000$ m/s, which corresponds to M $= 4800, N_F = 25$.

In addition, the impact of N on the efficiency is examined. Figure 4.9 shows the ratio of the proposed method's computational complexity to the existing method's [21] complexity depending on number of pulses in CPI. We assume $N_v = 5120, N_F = 20, M = 4800$. We note that the proposed algorithm has a much lower computational complexity compared to the existing method [21] , particularly at a lower velocity search resolution and a lower number of impulses in CPI, which is the usual case when high velocity resolution is needed at low and medium PRF is radars.

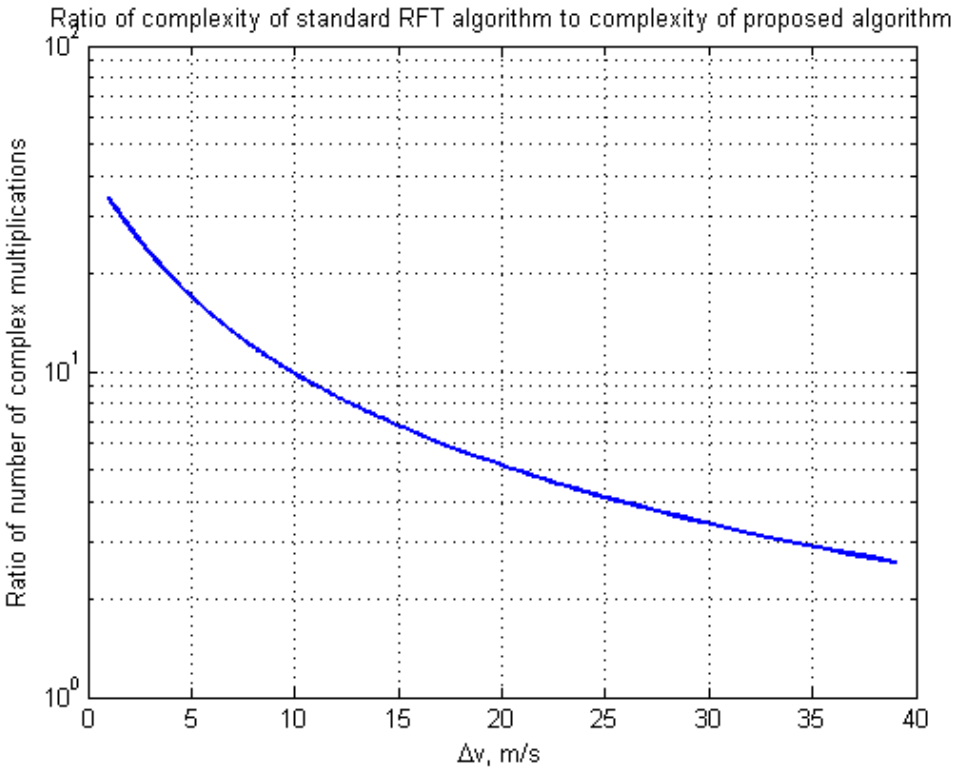

Figure 4.8. Ratio of the proposed method's computational complexity to the existing method's [21] complexity depending on the velocity search resolution Δv

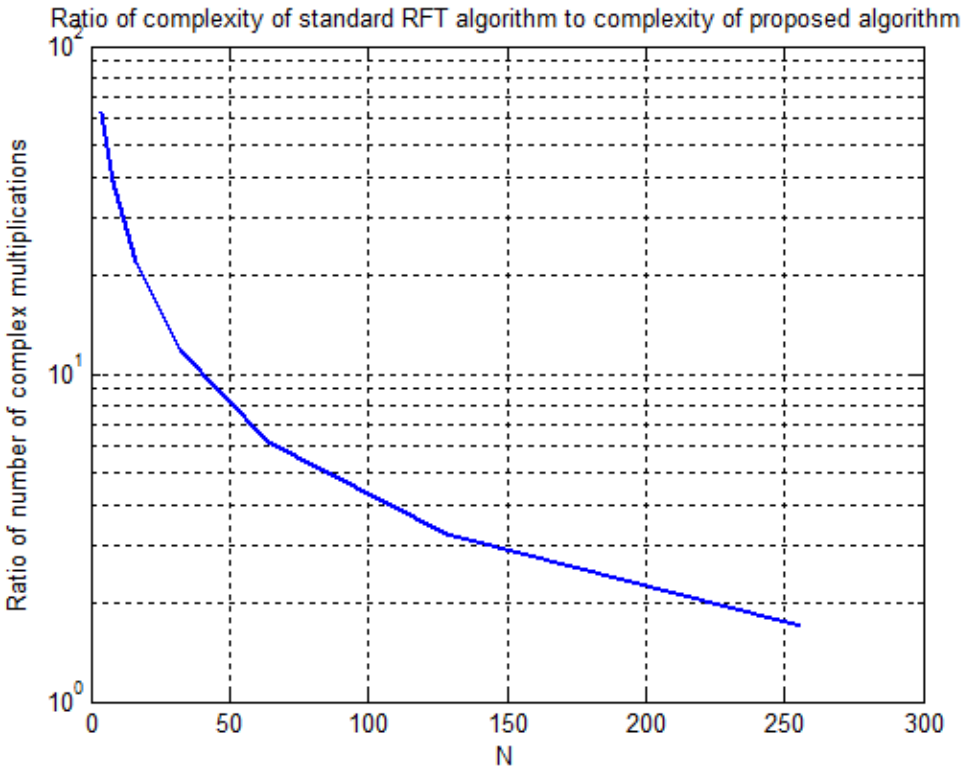

Figure 4.9 Ratio of the proposed method's computational complexity to the existing method's [21] complexity over N when N_F=K

4.2.3 Simulation Results

A computer simulation has been carried out for the performance comparison of the existing [21] and the proposed algorithm. We assume a simple point target model, LFM envelope , non-fluctuating Swerling-0 signal model, and complex additive Gaussian white noise background. Radar parameters are given as carrier frequency $f_c = 0.5$ GHz , bandwidth $B = 20$ MHz, sampling frequency is 40 MHz, pulse width is 60 μs, pulse repetition interval $T_r = 240$ μs. Simulation parameters are set as: v = 7000 m/s, N = 16, K = 64, N_v = 1536. Figure 4.10 and Figure 4.11 demonstrate that the DAST compensates the range migration.

Figure 4.12 shows probability of detection vs. single-sample SNR for the CZT based RFT [21] and the proposed method where false alarm probability is$P_F = 10^{-4}$.

Simulation result depicts that approximately same detection performance can be achieved by the proposed method.

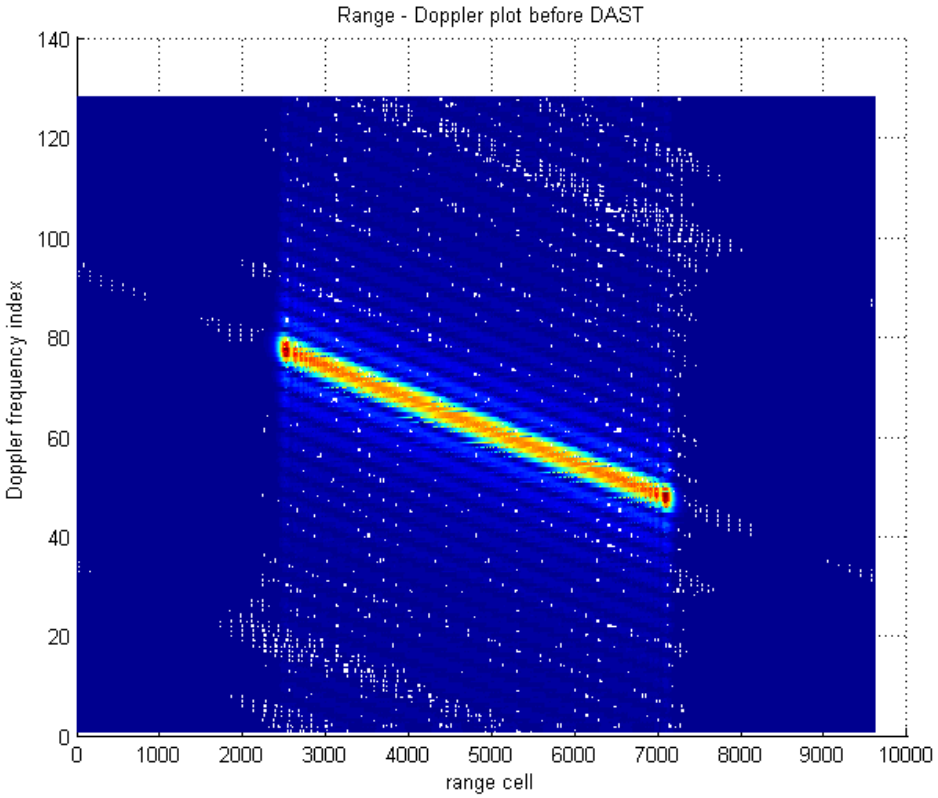

Figure 4.10. Range - Doppler plot of $|Z|$, i.e., before DAST

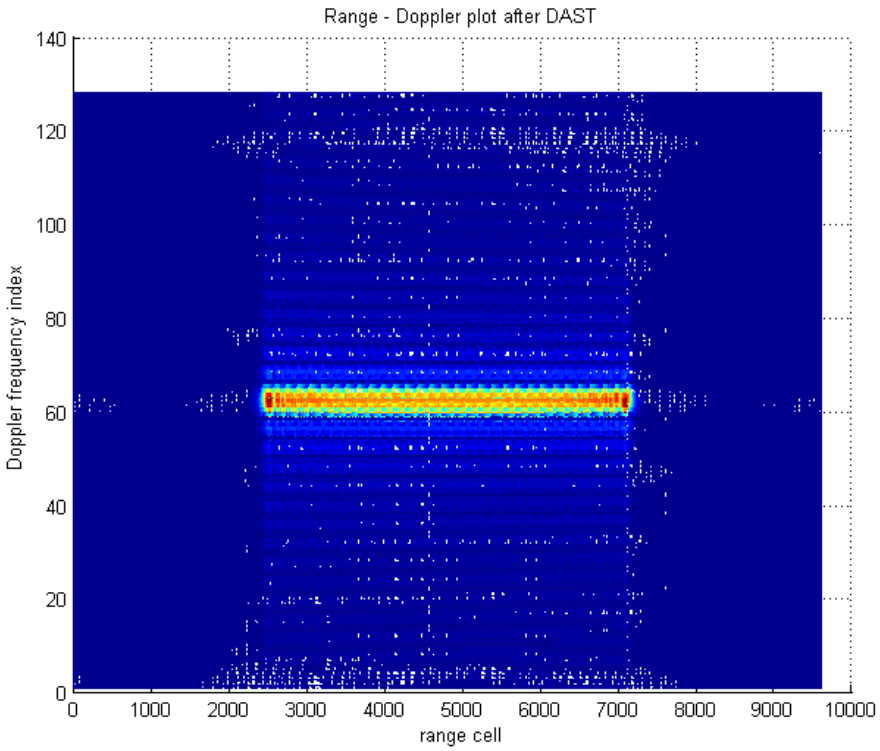

Figure 4.11. Range- Doppler plot of |DAST[Z]|, i.e., after DAST

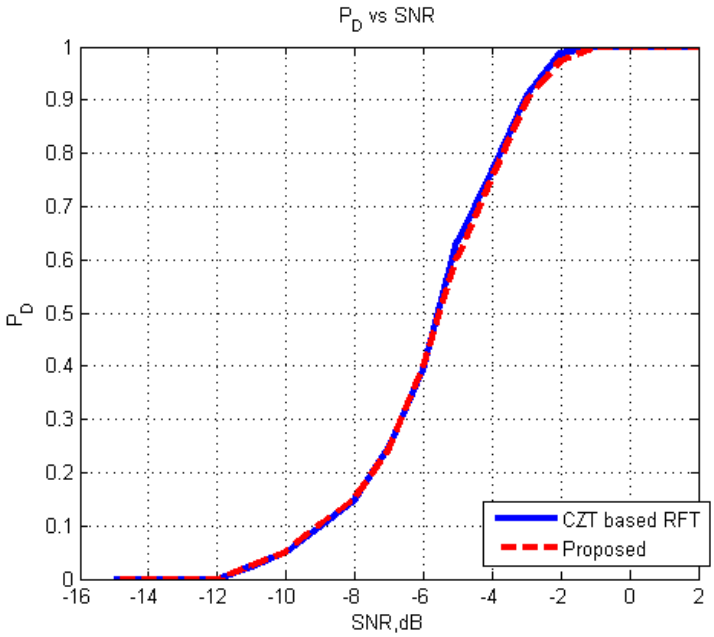

Figure 4.12. P_D vs SNR after matched filtering with false alarm probability $P_F = 10^{-4}$

4.2.4 Summary

We proposed a low complexity algorithm to compensate the range migration. Instead of searching for the radial velocity, we search jointly the residual velocity and the Doppler ambiguity factor. CZT is employed to search for the residual velocity. We have introduced a new computationally inexpensive method, DAST, searches and corrects the Doopler ambiguity. It turns out that the proposed method can be used to achieve approximately the same detection performance as with the RFT. The computational efficiency has been improved by more than ten times comparing with our previously proposed algorithm [51].

CHAPTER 5

CONCLUSIONS

In this thesis, we have considered the range migration problem that can arise especially in conjunction with wide bandwidth, long integration time, and high speed target in radar systems.

We have approached the range migration issue from two different perspectives: exploring new RMC methods to strike a balance between the computational efficiency and the detection performance, and investigating the RMC methods in realistic radar environment including clutter and target fluctuation.

Realistic synthetic sea clutter data has been generated and it is shown that detection performance can be improved if KT is applied after suppressing this clutter for detection of range-migrating target. It has been depicted that suppressing the clutter before applying KT improves performance compared to applying KT before suppressing the clutter. The main reason is that Doppler spectrum gets larger after applying the KT and the clutter cannot be suppressed perfectly since the clutter suppression filter is applied according to clutter covariance matrix before applying the KT.

A new method has been proposed to eliminate the range migration problem jointly for range migrating clutter and the range migrating target. By the proposed method, we can align range profiles of both clutter and target without bringing additional computational cost with respect to only range alignment of target.

A hybrid integration scheme has been presented to detect moderately fluctuating targets. It is shown that it is possible by the combination of hybrid integration and frequency diversity to achieve the best detection probability for a given combination of SNR, correlation coefficient and total number of pulses. When the KT is applied

to remove range migration for moderately fluctuating targets, the detection performance is degraded about 0.8 dB SNR due to interpolation loss during KT.

We have proposed [51] an efficient implementation of repetitive CZT to reduce computational complexity of the KT because the KT requires repeated execution of CZT for each potential Doppler ambiguity factor. We found a new implementation of RFT that uses repetitive CZT operation. In this way, we managed to reduce the complexity of the RFT as well by employing our new efficient repetitive CZT method. The proposed method turns out to be mathematically equivalent to the standard method, so there is no loss of performance.

We have introduced [52] another efficient method to search for the Doppler ambiguity and the residual velocity without repeating CZT, which is more than ten times more efficient compared to [51]. The proposed method is more favorable especially in low and medium PRF radars with high velocity resolution.

In this thesis, we have investigated the range migration compensation under the target fluctuation and the clutter separately. Future research may consider another realistic case when the target fluctuation and the clutter exist at the same time. Performance of the combination of hybrid integration scheme with frequency diversity can be evaluated for this case. New methods can be explored to handle the target fluctuation and clutter together. It would be interesting how to combine frequency diversity and hybrid integration to improve detection performance for a given clutter statistics and fluctuation correlation coefficient. In addition, one could take the complex nature of sea clutter fluctuations into account to provide a better performance.

REFERENCES

[1] D. K. Barton, Radar System Analysis and Modeling, Norwood: Artech House, 2005.

[2] M. I. Skolnik, Introduction to Radar system, McGraw-Hill Companies, 2002.

[3] J. Carretero-Moya, J. Gismero-Menoyo , A. Asensio-López and A. Blanco-del-Campo , "Application of the Radon transform to detect small-targets in sea clutter," *IET Radar, Sonar & Navigation,* vol. 3, no. 2, pp. 155-166, 2009.

[4] M. Xing, J. W. G. Su und Z. Bao, «New parameter estimation and detection algorithm for high speed small target,» *IEEE Transactions on Aerospace and Electronic Systems,* Bd. 47, Nr. 1, pp. 214-224, 2011.

[5] M. R. Sharif und S. S. Abeysekera, «Efficient wideband signal parameter estimation using a radon-ambiguity transform slice,» *IEEE transactions on aerospace and electronic systems,* Bd. 43, Nr. 2, pp. 673-688, 2007.

[6] B. D. Carlson, E. D. Evans and S. L. Wilson, "Search radar detection and track with the Hough transform. I. system concept," *IEEE Transactions on Aerospace and Electronic Systems* , vol. 30, no. 1, pp. 102-108, 1994.

[7] B. D. Carlson, E. D. Evans and S. L. Wilson, "Search radar detection and track with the Hough transform. II. detection statistics," *IEEE Transactions on Aerospace and Electronic Systems,* vol. 30, no. 1, pp. 109-115, 1994.

[8] B. Carlson, E. Evans and S. Wilson, "Search radar detection and track with the Hough transform. III. Detection performance with binary integration," *IEEE Transactions on Aerospace and Electronic Systems* , vol. 30, no. 1, pp. 116-125, 1994.

[9] D. Orlando, L. Venturino, M. Lops und G. Ricci, «Track-before-detect strategies for STAP radars,» *IEEE Transactions on Signal Processing* , Bd. 58, Nr. 2, pp. 933-938, 2009.

[10] F. Ehlers, D. Orlando und G. Ricci., «Batch tracking algorithm for multistatic sonars,» *IET Radar, Sonar & Navigation,* Bd. 6, Nr. 8, pp. 746-752, 2012.

[11] X. Li, G. Cui, W. Yi und L. Kong, «Sequence-reversing transform-based coherent integration for high-speed target detection,» *IEEE Trans. Aerosp. Electron. Syst.,* Bd. 53, Nr. 3, 2017.

[12] X. Li, G. Cui, W.Yi, L.Kong, J.Yang und Y. Huang, «A fast non-searching method for maneuvering target detection based on ACCF,» in *Proc. IEEE Radar Conf. (RadarCon)*, 2015.

[13] J. Zheng, T. Su, W. Zhu, X. He und Q. H. Liu, «Radar high-speed target detection based on the scaled inverse Fourier transform,» *IEEE Journal of Selected Topics in Applied Earth Observations and Remote Sensing,* Bd. 8, Nr. 3, pp. 1108-1119, 2014.

[14] R. P. Perry, R. Dipietro and R. L. Fante, "SAR Imaging of Moving Targets," *IEEE Transactions on Aerospace and Electronic Systems,* vol. 35, no. 1, 1999.

[15] D. Zhu, Y. Li und Z. Zhu, «A keystone transform without interpolation for SAR ground moving-target imaging,» *IEEE Geoscience and Remote Sensing Letters,* Bd. 4, Nr. 1, pp. 18-22, 2007.

[16] Y. Li, T. Zeng and T. Long, "Range Migration Compensation and Doppler Ambiguity Resolution by Keystone Transform," in *2006 CIE International Conference on Radar,* 2006.

[17] S. Zhang, T. Zeng, T. Long and H. Yuan, "Dim target detection based on keystone transform," in *IEEE International Radar Conference*, 2005.

[18] X. Li, G. Cui, W. Yi, L. Kong und J. Yang, «Range migration correction for maneuvering target based on generalized keystone transform,» in *IEEE Radar Conf. (RadarCon)*, 2015.

[19] J. Xu, J. Yu, Y.-N. Peng and X.-G. Xia, "Radon-fourier transform for radar target detection, i: Generalized doppler filter bank," *IEEE Transactions on Aerospace and Electronic Systems*, vol. 47, no. 2, p. 1186–1202, 2011.

[20] J. Xu, J. Yu, Y. -N. Peng and X. -G. Xia, "Radon-Fourier Transform for Radar Target Detection (II): Blind Speed Sidelobe Suppression," *IEEE Transactions on Aerospace and Electronic Systems*, vol. 47, no. 4, pp. 2473-2489, 2011.

[21] J. Yu, J. Xu, Y.-N. Peng and X.-G. Xia, "Radon-Fourier transform for radar target detection (III): Optimality and fast implementations," *IEEE Trans. Aerosp. Electron. Syst*, vol. 48, no. 2, pp. 991-1004, 2012.

[22] Y. Zhao, J. Wang, L. Huang and R. Yang, "Low complexity keystone transform without interpolation for dim moving target detection," in *Proceedings of 2011 IEEE CIE International Conference on Radar*, 2011.

[23] C. E. Cook and M. Bernfeld, Radar Signals An Introduction to Theory and Application, New York: Academic Press Inc., 1967.

[24] R. J. Marks, Introduction to Shannon Sampling and Interpolation Theory, New York: Springer, 1991.

[25] J. Diaz-Carmona and G. J. Dolecek, "Fractional Delay Filters," in *Applications of MATLAB in Science and Engineering*, IntechOpen, 2011, 2011.

[26] A. V. Oppenheim, R. W. Schafer and J. R. Buck, Discrete-Time Signal Processing, New Jersey: Prentice Hall, 1999.

[27] O. Arıkan, *Investigation of topics in radar signal processing*, Urbana, IL: University of Illinois, 1990.

[28] L. Rabiner, R. W. Schafer and C. Rader, "The chirp z-transform algorithm," *IEEE transactions on audio and electroacoustics*, vol. 17, no. 2, pp. 86-92, 1969.

[29] N. Temme, "The Radon Transform: First Steps," in *CWI Newsletter*, Amsterdam, Centre for Mathematics and Computer Science, 1987, pp. 41-46.

[30] J. Radon, "Über die Bestimmung von Funktionen durch ihre Integralwerte längs gewisser Mannigfaltigkeiten," in *Berichte Sächsische Akademie der Wissenschaften*, Leipzig, 1917.

[31] M. Wang, A. K. Chan and C. K. Chui, "Linear frequency modulated signal detection using wavelet packet, ambiguity function and Radon transform," in *IEEE Antennas and Propagation Society International Symposium*, California, 1995.

[32] M. T. Rey, J. K. Tunaley, J. T. Folinsbee, P. A. Jahans, J. A. Dixon and M. R. Vant, "Application Of Radon Transform Techniques To Wake," *IEEE Transactions on Geoscience and Remote Sensing*, vol. 28, no. 4, pp. 553-560, 1990.

[33] R. K. Satzoda, S. Suchitra and T. Srikanthan, "Parallelizing the Hough Transform Computation," *IEEE Signal Processing Letters* , vol. 15, pp. 297 - 300, 2008.

[34] J. Illingworth and J. Kittler, "A survey of the hough transform," *Computer Vision, Graphics, and Image Processing*, vol. 44, no. 1, pp. 87-116, 1988.

[35] M. van Ginkel, L. van Vliet and C. L. L. Hendriks, "A short introduction to the Radon and Hough transforms and how they relate to each other," Delft University of Technology, 2004.

[36] V. M. Orlenko and Y. D. Shirman, "Non-coherent integration losses of wideband target detection," in *Proceedings of the European Radar Conference*, 2004.

[37] K. D. Ward, S. Watts and R. J. Tough, Sea Clutter: Scattering, the K Distribution and Radar Performance, London: IET, 2006.

[38] S.Watts, "Cell-averaging CFAR gain in spatially correlated K-distributed clutter," in *IEE Proceedings-Radar, Sonar and Navigation*, 1996.

[39] R. J. A. Tough and K. D. Ward, "The correlation properties of gamma and other non-Gaussian processes generated by memoryless nonlinear transformation," *Journal of Physics D: Applied Physics,* vol. 32, no. 23, pp. 3075-3084, 1999.

[40] M. Greco and S.Watts, "Radar Clutter Modeling and Analysis," in *Academic Press Library in Signal Processing: Volume 2 Communications and Radar Signal Processing*, Academic Press, 2014.

[41] F. E. Nathanson, J. P. Reilly and M. N. Cohen, Radar Design Principles, SciTech Publishing, Inc., 1999.

[42] M. A. Richards, Fundamentals of Radar Signal Processing, McGraw-Hill, 2005.

[43] M. Rangaswamy, D. Weiner and A. Ozturk, "Computer generation of correlated non-Gaussian radar clutter," *IEEE Transactions on Aerospace and Electronic Systems* , vol. 31, no. 1, pp. 106 - 116, 1995.

[44] M. A. Richards, J. Scheer and W. Holm, Principles of Modern Radar Vol. I: Basic Principles, SciTech Publishing, 2010.

[45] J. DiFranco and W. Rubin, Radar Detection, Scitech Radar and, 2004.

[46] M. Richards, «Threshold Detection of Radar Signals,» in *Fundamentals of Radar Signal Processing*, Mc Graw Hill, 2005, pp. 321-336.

[47] R. Scholtz, J. Kappl and N. E. Nahi, "The Detection of Moderately-Fluctuating Rayleigh Targets," *IEEE Transactions on Aerospace and Electronic Systems,* vol. 12, no. 2, 1976.

[48] "Small boat detection research at the CSIR," [Online]. Available: http://www.csir.co.za/small_boat_detection/. [Accessed 15 12 2014].

[49] J. G. Proakis, Digital Communications, McGraw-Hill Education, 2007.

[50] E. Conte, A. D. Maio und G. Ricci, «Covariance matrix estimation for adaptive CFAR detection in compound-Gaussian clutter,» *IEEE Transactions on Aerospace and Electronic Systems,* Bd. 38, Nr. 2, pp. 415-426, 2002.

[51] O. Çulha and Y. Tanık, "Low complexity keystone transform and radon fourier transform utilizing chirp-z transform," *IEEE ACCESS,* vol. 8, p. 105535–105541, 2020.

[52] O. Çulha and Y. Tanık, "Efficient Range Migration Compensation Method Based on Doppler Ambiguity Shift Transform," *IEEE Sensors Letters,* vol. 6, no. 3, pp. pp. 1-4, 2022.

[53] O. Çulha und Y. Tanık, «Range migration compensation based on keystone transform in sea clutter,» in *24th Signal Processing and Communication Application Conference (SIU),* 2016.

[54] O. Çulha und Y. Tanik, «The detection of fluctuating targets in case of range migration,» in *25th Signal Processing and Communications Applications Conference (SIU)*, 2017.